University of Alberta

The role of water in the transformation of opal-A to opal-CT in siliceous sinter

by

Rachel Singer

A thesis submitted to the Faculty of Graduate Studies and Research in partial fulfillment of the requirements for the degree of Master of Science

Department of Earth and Atmospheric Science

Edmonton, Alberta

Fall 2006

Your file Votre référence
ISBN: 978-0-494-22371-0
Our file Notre référence
ISBN: 978-0-494-22371-0

Abstract

Emerging hot spring waters commonly precipitate opal-A ($SiO_2 \cdot nH_2O$), resulting in the formation of different types of siliceous sinter with variable microstructures and water contents. The patchy and inhomogeneous transformation of opal-A to its more stable phase, opal-CT, takes place through a dissolution-reprecipitation pathway. Fabrics indicative of dissolution and reprecipitation are most common in sinter composed of opal-CT. The total water content, determined using electron microprobe (EMP) analysis and Fourier transform infrared (FTIR) spectroscopy, of opal-A deposits (6-9 wt %) are generally higher than opal-CT (3-6 wt %). The total water content (molecular water + silanols) in opal-A and opal-CT is largely formed of molecular water. In the transformation of opal-A to opal-CT, silanols are lost before the molecular water. These trends are common in sinters from the Taupo Volcanic Zone, New Zealand and Geysir, Iceland, indicating the transformation of opal-A to opal-CT must follow analogous pathways despite variable environments.

Acknowledgements

I would like to thank Dr. Brian Jones for his support and guidance. His thorough editing skills have definitely paid off. Thomas Stachel, for allowing me free reign of his FTIR. Diane Caird, for running my XRD samples; non-crystalline and not very exciting. George Braybrook, for his wonderful SEM shots and many enjoyable hours spent on the SEM. Sergei Matveev, for his great help with the EMP. Bob Luth, for his help with the EMP calculations. Mark Labbe and Don Resultay, for their speedy work in thin section preparation.

I would also like to thank my family and friends for their support in this process, especially Peter. It has been quite the journey and a valuable learning experience.

Table of Contents

List of Tables

List of Figures

List of Abbreviations

Ā – Integral absorbance

BSEI – Backscattered electron image

C - Concentration

d – Sample thickness

DI – Dull indurated sinter

EDX – Energy dispersive X-ray

EMP – Electron microprobe

FTIR – Micro-Fourier transform infrared spectroscopy

FWHM – Full width half maximum

H_2O_{mol} – Molecular water

H_2O_{SiOH} – Silanol water

ICE – Iceland

N – Number of analyses

NZ – New Zealand

PF – porous friable sinter

PI – Porous indurated sinter

PV – Patchy vitreous sinter

SEM – Scanning electron microscopy

sp – Spicule

vit – Vitreous sinter

wt % - Weight percent

XRD – X-ray diffraction

Chapter One – Introduction

1.1 General Introduction

Hot springs and geysers are known for their impressive display of nature's beauty and wonder. World renowned spring sites include Yellowstone National Park, U.S.A., Geysir, Iceland, and the Taupo Volcanic Zone located on the North Island of New Zealand. Mineral deposits surrounding spring environments have long been studied by the scientific community (e.g., Weed 1889; White et al. 1956). A variety of mineral deposits including calcite, aragonite, barite, and siliceous sinter may be produced at spring sites depending on the chemical composition of the emerging hydrothermal waters. Such mineral deposits continue to be of great interest, as they have been implicated in the preservation of early microbial life on Earth (e.g., Cady and Farmer 1996; Konhauser et al. 2003), the identification of hydrothermal systems on Mars (e.g., Michalski et al. 2003; Goryniuk et al. 2004), and as indicators of paleoenvironmental conditions (e.g., Jones et al. 1997; Lowe and Braunstein 2003; Mountain et al. 2003).

Neutral to slightly alkaline silica-rich hydrothermal waters surfacing from presently active hot springs and geysers commonly produce siliceous sinter that is composed of a non-crystalline silica precipitate, opal-A (Fournier 1985). Opal-A is a metastable mineral; time and/or high temperatures and pressures favour its progressive development towards quartz, a thermodynamically stable state. Opal-A is commonly transformed via a pathway from opal-A through opal-CT and/or opal-C to quartz (Jones and Segnit 1972; Fournier 1985; Williams et al. 1985; Landmesser 1998). This mineral transformation in sinter diagenesis is generally marked by increases in structural ordering and density, and by decreases in porosity and water content (Herdianita et al. 2000b). Similar trends of

evolving crystallinity have been recorded in deep sea siliceous sediments (Murata and Nakata 1974; Isaacs 1982; Fröhlich 1989; Knauth 1994; Rice et al. 1995). Although recent studies have improved our understanding of the transformation from opal-A to opal-CT, many aspects of this transition remain a mystery (Campbell et al. 2001; Lynne and Campbell 2003, 2004; Rodgers et al. 2004; Lynne et al. 2005).

Opal-A and opal-CT are hydrated siliceous minerals ($SiO_2 \cdot nH_2O$) that contain varying amounts of silanols (OH groups attached to silicon), water trapped in micropores, and/or water adsorbed onto exposed surfaces (Jones and Segnit 1969; Langer and Flörke 1974; Graetsch 1994). The total water content (silanol groups + molecular water) in opal-A and opal-CT can range from 1.5 to 15.3 wt %, although opal-A tends to have higher water contents than opal-CT (Segnit et al. 1965; Langer and Flörke 1974; Aines and Rossman 1984; Adams et al. 1991; Flörke et al. 1991; Smith 1998; Herdianita et al. 2000b; Jones and Renaut, 2004). The total water content in opal has historically been evaluated using bulk sample analysis including loss on ignition (e.g., Nicholson and Parker 1990), infrared spectroscopy (e.g., Segnit et al. 1965; Jones and Segnit 1969; Aines and Rossman 1984), differential thermal analysis and thermogravimetric analysis (e.g., Graetsch et al. 1985; Adams et al. 1991) and coulometric Karl-Fisher titration (e.g., Graetsch et al. 1985). Recent analytical work using backscattered electron images (BSEI) and electron microprobe (EMP) analysis has shown microscale variations in the total water content of sinters composed of opal-A (Jones and Renaut 2004).

Measuring the total water and identifying the different forms of water in siliceous sinter remains difficult and seriously impedes a better understanding of the opal-A to opal-CT transition. Micro-Fourier transform infrared spectroscopy (FTIR) allows for

rapid quantitative analysis of the relative contributions of silanol groups and molecular water to the total water content of opal on a microscale. Water loss during diagenetic alteration is a critical aspect in furthering our knowledge in the transition from opal-A to opal-CT.

Sinter diagenesis has been recognized as being a patchy, inhomogeneous process with respect to spatial and temporal scales (Campbell et al. 2001; Lynne and Campbell 2003, 2004; Lynne et al. 2005; Jones and Renaut in press). In order to properly evaluate the opal-A to opal-CT transformation, a detailed integrated microscale approach using various analytical techniques to evaluate both the textural and compositional changes accompanying diagenesis is necessary.

1.2 Objectives

The overall goal of this study is to enhance our understanding of the transformation of opal-A to opal-CT in siliceous sinter by providing a detailed examination of the physical macroscopic appearance of sinter, microstructures, and water content of sinters from Taupo Volcanic Zone in New Zealand and Geysir, Iceland. This is accomplished by:

- hand sample and thin section analyses,
- characterizing mineralogy using X-ray diffraction (XRD),
- characterizing microstructures using scanning electron microscopy (SEM),
- determining total water content of siliceous sinter using backscattered electron images (BSEI) and electron microprobe (EMP) analysis,

- determining the distribution of different forms of water (silanols and molecular water) in siliceous sinter using micro-Fourier transform infrared spectroscopy (FTIR), and
- comparing analytical techniques (EMP and FTIR) used to determine the total water water content of siliceous sinter.

Transformation from one phase to the next in silica maturation is thought to occur via a dissolution-reprecipitation pathway (e.g., Rice et al. 1995; Landmesser 1998) that is accompanied by water loss (e.g., Williams et al. 1985; Herdianita et al. 2000b; Campbell et al. 2001; Rodgers et al. 2004). With this type of mechanism comes a great potential for sedimentary fabric loss; invariably associated with the loss of valuable paleoecological information (e.g., Rodgers and Cressey 2001; Lynne and Campbell 2003, 2004; Jones et al. 2004; Lynne et al. 2005). Thus, it is important to strive for a more complete understanding of the diagenetic transformation of siliceous sinters at all levels, in both the physical (i.e. fabrics and microstructures) and compositional (i.e. mineralogy and water content) realms.

1.3 Samples

The following suite of samples represents a variety of siliceous sinter, composed of opal-A or opal-CT, such that a comparative analysis of fabrics, morphology and composition (i.e. water content) may be assessed from different locations:

- within a vent system,
- within a vertical temporal succession of sinter, and
- between geographically and climatically diverse hot spring environments.

1.3.1 Whakarewarewa, New Zealand

The Whakarewarewa geothermal area is located in the Taupo Volcanic Zone on the North Island of New Zealand (Fig. 1.1A, B). Covering an area of ~12 km^2 (Wood 1992), Whakarewarewa contains more than 500 thermal features, including active and dormant geysers and numerous hot springs (Llyod 1975). It lies near the southern margin of a roughly circular, ~15 km wide collapsed caldera (Llyod 1975) that formed when the Mamaku Ignimbrite was ejected between 140 ka (Murphy and Seward 1981) to 220 ka (Glover and Mroczek 1998). Samples from the Waikite Geyser complex, Geyser Flat, and Te Anarata were used in this study (Fig. 1.1C).

Waikite Geyser has been dormant since March 1967 (Llyod 1975). Its eruptions once reached heights up to 15 m when the regional groundwater level was high (Llyod 1975). A drop in the local groundwater level following the erosion of Puarenga stream combined with the progressive withdrawal of geothermal fluids for local energy use from ~1920 to the mid-1980's have caused a general decline in spring and geyser activity in the Whakarewarewa area (Allis and Lumb 1992). The Waikite vent lies at the apex of a large terraced mound of siliceous sinter that covers an area of ~80 m^2 and is up to 20 m high (Fig. 1.1D). The Pareia vent is a small geyser that lies south of the Waikite vent (Fig. 1.1C, D) which has recently renewed its activity (Jones et al. 2001b). Water collected at the Pareia vent in May 2000 had a temperature of 78°C and pH of 9.2 (Jones et al. 2001b). Three representative samples from different locations from in the Waikite Geyser complex were chosen for detailed analyses; close to the main vent (NZ 592), between the two vents (NZ 603), and distal from the main vent (NZ 601) (Fig. 1.1D).

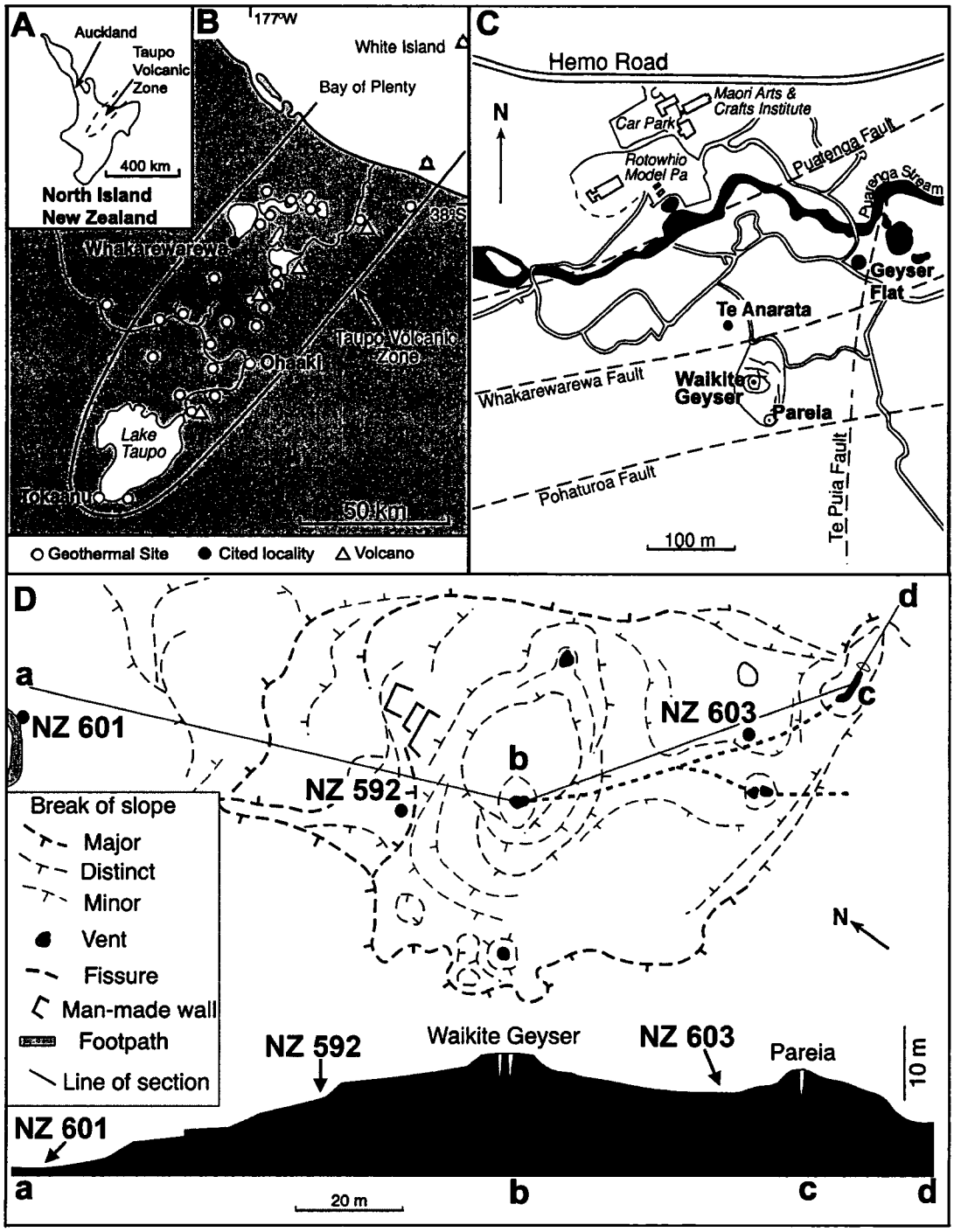

Figure 1.1. Map of North Island of New Zealand showing sample locations. Modified from Jones et al. 2001c. **A)** Taupo Volcanic Zone. **B)** Geothermal sites and volcanoes in Taupo Volcanic Zone. Samples for this study came from Whakarewarewa (solid dot). **C)** Location of Waikite Geyser vent, Pareia vent, Te Anarata, and Geyser Flat in Whakarewarewa geothermal area. **D)** Plan and cross section view of Waikite Geyser complex showing location of samples NZ 601, NZ 592, and NZ 603. Courtesy of B. Jones.

These samples consist of generally flat-lying to undulatory laminae of alternating dark and light coloured sinter.

Geyser Flat is a broad (~6000 m^2) platform of siliceous sinter located ~100 m northeast of the Waikite Geyser complex (Fig. 1.1C). Lying ~ 6 m above the Puarenga Stream, the siliceous sinter at Geyser Flat was formed by waters ejected by Mahanga, Waikorohihi, Te Horu, Pohutu, Prince of Wales Feathers, and Kereru geysers (Jones et al. 2001c). These geysers lie along the Te Puia Fault, which provides the main conduit for the hydrothermal waters reaching the surface (Llyod 1975). A densely laminated sample of geyserite composed of alternating layers of vitreous grey and white siliceous sinter was analyzed from this location (NZ 816).

Te Anarata is a succession of subfossil sinter located ~ 65 m northwest of the Waikite vent (Fig. 1.1C). The sinter at Te Anarata formed after the level of Lake Rotorua dropped and hydrothermal activity became established at Whakarewarewa (Jones et al. 2002). An alluvial deposit of ignimbrite and tephra (Oruanui Formation) that is ~22,500 years old, lies beneath the sinter samples provides a relative basis for dating the age of the samples. These sinter deposits are much older than those from Waikite (Jones et al. 2002). The samples chosen from the vertical succession highlight a range of ages relative to the dated tephra deposit; the sample closest to the tephra deposit represents the oldest sinter, whereas the sample farthest above the tephra deposit represents the youngest sinter (Fig. 1.2).

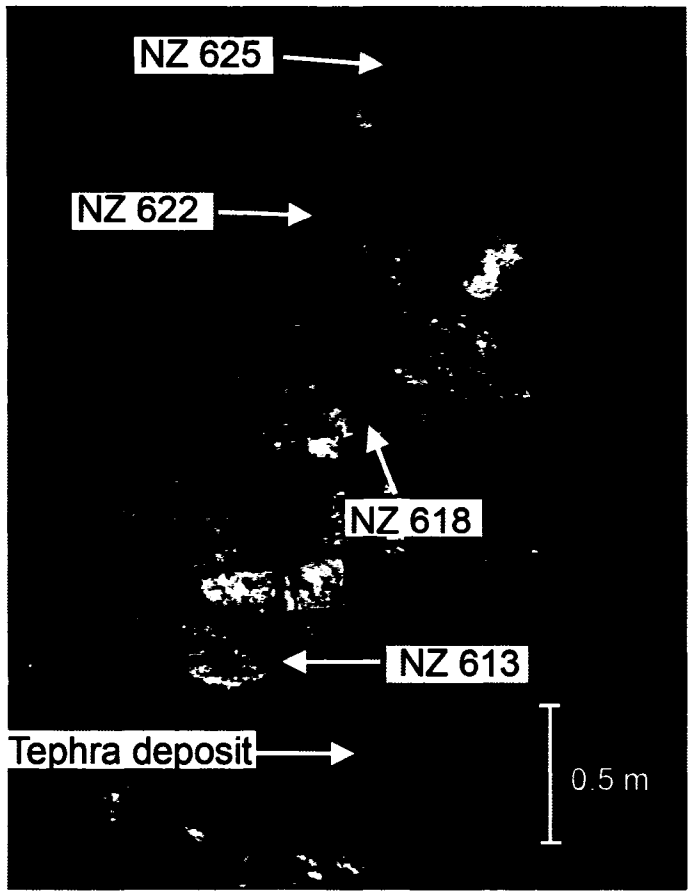

Figure 1.2. Field photograph of Te Anarata sinter succession in the Whakarewarewa geothermal area showing location of samples NZ 625, NZ 622, NZ 618, and NZ 613, overlying a tephra deposited ~ 22,500 years B.P. Photograph courtesy of B. Jones.

1.3.2 Geysir, Iceland

Geysir, situated in southwestern Iceland, is one of the world's most famous spouting hot spring (Fig. 1.3). It is credited for use of the term "geyser", which describes all hot springs that periodically erupt with an ejection of water and steam into the air. Geysir and about 50 other hot springs are found in an extensive area of siliceous sinter covering approximately 1 km^2 (Barth 1950) (Fig. 1.3). Palagonite, a heterogeneous formation consisting of tuffs and breccias of basaltic glass, and basaltic lava flows surround the Geysir region (Barth 1940; Pasvanoglu et al. 2000). This region is bound on the northwest by the rhyolitic dome Laugarfjall, which rises to 187 m and by the small river Beiná to the east and south (Barth 1950; Pasvanoglu et al. 2000).

The discharge apron around Geysir is a stratified dome-shaped mass of siliceous sinter that radiates ~200 m to the north and east of the vent pool (Barth 1940). The vent pool is ~1 m deep and 20 m across with a central feeder vent ~1 m in diameter that narrows as it extends to a depth of 23 m (Forbes 1860; Nielsen 1937; Pasvanoglu et al. 2000). Earthquakes have played a major role in determining the activity/dormancy of Geysir (Thorkelsson 1910; Nielsen 1937; Torfasson 1985; Pasvanoglu et al. 2000). Geysir's eruptive history has been irregular, at peak times of activity eruptions have reached up to 80 m high (Nielsen 1937; Barth 1940, 1950; Hróarsson and Jónsson 1992; Demissie 2003). Estimates using tephrachronology indicate that this geothermal area has been active for the last 10,000 years (Torfasson 1985).

The samples chosen for analysis were taken from a measured section on the west side of the Geysir discharge apron and indicate a mineralogical boundary between opal-A and opal-CT (Fig. 1.4).

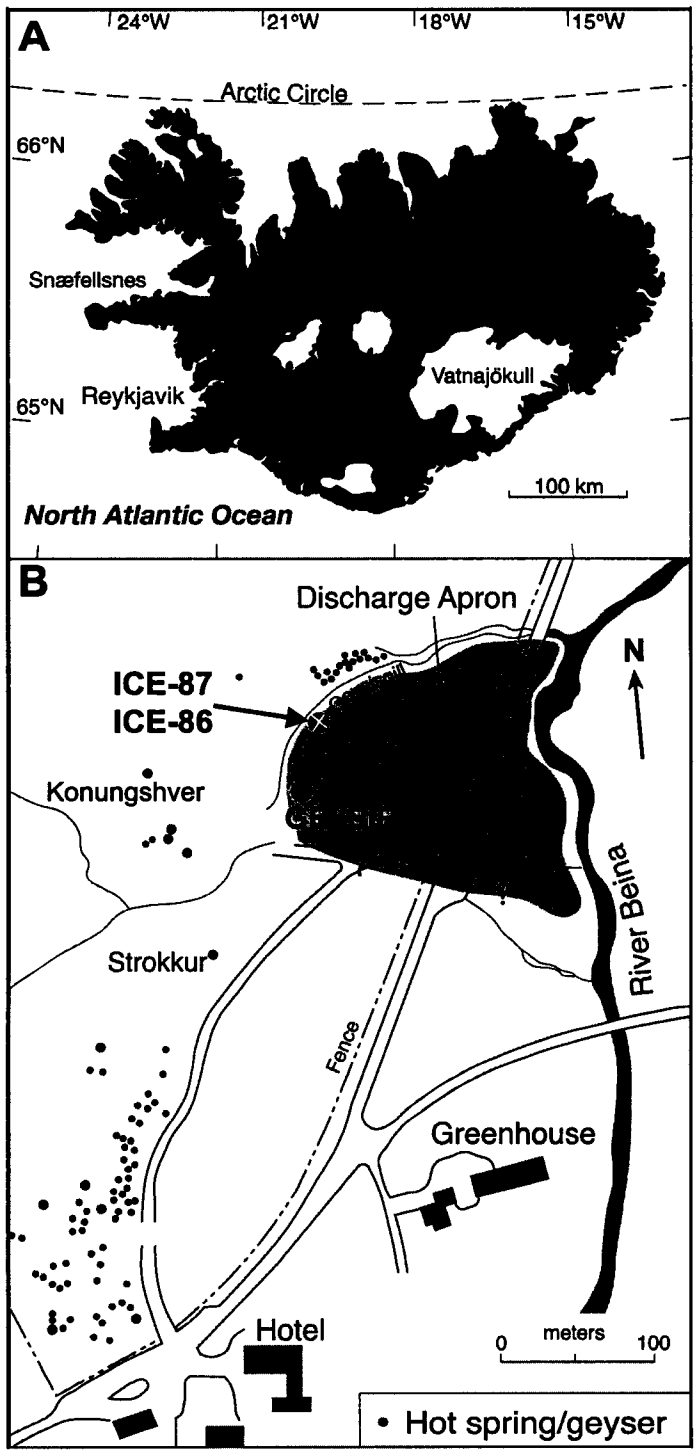

Figure 1.3. Map of Geysir, Iceland showing sample locations. Modified from Jones and Renaut, in press. **A)** Location of Geysir in southern Iceland. **B)** Location of samples ICE-87 and ICE-86 on west side of Geysir discharge apron. Question marks indicate uncertain southern boundary.

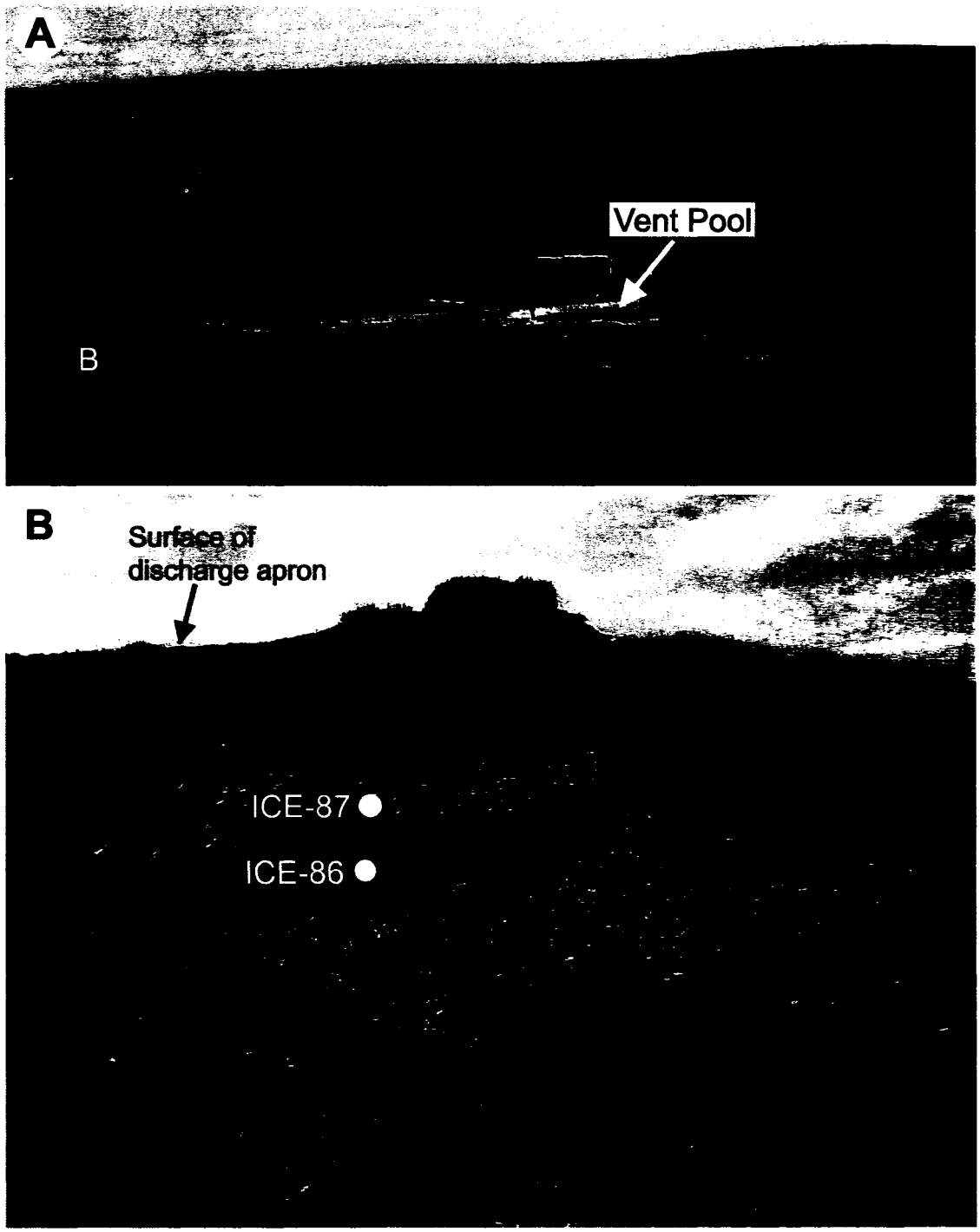

Figure 1.4. A) General view of Geysir discharge apron, looking to the east, showing sample location (Letter B) with respect to vent pool. Letter B indicates position of Fig. 1.4B. **B)** Location of samples ICE-87 (opal-A) and ICE-86 (opal -CT). Section G1 in Jones and Renaut (in press). Photographs courtesy of B. Jones.

Chapter Two – Methodology and Terminology

2.1 Mineralogy and Morphology

2.1.1 X-ray Diffraction

The mineralogy of each sample was determined by XRD analyses on a Rigaku Geigerflex 2173 sealed-tube X-ray generator with a Co tube. All samples were dried and hand ground using an agate mortar and pestle. Approximately 1 g of ground sample was used to fill a backpack sample container, which was scanned at 2° 2θ/min with a step size of 0.05° from 2 to 90° 2θ with operating conditions of 40 kV and 30 mA. This type of scan setting was preformed to assess the overall mineralogy of the sample. A small amount of halite was added to each sample, in order to standardize and accurately compare diffractograms with each other, and samples were scanned at 0.6° 2θ/min with a step size of 0.01° from 10° to 40° 2θ with operating conditions of 40 kV and 30 mA (Herdianita et al. 2000a; Smith et al. 2003; Jones and Renaut, in press). These scans were converted to those from a Cu source by using a subroutine in the computer software that operates the Rigaku Geigerflex X-ray as most studies of opal in sinters have employed X-ray machines with a Cu tube (e.g., Herdianita et al. 2000a, 2000b; Rodgers and Cressey 2001; Rodgers et al. 2002, 2004; Smith et al. 2003; Lynne et al. 2005). A characteristic XRD pattern for opal-A is recognized by a prominently diffuse band centered at about 4Å (~22.2° 2θ CuK_α) (Jones and Segnit 1971; Flörke et al. 1991; Graetsch 1994; Smith 1998) (Fig. 2.1A). The presence of a well defined broad hump in the 22.2° 2θ (CuK_α) region accompanied by a satellite peak on the low-angle side and a shoulder on the high angle side characterize the XRD pattern of opal-CT (Jones and Segnit 1971; Graetsch 1994; Smith 1998; Herdianita et al. 2000b) (Fig. 2.1B).

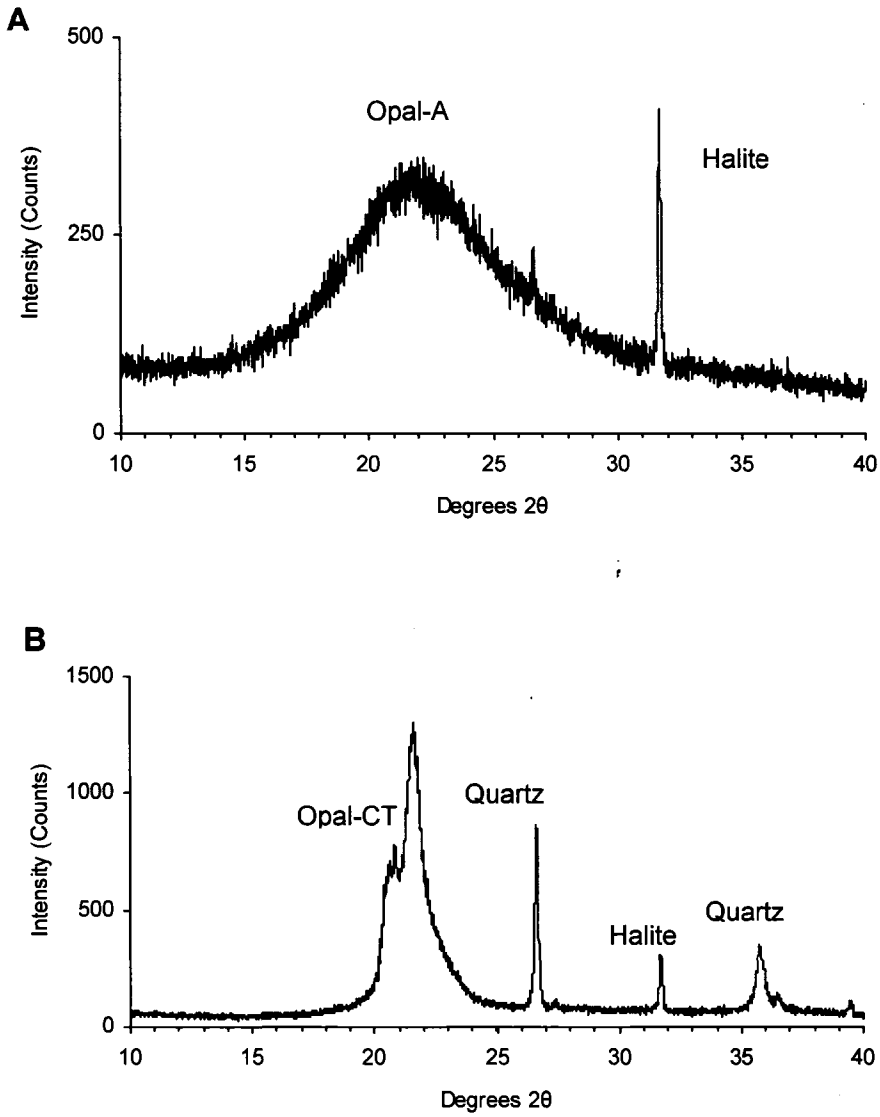

Figure 2.1. A) Representative broadband XRD diffraction pattern of opal-A (sample NZ 592). **B)** Representative sharp peaked XRD diffraction pattern of opal-CT and quartz (sample NZ 816). Halite was added to XRD samples as an internal standard.

2.1.2 Macroscale Observations

Hand sample examination was used to describe macroscopic textures and fabrics of the sinter samples. Corresponding thin sections (2.5 × 4.5 cm) were examined using transmitted light microscopy. Based on these observations, each sample was divided into laminae of different types of sinter for detailed analysis of sinter morphology and water content.

2.1.3 Siliceous Sinter Terminology

Considerable attention has been given to categorizing sinter facies and describing structures related to the preservation of biota (e.g., Walter 1976; Cady and Farmer 1996; Jones et al. 1998, 2000, 2002; Braunstein and Lowe 2001; Guidry and Chafetz 2003a, 2003b; Lowe and Braunstein 2003). In comparison, little heed has been given to developing terminology that easily and adequately portrays the macroscopic appearance of different types of siliceous sinter. Although the terminology used here to describe the macroscopic appearance of siliceous sinter generally follows that used by Campbell et al. (2001) and Lynne and Campbell (2003, 2004), there are several important differences. The practice of Campbell et al. (2001) and Lynne and Campbell (2003, 2004) to include terms that reflect the mineralogy (i.e. opal-A, opal-CT) and microstructures of their samples, for example, is not followed in this study. Siliceous sinters are known to be highly variable at both the macroscopic and microscopic level (Campbell et al. 2001; Jones and Renaut 2003b, in press; Rodgers et al. 2004). Thus, there is concern that a scheme which classifies sinter based on a combination of highly variable features such as mineralogy, macroscopic appearance, and microstructures may lead to unfitting

associations of these characteristics and ultimately a misconception of sinter formation and diagenesis. Instead, the sinter is named here by the use of descriptive terms that reflect only the physical appearance of the sinter. Notably the term "sinter" is used here instead of the term "silica" as used by Campbell et al. (2001) and Lynne and Campbell (2003, 2004). The term sinter better reflects the many facets of these siliceous deposits, which include accessory minerals and detrital components of lithological and biological origin (Jones and Renaut 2003b).

The term "friable" is used to describe sinter that crumbles or breaks apart easily (Fournier 1985; Campbell et al. 2001; Lynne and Campbell 2004). The terms used to describe the variable cohesiveness of sinter (extremely, very, moderately and barely friable, and indurated) follow the usage of Lynne and Campbell (2004). They used a simple qualitative scratch test: for example, an "extremely friable" sinter must be handled with great care in order to avoid crumbling whereas an "indurated" sample is hard and requires a hammer to break it (Table 2.1).

"Dull" and "vitreous" are used here to describe the luster of the sinter; dull appears matt and reflects lightly poorly, whereas vitreous signifies a shiny or glassy appearance.

The term "porous" is used as a qualitative descriptor of the sinter to indicate a visible abundance of macroscopic pores. Conversely, "non-porous" describes a complete lack of macroscopic pore space in the sinter. Adjectives (e.g. very, slightly) are used to modify the degree of porosity observed.

Table 2.1. Friability classification. Based on classification derived from Lynne and Campbell (2004).

Descriptive Terms	Field Scratch Test
Extremely friable	Sample cannot be handled without crumbling, or can be handled with care but easily crumbles
Very friable	Sample can be handled with care and does not crumble readily in fingers
Moderately friable	Can handle without crumbling. Easily scratched with fingernail.
Barely friable	Can handle without crumbling. Can barely scratch with fingernail.
Indurated	Cannot scratch with fingernail. Requires hammer blows to break sample.

The five types of sinter named this study are (1) porous friable sinter, (2) dull indurated sinter, (3) porous indurated sinter, (4) vitreous sinter, and (5) patchy vitreous sinter.

- **Porous friable sinter** is generally white to beige in colour, fine-grained, porous, and has a dull luster. Used here, it describes extremely to moderately friable sinter (cf. Lynne and Campbell (2004) included only extremely and very friable, not moderately friable). By including moderately friable sinter to describe porous friable sinter, the use of Lynne and Campbell (2004)'s term "transitional fabric", which is distinguished from other sinter fabrics by mineralogy and microstructures, is avoided. Porous friable silica feels gritty to the touch and a chalky power is left on fingers after handling (Campbell et al. 2001; Lynne and Campbell 2003, 2004).
- **Dull indurated sinter** is used to describe sinter that is barely friable to indurated. It is white, beige or grey in colour with a dull luster and ranges from slightly

porous to non-porous. This term also avoids use of Lynne and Campbell (2004)'s "transitional fabric" or "primary smooth fabric", which are associated mainly with microstructures and mineralogy.

- **Porous indurated sinter** describes highly porous sinter that is barely friable to indurated. Due to its highly porous nature this type of sinter has a rough appearance. Lynne and Campbell (2004) described this type of sinter as having a dull luster; used here this type of sinter generally has a vitreous luster. It is generally dark in colour ranging from beige to grey. The use of the term here, unlike in Lynne and Campbell (2004), does not imply a diagenetic state, mineralogy or specific microstructures.
- **Vitreous sinter** is used to describe smooth, non-porous, and well-indurated sinter that has a shiny or glassy luster (Fournier 1985; Campbell et al. 2001; Lynne and Campbell 2003). It is typically transparent, grey, or white in colour. It is commonly found as thin distinct laminae that alternate with porous friable silica (Campbell et al. 2001). The boundary between vitreous sinter and neighboring sinter types is characteristically sharp and well-defined.
- **Patchy vitreous sinter** describes sinter with a vitreous luster that is moderately to barely friable and slightly to highly porous. It forms either discontinuous or continuous laminae. The boundary between patchy vitreous sinter and other types of sinter is typically gradational and merges into other types of sinter such as porous friable sinter. Cambell et al. (2001) and Lynne and Campbell (2003, 2004) used the term "secondary vitreous silica" to describe this type of sinter, which they associated with the diagenesis of porous friable silica. The term

patchy vitreous sinter better describes the macroscopic appearance of the sinter while avoiding the implications of a diagenetic origin.

2.1.4 Scanning Electron Microscope

Small fractured samples were mounted on stubs and sputtered coated with a thin layer of gold for examination on a JEOL 6301FE field emission scanning electron microscope (SEM) with an accelerating voltage of 5 kV. To reduce problems of charging, colloidal silver glue was run from the stubs up the sides of the mounted samples in order to improve conductivity (cf. Jones et al. 2001b). High resolution photomicrographs were obtained for each lamina in each sample of sinter. The elemental composition of selected spots was verified by energy dispersive X-ray (EDX) analysis on the SEM with an accelerating voltage of 20 kV.

2.1.5 Microstructure Terminology

The terminology used for describing microstructures found in siliceous sinter has yet to be clearly and consistently defined. As such, the terms used in this study are thoroughly outlined.

Spheres, ~ 200 nm to 15 μm in diameter, are a widely recognized feature of opal-A (e.g., Darragh et al. 1966; Jones and Segnit 1969; Flörke et al. 1991; Graetsch 1994) and siliceous sinter deposits (e.g., Cady and Farmer 1996; Jones et al. 1998, 1999; Campbell et al. 2001; Guidry and Chafetz 2003b; Smith et al. 2003; Lynne and Campbell 2004). Spheres characteristically have smooth external surfaces (Fig. 2.2A). Other

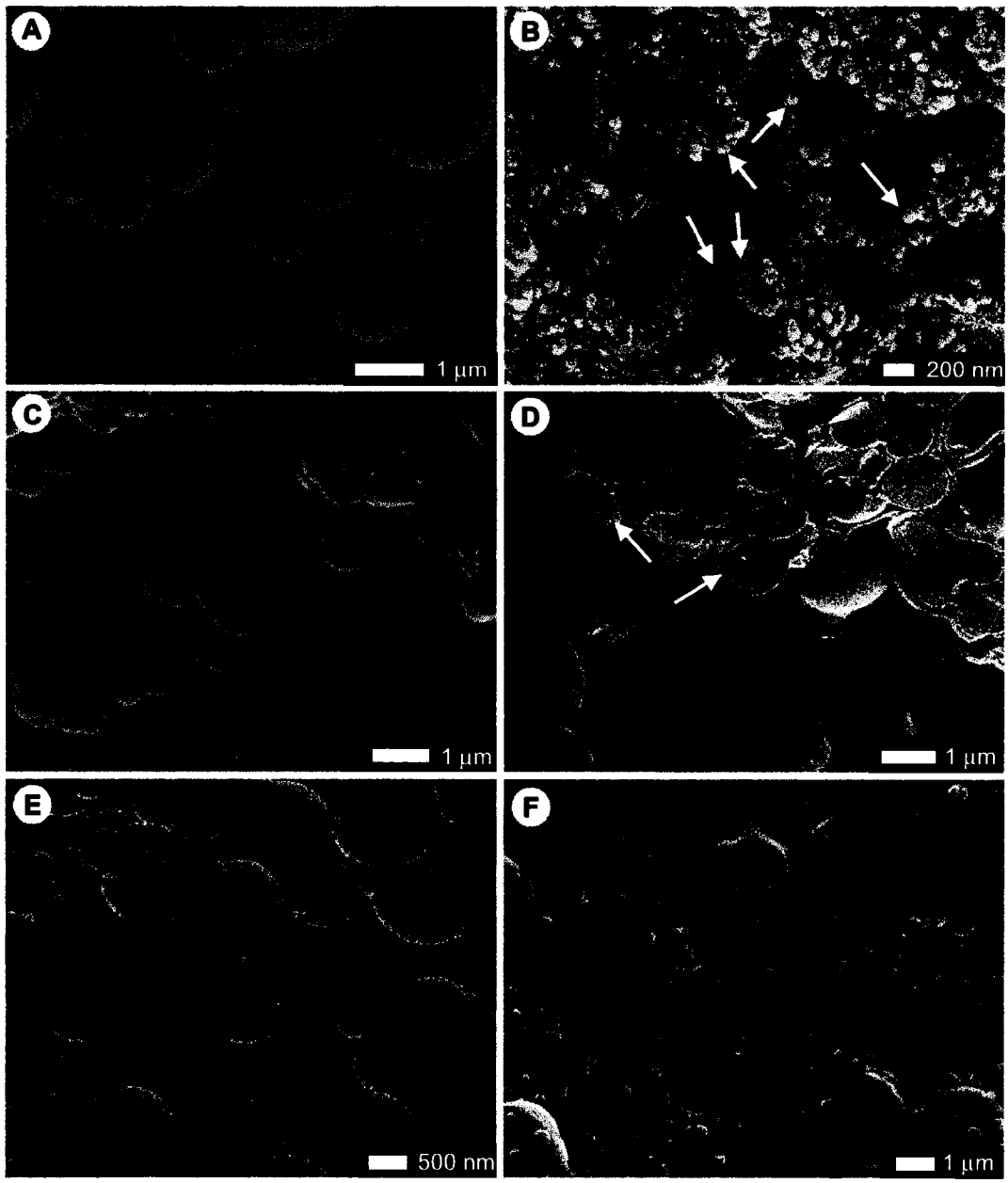

Figure 2.2. Terminology. **A)** Spheres, sample NZ 592. **B)** Nanospheres, sample NZ 816. **C)** Multilobed masses of spheres, sample NZ 592. **D)** Cement, sample NZ 592. **E)** Type I inverse opal, sample NZ 618 **F)** Nodular spheres, sample NZ 622.

terms, such as "spheroids" (Jones and Renaut 2003b) and "microspheres" (Lynne et al. 2005), have also been used to describe such spheres. The term "sphere" is used herein.

Spheres may vary in their arrangement and size. They may be found as discrete, individual spheres (Fig. 2.2A) or they may clump together to form "multilobed masses" (Fig. 2.2C) (Jones and Renaut in press). The term "botryoidal clusters" has also been used to describe such features (Flörke et al. 1991; Lynne and Campbell 2004); however, the term "multilobed masses" is used herein. The term "nanosphere" is used to distinguish spheres less than ~125 nm in diameter (Fig. 2.2B) (Lynne et al. 2005).

Spheres may be covered by a smooth coating of silica cement (Jones and Renaut 2003b); most evident in cross-section view (Fig. 2.2D). Preferential dissolution of the original spheres may occur, leaving behind the silica cement (Fig. 2.2E); Jones and Renaut (in press) called this "Type I inverse opal". "Type II inverse opal" is used here, as in Jones and Renaut (in press), for the microtexture resulting from preferential dissolution of the cement, leaving behind the original spheres.

Spheres may be modified with external ornamentation and by their connection style (Jones and Renaut in press). "Nodular spheres", termed here, display an irregular surface of smooth sub-spherical to elongated nodules (~250 nm wide) protruding from the surface of otherwise smooth spheres (Fig. 2.2F). The term "spiky spheres" is used here for spherical features with protruding pointed nodules (Fig. 2.3C). The term "bumpy spheres" is used here as in Lynne et al. (2005), although its use here does not imply the diagenetic origin as given by Lynne et al. (2005). Bumpy spheres differ from nodular and spiky spheres in that their entire surface is knobby and irregular (Fig. 2.3D).

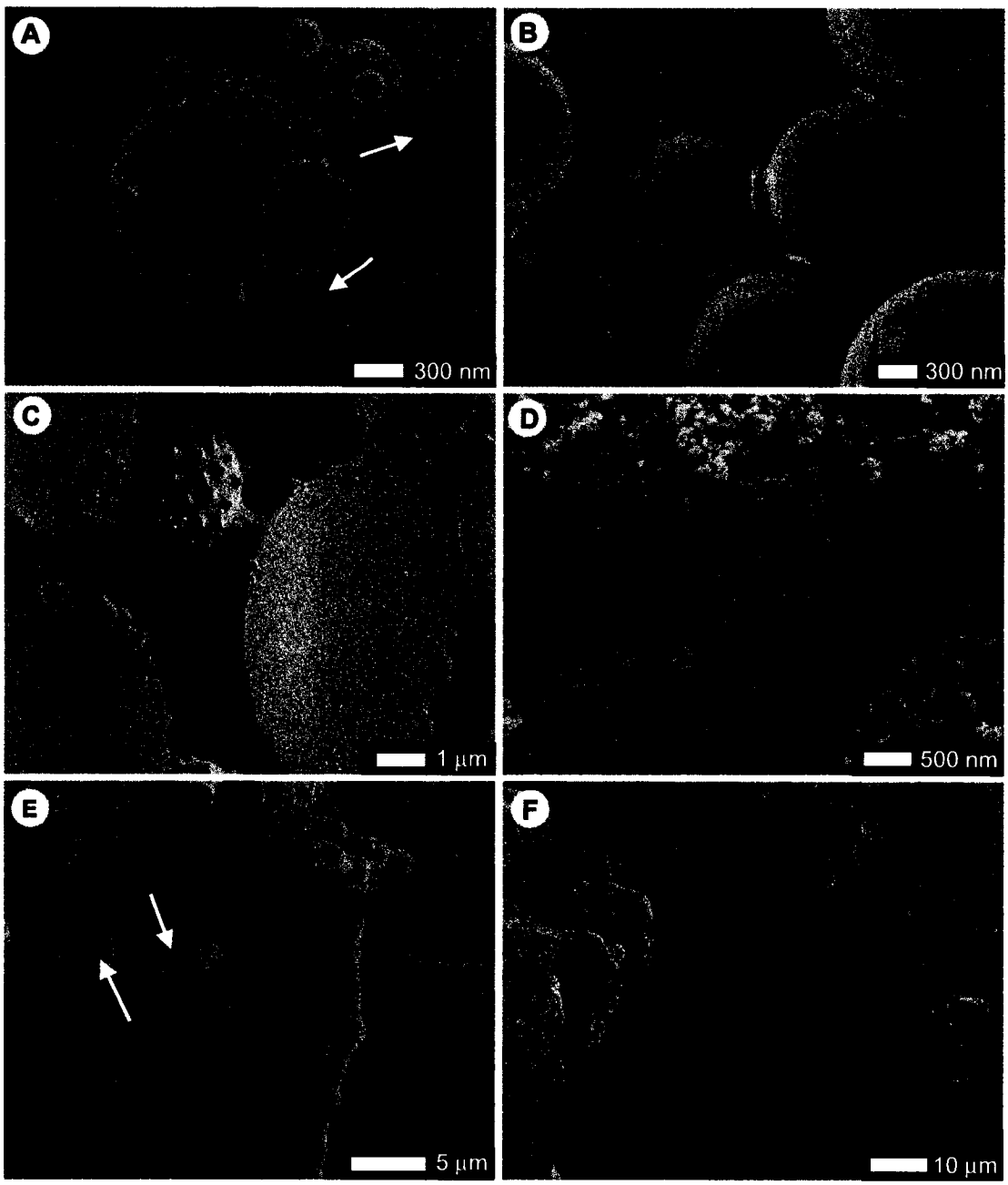

Figure 2.3. Terminology. **A)** Connections pads indicated with black arrows and necks indicated with white arrows, sample NZ 625. **B)** Ringed necks, sample NZ 592. **C)** Spiky spheres, sample NZ 601. **D)** Bumpy spheres, sample NZ 816. **E)** Silicified microbes, characteristic hollow open tubes indicated with white arrow, sample NZ 592. **F)** Pollen grain (?), sample NZ 601.

Connection pads are small, 200-300 nm in diameter, ovate to circular pads that join neighbouring spheres (Jones and Renaut in press). Connections pads are most evident where one sphere has been pulled away from another sphere (Fig. 2.3A, black arrows). The term "neck" describes thin strands of connective silica between spheres (Fig. 2.3A, white arrows) (Jones and Renaut 2003b). The term "ringed neck" describes a disc of silica around necks of connecting spheres (Fig. 2.3B).

Silicified microbes are prominent in many siliceous sinters (e.g., Cady and Farmer 1996; Jones et al. 1998, 1999, 2001a, 2004; Guidry and Chafetz 2003b; Smith et al. 2003; Lynne and Campbell 2004). Silicified microbes may be identified using a variety of features such as hollow open tubes, which indicate the space once occupied by filamentous microbes (Fig. 2.3E) (Jones et al. 2001a).

Spores, the reproductive units of many plants, are identified in siliceous sinter by their generally spherical nature (> 2 μm in diameter) and connection stalk (Jones et al. 1999). Pollen grains are large spherical bodies, ~ 24-60 μm in diameter, that appear hollow and are commonly collapsed or deformed (Fig. 2.3F) (Jones et al. 1999; Jones and Renaut 2003b). Plant material, such as twigs and grass stems, and insects, such as beetles and small flies, generally appear unaltered from silica encasement (Jones and Renaut 2003b).

The term "isopachous laminae" is applied here to silica cement displaying thin (< 100 nm thick) laminae (Fig. 2.4A) (Jones and Renaut 2003b, in press). This feature is formed by successive precipitation of opal cement with each layer mimicking the topography of the underlying substrate. Differential etching on these surfaces by rising steam and sulphurous gases highlight isopachous laminae.

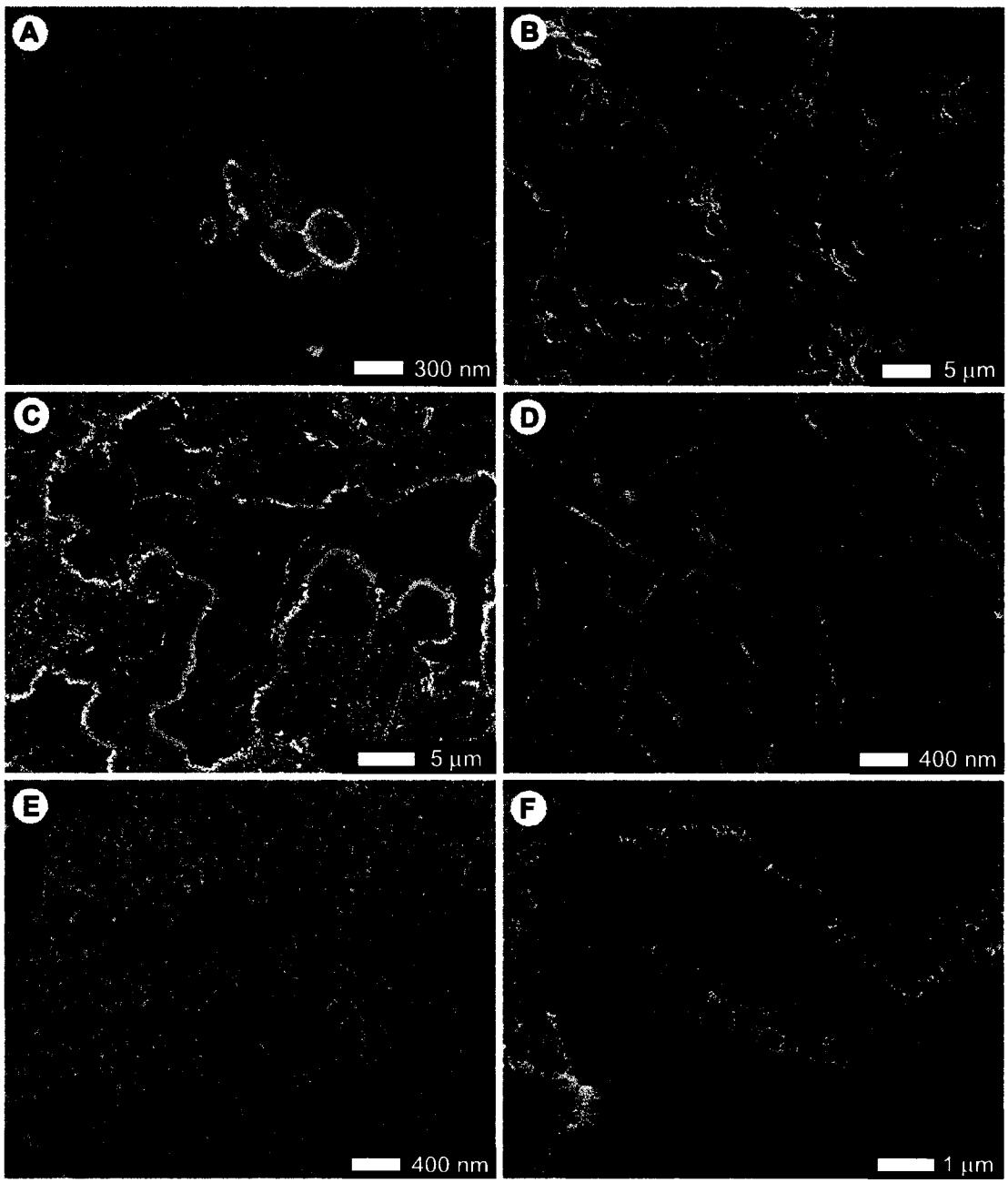

Figure 2.4. Terminology. **A)** Isopachous laminae, sample NZ 622. **B)** Scalloped surface, sample NZ 603. **C)** Lepispheres, sample NZ 816. **D)** Platelets, sample NZ 816. **E)** Knobby lepispheres, sample NZ 622. **F)** Silica divots, sample NZ 816.

The term "scalloped surface" describes a silica surface with a pitted appearance (Fig. 2.4B) (Jones and Renaut 2003b). Scalloped surfaces are attributed to natural etching via preferential dissolution of silica by rising steam and sulphurous gases. These features have been replicated by artificially etching siliceous sinter with dilute HF acid (Jones and Renaut 2003a, b). Lynne and Campbell (2003; their Fig. 5C, D) used the term "porous silica" to describe what is termed here as a scalloped surface, and attribute this feature to silica infilling. The term "scalloped surface" will be used herein as opposed to the term "porous silica".

Spherical aggregates, generally ~ 5-10 μm in diameter, composed of small intersecting "platelets" (~ 1 μm long, < 50 nm thick) form "lepispheres" (Fig. 2.4C, D), the most commonly illustrated feature of opal-CT (e.g., Segnit et al. 1970; Flörke et al. 1975; Kastner et al. 1977; Elzea et al. 1994; Graetsch 1994; Herdianita et al. 2000b; Campbell et al. 2001). The term platelet is to describe only features that exhibit a well-defined platy habit (Fig. 2.4D). Other terms such as "plates" (e.g., Jones and Renaut in press) and "blades" (e.g., Graetsch 1994; Rodgers et al. 2002, 2004) have also been used to describe platelets. The motivation for the use of these different terms is unclear as they essentially describe the same feature. The term "platelet" will be used herein. The platelets, which form lepispheres, typically have somewhat ragged edges and form 3-D skeletons ("house-of-card" structures) intersecting each other at angles between 40° and 60° (Fig. 2.4D) (Flörke et al. 1991; Rodgers et al. 2004).

Relatively few authors (Rodgers et al. 2002; Lynne and Campbell 2004; Rodgers et al. 2004; Lynne et al. 2005) have acknowledged that lepispheres are variable microstructures (Fig. 2.4D vs. 2.4E). Terms used to date for variations in the quality and

arrangement of platelet-like structures forming lepispheres include "incipient 'fuzzy' lepispheres" (Lynne and Campbell 2004) or simply "incipient lepispheres" (Rodgers et al. 2002). Rodgers et al. (2002) described incipient lepispheres as "...subspherical masses covered by raised surface lumps rather than the typical blades...", whereas others have described such features as "...oriented rows of sub-aligned nanospheres..." (Lynne et al. 2005, their Fig. 7b) and as "...blades that broaden abruptly to terminate in microclumps of silica..." (Rodgers et al. 2004, their Fig. 24E). Lynn and Campbell (2004, their Fig. 8D-E) did not provide a text description of their term, incipient "fuzzy" lepispheres, only an illustration that closely resembles what is later termed bumpy spheres (Lynne et al. 2005, their fig. 6C, D). Nevertheless, the term incipient lepispheres implies that these features are in the early stages of lepisphere development. Until a better understanding of the origins of these microstructures is attained, it is critical that terms are used only to describe the appearance of such features without alluding to their origins. The term "knobby lepispheres" will, therefore, be used herein to describe spherical aggregates composed of ordered intersecting "microclumps" of silica (Fig. 2.4E), whereas the term lepisphere will be used only for such features composed of platelets (Fig. 2.4C, D).

Other features associated with lepispheres include stacked divot-like features (~ 0.5 μm thick, ~ 2 μm in diameter) formed of intersecting elongated rods (~ 30 nm thick, 100-400 nm long) (Fig. 2.4F). These microstructures are termed here "silica divots". The surrounding groundmass of cavities lines with lepispheres is commonly formed of what Jones and Renaut (in press) refer to as "intercalated plates". For the sake of consistency with the terms used in this study, these features will be termed "intercalated

platelets". This microtexture is characterized by rectangular- to square-shaped micropores (Jones and Renaut in press).

2.2 Water Content

2.2.1 Backscattered Electron Images and Electron Microprobe Analysis

Backscattered electron images (BSEI) were obtained from carbon coated polished thin sections (2.5 × 4.5 cm) on a JEOL 8900R electron microprobe (EMP). On BSEI, different grey levels reflect differences in the average atomic weights of the precipitates. Each image has 64 grey levels with the lighter greys indicating higher average atomic weights. Grey levels are calibrated from each image; therefore, specific grey levels cannot be equated to average atomic weights from one image to the next (Jones and Renaut 2004). The elemental composition of the samples was determined using EMP analysis with an accelerating voltage of 15 kV, a 10 nA beam current, a 3-5 μm beam diameter, a 10 second count time on Si and O peaks, and 2 second count time on backgrounds. The data were reduced using the ZAF program, a correction routine for oxides, provided by JEOL.

EMP analyses were preformed on sinter samples in order to determine microscale variations in the total water content of opal ($SiO_2 \cdot nH_2O$). This can only be accomplished in the absence of other elements. In addition to Si and O, trace elements (Ca, Mg, Al, Na, Fe, Mn, and K) were analysed to ensure that BSEI of the sinters was not reflecting differences in average atomic weights caused by variations in trace element distribution. Each lamina in each sample was imaged using BSEI to determine light and dark grey

areas, referred to herein as light and dark grey opal (BSEI), and subsequently analyzed using EMP analysis in order to obtain a representative average of the total water content.

The EMP was programmed to measure Si and O independently in order to calculate the amount of excess O. Using the 1:2 ratio of Si:O for anhydrous silica (SiO_2), any oxygen in excess of this ratio can be used as a proxy for the total water content (molecular water + silanols) present in hydrous silica ($SiO_2 \cdot nH_2O$) (Jones and Renaut 2004). The weight percentages (wt %) of Si and O were not normalized, but used as measured, to calculate total water content. Analyses with totals less than 90 wt % were discarded as they likely represent areas of high microporosity and/or beam damage to the sample. Generally the sum of non-volatile impurities does not exceed 1-2 wt % in non-crystalline silica minerals (Flörke et al. 1991). Analyses with trace element concentrations higher than 1 wt % were not used to calculate water contents; such analyses do not provide an accurate representation of total water content as determine using this method.

The calculations for the determination of total water content using the Si:O ratio found with EMP analysis are given below:

1. *Using measured Si and O weight percentages, 100 grams (g) of substance is assumed:*

   43.92 wt % Si = 43.92 g Si
   53.84 wt % O = 53.84 g O
   Total Si + O = 97.76 g

   Any remaining mass (2.24 g) is attributed to a combination of hydrogen (mainly) and trace elements.

2. *Moles of Si and O are determined*:

$$\frac{\text{mass of substance}}{\text{molar mass}} = \text{moles}$$

$$\frac{43.92 \text{ g Si}}{28.0855 \text{ g.mol}^{-1} \text{ Si}} = 1.56 \text{ mol Si}$$

$$\frac{53.84 \text{ g O}}{15.994 \text{ g.mol}^{-1} \text{ O}} = 3.37 \text{ mol O}$$

3. *The amount of excess O is determined*:
The molar ratio of Si:O in silica (SiO_2), which contains no water, is 1:2. If the molar ratio of Si:O is greater than 1:2 than excess O is assumed to represent O present in the water portion of the hydrated silica ($SiO_2 \cdot nH_2O$).

$$x \text{ mol O} - 2y \text{ mol Si} = \text{mol excess O}$$
$$3.37 \text{ mol O} - 2 \times 1.56 \text{ mol Si} = 0.25 \text{ mol excess O}$$

4. *Moles of H_2O (n) are determined*:
To determine n, mol excess O is normalized to mol Si; in each mol of $SiO_2 \cdot nH_2O$ there is one mol Si.

$$\frac{\text{mol excess O}}{\text{mol Si}} = n \text{ mol } H_2O$$

$$\frac{0.25 \text{ mol excess O}}{1.56 \text{ mol Si}} = 0.16 \text{ mol } H_2O$$

5. *Mass of H_2O is determined:*

$$n \text{ mol } H_2O \times \text{molar mass } H_2O = \text{mass } H_2O$$
$$0.16 \text{ mol } H_2O \times 18.015 \text{ g.mol}^{-1} H_2O = 2.89 \text{ g } H_2O$$

6. *Mass of opal is determined:*
Weight of $SiO_2 \cdot nH_2O$ varies according to n.

$$\text{mass of 1 mol } SiO_2 + \text{ grams } H_2O = \text{mass of opal}$$
$$60.084 \text{ g } SiO_2 + 2.89 \text{ g } H_2O = 62.97 \text{ g opal}$$

7. *Total water content (wt % H_2O) in opal is determined:*

$$\frac{\text{mass } H_2O}{\text{mass opal}} \times 100 = \text{wt \% } H_2O$$

$$\frac{2.89 \text{ g } H_2O}{62.97 \text{ g opal}} \times 100 = 4.6 \text{ wt \% } H_2O$$

The average total water content was determined with respect to light and dark opal (BSEI), if present, in each lamina. If the sinter appeared homogeneous on BSEI, random points were chosen and the average total water content was determined.

The error reported for these calculations was determined through propagation of uncertainty (Bevington 1969; Harris 1987). The standard error of the mean ($e = \frac{\sigma}{\sqrt{N}}$, where σ is the standard deviation and N is the sample size) was used to represent the error of the average total water contents. When determining the error for a calculation it is necessary to consider both precision and accuracy. The precision (e_{sample}) was determined using the mean (μ) and *e* of Si and O measured in each lamina. Following ~ 50 analyses, 3 randomly selected spots on the quartz standard were measured as a means of monitoring analytical accuracy. The accuracy ($e_{quartz\ standard}$) was found using μ of the total weight % measured on the quartz standard. Adjustments to the calculated total water content were made in instances where the average total weight % of the point measurements of the quartz standard was ± 1 wt % difference from 100 wt %. For example, if the average total weight % of the point measurements of the quartz standard was 103.5 wt %, the sample measurements prior to the quartz standard were adjusted by 3.5 wt %. The reported final error (e_{Total}) is: $e_{Total}^2 = (e_{quartz\ standard})^2 + (e_{sample})^2$

The following sample calculation of error propagation is provided:

1. *Using μ and e of Si wt % and O wt %, e_{sample} is determined*:

   41.49 wt % Si ± 0.39 wt % = 41.49 g Si ± 0.39 g
   50.36 wt % O ± 0.33 wt % = 50.36 g O ± 0.33 g

2. *Moles of Si and O are determined*:

$$\frac{41.49\ \text{g Si} \pm 0.39\ \text{g}}{28.0855\ \text{g.mol}^{-1}\ \text{Si}} = 1.48\ \text{mol Si} \pm 0.01\ \text{mol}$$

$$\frac{50.36 \text{ g O} \pm 0.33 \text{ g}}{15.994 \text{ g.mol}^{-1} \text{ O}} = 3.15 \text{ mol O} \pm 0.02 \text{ mol}$$

3. *Using propagation of uncertainty (addition or subtraction), moles of excess O are determined:*

$$x = u \pm bv$$
$$e_x^2 = e_u^2 + b^2 e_v^2$$

$$\text{excess mol O} = x \text{ mol O} - 2y \text{ mol Si}$$
$$\text{excess mol O} = 3.15 \text{ mol O} \pm 0.02 - 2(1.48 \text{ mol Si} \pm 0.01)$$

$$e_{\text{excess mol O}}^2 = e_{\text{mol O}}^2 + 2^2 e_{\text{mol Si}}^2$$
$$e_{\text{excess mol O}} = \sqrt{0.02^2 + 2^2(0.01)^2} = 0.028 = 0.03 \text{ mol}$$

$$\text{excess mol O} = 0.19 \text{ mol} \pm 0.03$$

4. *Using propagation of uncertainty (division), moles of H_2O (n) are determined:*

$$x = \pm a\frac{u}{v}$$
$$(\%e_x)^2 = (\%e_u)^2 + (\%e_v)^2$$

$$n \text{ mol } H_2O = \frac{\text{mol excess O}}{\text{mol Si}}$$
$$n \text{ mol } H_2O = \frac{0.19 \text{ mol excess O} \pm 0.03}{1.48 \text{ mol Si} \pm 0.01}$$

$$(\%e_{n \text{ mol } H_2O})^2 = (\%e_{\text{mol excess O}})^2 + (\%e_{\text{mol Si}})^2$$

$$\%e_{n \text{ mol } H_2O} = \sqrt{\left(\frac{0.03}{0.19} \times 100\right)^2 + \left(\frac{0.01}{1.48} \times 100\right)^2} = 15.8 \ \%e$$

$$e_{n \text{ mol } H_2O} = 0.13 \text{ mol } H_2O \times 15.8 \ \%e = 0.02$$
$$n \text{ mol } H_2O = 0.13 \text{ mol } H_2O \pm 0.02$$

5. *Mass of H_2O is determined:*

$$0.13 \text{ mol } H_2O \pm 0.02 \times 18.015 \text{ g.mol}^{-1} H_2O = 2.36 \text{ g } H_2O \pm 0.37$$

6. *Using propagation of uncertainty (division), the total water content (wt % H_2O) in opal is determined:*

$$\frac{\text{mass } H_2O}{\text{mass opal}} \times 100 = \text{ wt \% } H_2O$$

$$\frac{2.36 \text{ g } H_2O \pm 0.37}{62.97 \text{ g opal} \pm 0.37} \times 100 = \text{wt \% } H_2O$$

$$\%e_{\text{wt\%}H_2O} = \sqrt{\left(\frac{0.37}{2.36} \times 100\right)^2 + \left(\frac{0.37}{62.44} \times 100\right)^2} = 15.7 \ \%e$$

$$e_{\text{wt\% } H_2O} = 3.78 \text{ wt \% } H_2O \times 15.7 \ \%e = 0.59$$
$$wt\% \ H_2O = 3.78 \text{ wt \% } H_2O \pm 0.59$$

This is the error determined for the precision of the measurement (e_{sample}).

7. *Based on 3 point measurements of the quartz standard, $e_{\text{quartz standard}}$ is determined:*

Total wt % measured on quartz standard:
100.02
98.63
99.23

$\mu = 99.29$ wt %
$e = 0.41$

8. *The errors determined are combined:*

$$e_{\text{Total}}^2 = (e_{\text{quartz standard}})^2 + (e_{\text{sample}})^2$$
$$e_{\text{Total}} = \sqrt{(0.59)^2 + (0.41)^2} = 0.72$$

Thus, the reported value for the total water content in this example is 3.8 wt % ± 0.7.

2.2.2 Micro-Fourier Transform Infrared Spectroscopy

Thin sections were prepared from sinter samples using the immediately opposing face of the slides prepared for EMP analysis, so as to minimize spatial variability when determining water contents. Thin sections were polished on both sides and ground to thicknesses ranging from 100-500 μm. The thin sections were removed from the glass

slides by immersing them in acetone to dissolve the adhesive (loctite 495 instant adhesive super bonder). Samples were cleaned in acetone until no residue from the adhesive was observed. Samples were then placed on a sample stage with a window to allow for transmission of infrared light.

Micro-Fourier transform infrared spectroscopy (FTIR) was used to determine the relative contribution of molecular water (H_2O_{mol}) and silanol groups (H_2O_{SiOH}) to the total water content of the sinter. Spectra were obtained on a Thermo Nicolet Nexus 470 FTIR spectrometer with a Continuμm microscope accessory in transmission mode using a Tungsten Halogen Near-IR (white light) source, a KBr beamsplitter and MCT-A detector. Each spectrum was obtained with 4 cm^{-1} resolution and 200 scans with an analytical area of 150 × 150 μm from 6500-2000 cm^{-1}. The entire system was continuously purged with dry air. A background spectrum was analyzed for each session and was automatically subtracted by the OMNIC program used for analysis. Locations in each laminae were chosen to maximize IR signal. This was monitored by ensuring that the interferogram had an intensity greater than approximately 0.5 Volts.

The absorption spectra of opal-A and opal-CT show three bands (~3400, 4500 and 5200 cm^{-1}) that represent different forms of water (Fig. 2.5). The band assignments follow studies summarized by Aines and Rossman (1984). The broad band at 3400 cm^{-1}, with a shoulder at ~3700 cm^{-1}, is due to fundamental OH-stretching vibrations of molecular water (H_2O_{mol}) and silanol groups (H_2O_{SiOH}). When the total water content of a mineral is higher than ~2 wt % (Fig. 2.5), the absorbance of this band is difficult to

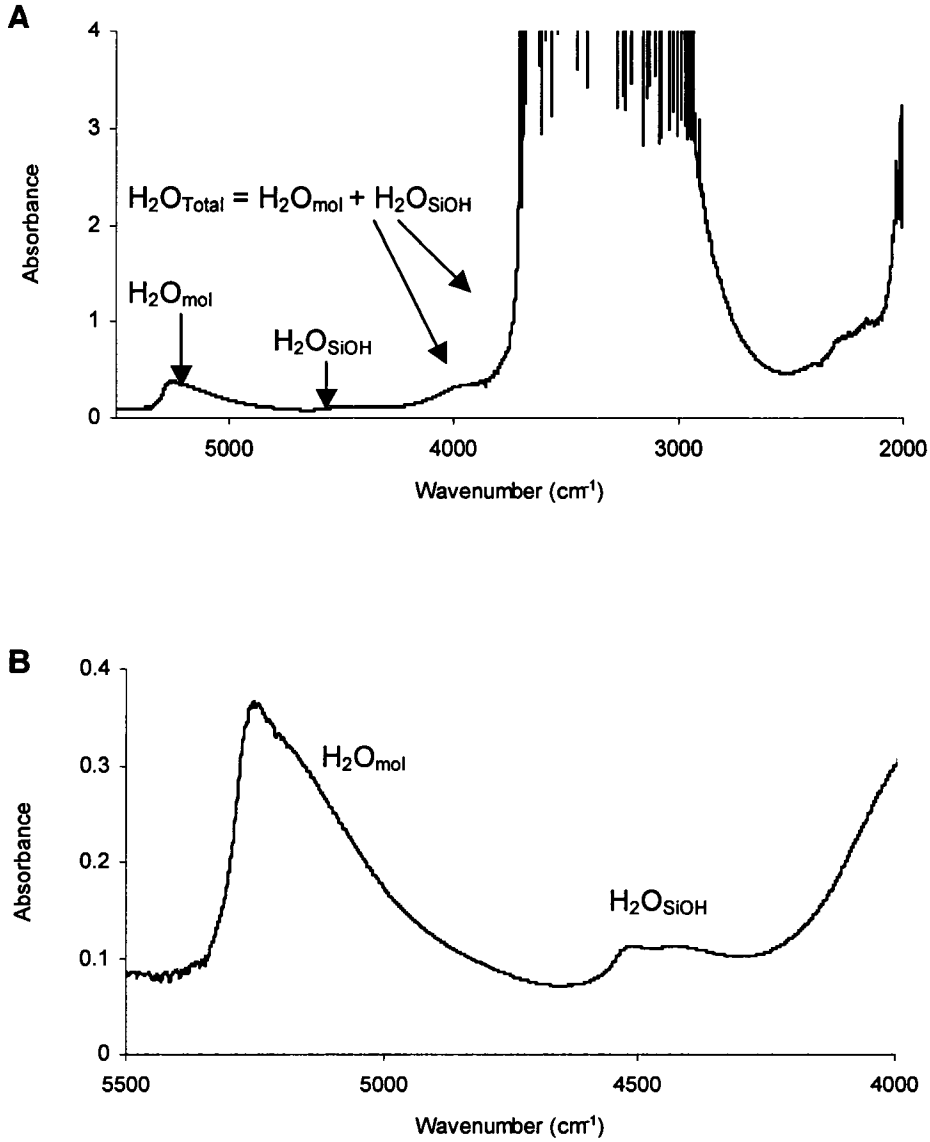

Figure 2.5. A) Representative of FTIR spectrum of opal-A showing water species. Band assignments follow those summarized by Aines and Rossman (1984). **B)** Expanded view of the H_2O_{mol} (5200 cm^{-1}) and H_2O_{SiOH} (4500 cm^{-1}) bands in the near infrared portion of the spectrum. The absorbance is a unitless measurement.

keep on scale (Rossman 1988; Danyushevsky et al. 1993; Graetsch 1994). Also, the linearity of Lambert-Beer's law, used for the quantitative determination of molecular species in a sample, breaks down when the maximum peak height is greater than 1 absorbance unit (Smith 1996). Bands in the near infrared (NIR) portion of the spectrum (4500 and 5200 cm^{-1}) are better suited for water content determination of water-rich specimens because the absorbance in this region is significantly less intense than the 3400 cm^{-1} band. The absorption bands of H_2O_{SiOH} and H_2O_{mol} do not overlap in the NIR (Fig. 2.5) allowing for reliable quantitative determination of water contents (Newman et al. 1986).

The concentrations of H_2O_{SiOH} and H_2O_{mol} were calculated using the Lambert-Beer law:

$$\overline{A} = \varepsilon_{\upsilon}^{*} \cdot c \cdot d$$

$\bar{A}$ (unitless) = Integral absorbance

$\varepsilon^{*}_{\upsilon}$ ($l.mol^{-1}cm^{-1}$) = intergrated extinction coefficient for the band

c ($mol.l^{-1}$) = molar concentration

d (cm) = sample thickness

Although the Lambert-Beer law is applicable to the maximum peak height in absorbance units, it has been shown that $\bar{A}$ is a more reliable measure of determining water concentrations (Langer and Flörke 1974; Paterson 1982). The integral absorbance for each spectrum was determined using PeakFit ©, a peak fitting software program produced by Systat Software Inc. Integrated extinction coefficients (5200 cm^{-1} band, H_2O_{mol}: $\varepsilon^{*}_{\upsilon} = 250\ l.mol^{-1}cm^{-1}$; 4500 cm^{-1} band, H_2O_{SiOH}: $\varepsilon^{*}_{\upsilon} = 160\ l.mol^{-1}cm^{-1}$), originally

given by Scholze and Franz (1960), were used in this study as in previous studies (Langer and Flörke 1974; Graetsch et al. 1985, 1990; Rossman 1988; Flörke et al. 1990). Sample thicknesses were measured using a Mitutoyo micrometer with a manufacturer's error of ± 0.001 mm. For the determination of water content (wt %) in opal, a density of 2.2 $kg.l^{-1}$ was used in this study as in previous studies (Langer and Flörke 1974; Fröhlich 1989; Graetsch et al. 1990). Lambert-Beer's law was validated in this study for the 5200 and 4500 cm^{-1} bands; illustrated by the linear relationship obtained between the integral absorbance (Ā) and sample thickness (d) of a given type of sinter (Fig. 2.6). For water species in hydrated siliceous minerals, it is assumed that $C_{H2O} = C_{5200} + C_{4500}$, where C_{H2O} is the concentration of total water, C_{5200} and C_{4500} are the concentrations of H_2O_{mol} and H_2O_{SiOH}, respectively (Langer and Flörke 1974; Graetsch et al. 1985; Newman et al. 1986; King et al. 2002).

The molecular water band (5200 cm^{-1}) may be split into high energy and low energy bands (Langer and Flörke 1974). Langer and Flörke (1974) used two Gaussian component bands in their analyses of the molecular water band (5200 cm^{-1}). The high energy band represents "type A molecular water", which is isolated in the SiO_2 matrix and not involved with hydrogen bonding. The low energy band represents "type B molecular water", which is adsorbed water that resides in relatively large voids with strong hydrogen bonds (Langer and Flörke 1974; Aines and Rossman 1984; Flörke et al. 1991). The component bands within the 4500 cm^{-1} band are related to the strength of hydrogen bonds in silanol groups (Langer and Flörke 1974; Flörke et al. 1991). The stronger the hydrogen bonds are in the silanol groups, the lower the energy of the combination band (Langer and Flörke 1974). In their analyses of silanol groups, Langer

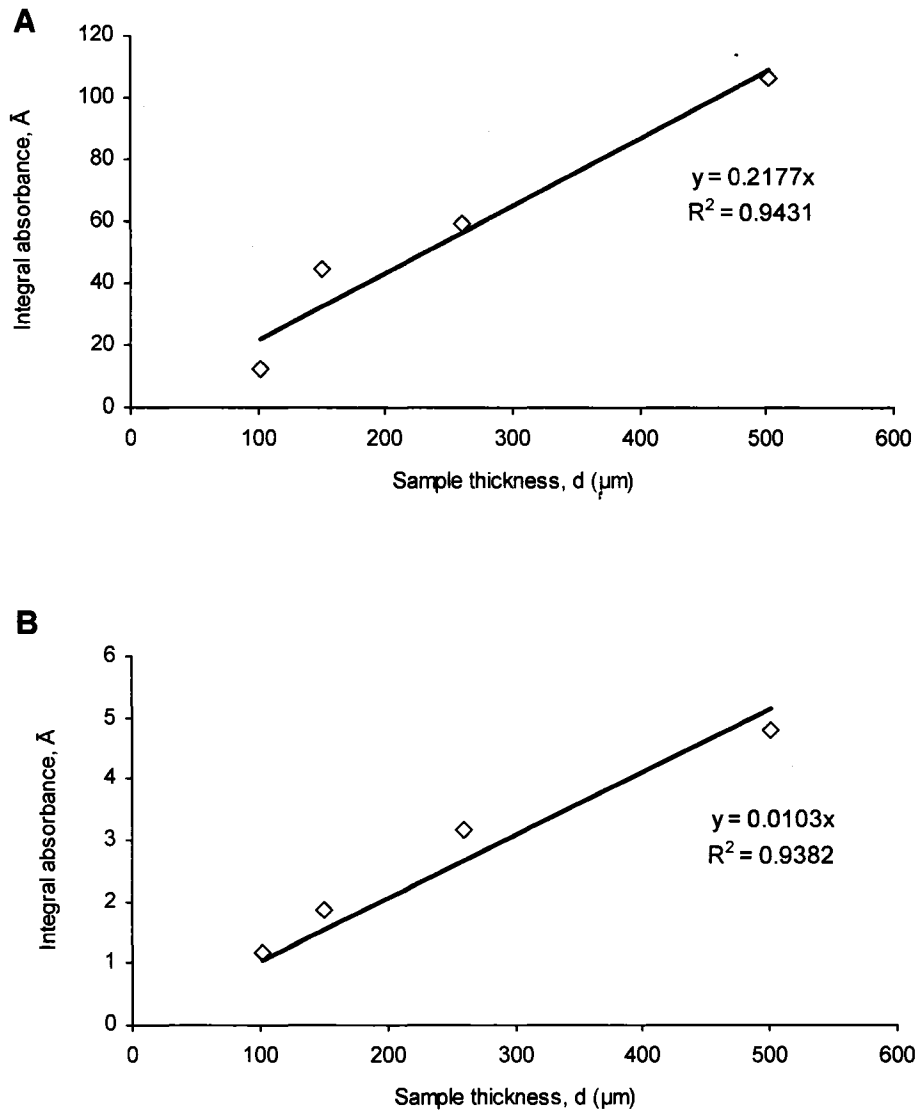

Figure 2.6. A) Integral absorbance of the H_2O_{mol} (5200 cm^{-1}) band as a function of sample thickness. **B)** Integral absorbance of the H_2O_{SiOH} (4500 cm^{-1}) band as a function of sample thickness. A linear relation proves the validity of Lambert-Beer's law.

and Flörke (1974) used two Gaussian component bands; "type A silanol groups" (high energy band) are located at structural defects in the silica matrix whereas "type B silanol groups" (low energy band) are located on silica surfaces with strong involvement in hydrogen bonding. The spectra obtained by the summation of component bands acquired in the PeakFit © program were closest to the measured spectra in this study (as determined by R^2 closest to 1) using a combination of four Gaussian-Lorentzian component bands to fit the 5200 cm^{-1} band and three Gaussian-Lorentzian component bands to fit the 4500 cm^{-1} band; as opposed to the two Gaussian component bands, in both the 5200 and 4500 cm^{-1} bands, used by Langer and Flörke (1974) (Figs. 2.7, 2.8). Relative comparisons of the different types of molecular water and silanol groups (type A vs. type B) in opal have been undertaken through comparisons of the percent area of component bands (Langer and Flörke 1974). Component bands 1 and 4 in the 5200 cm^{-1} band (Fig. 2.7), used in this study, are assumed to be equivalent to the high and low energy bands, respectively, as described by Langer and Flörke (1974). The sum of component bands 1 and 2 in the 4500 cm^{-1} band (Fig. 2.8) used in this study are assumed to be equivalent to the high energy band, and component band 3 in the 4500 cm^{-1} band (Fig. 2.8) is assumed to be equivalent to the low energy band described by Langer and Flörke (1974).

An attempt was made to obtain 3 spectra for each type of sinter in a given sample, so that a representative average of the water content could be obtained. Complications arose because not all types of sinter are able to transmit sufficient light to obtain a good spectrum, as determined by absorbance levels (Fig. 2.5 vs. 2.9). To minimize error, only spectra with a maximum peak height of less than 1 absorbance unit were used

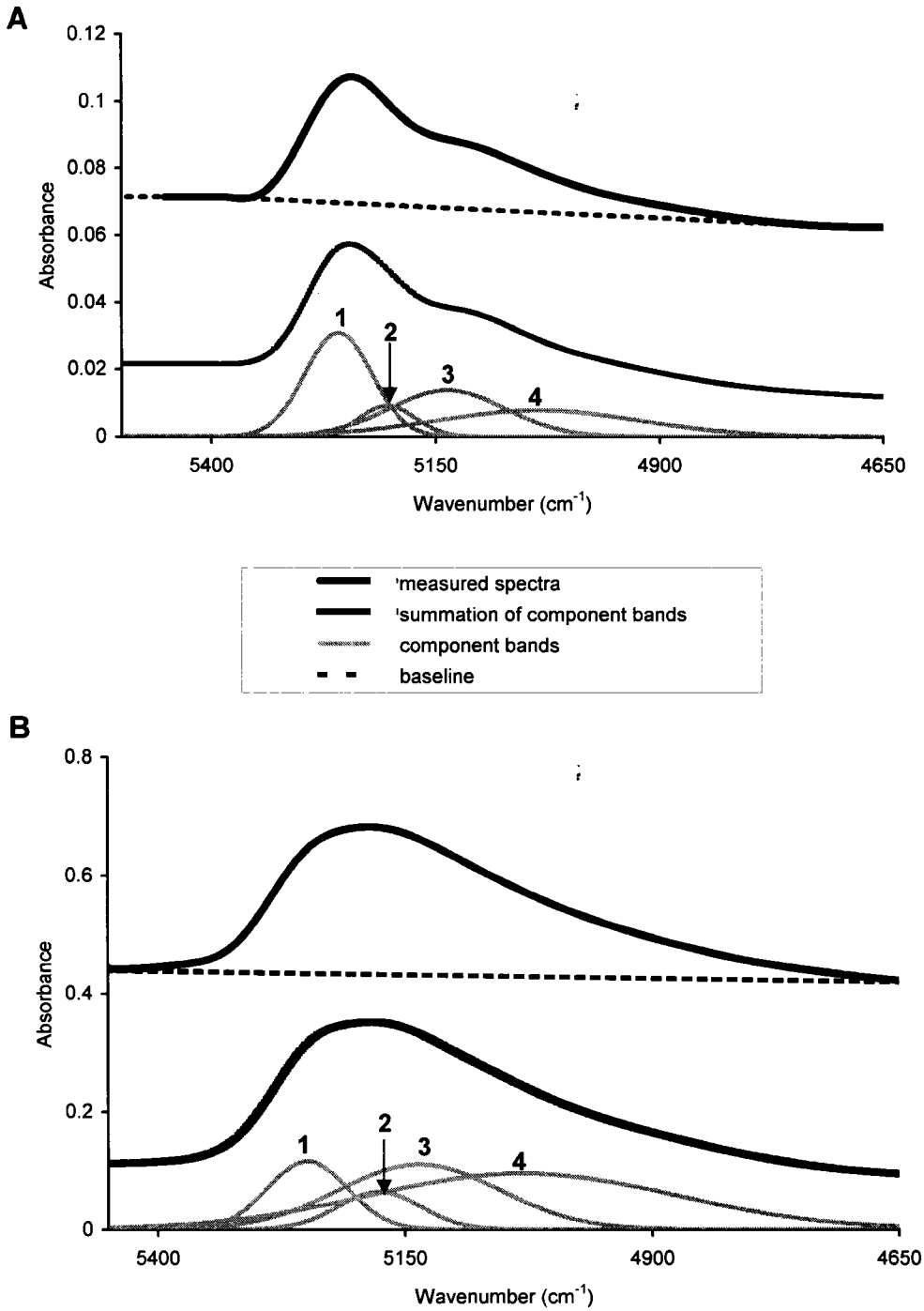

Figure 2.7. Representative FTIR spectra of opal. Component bands (1-4) assigned using the PeakFit program. Component band 1 represents type A molecular water and component band 4 represents type B molecular water. Summation of component bands has R^2 greater than 0.999. A) Representative FTIR spectrum of molecular water band of opal-A (NZ 592, vitreous sinter). B) Representative FTIR spectrum of molecular water band of opal-CT (NZ 816, vitreous sinter). The absorbance is a unitless measurement.

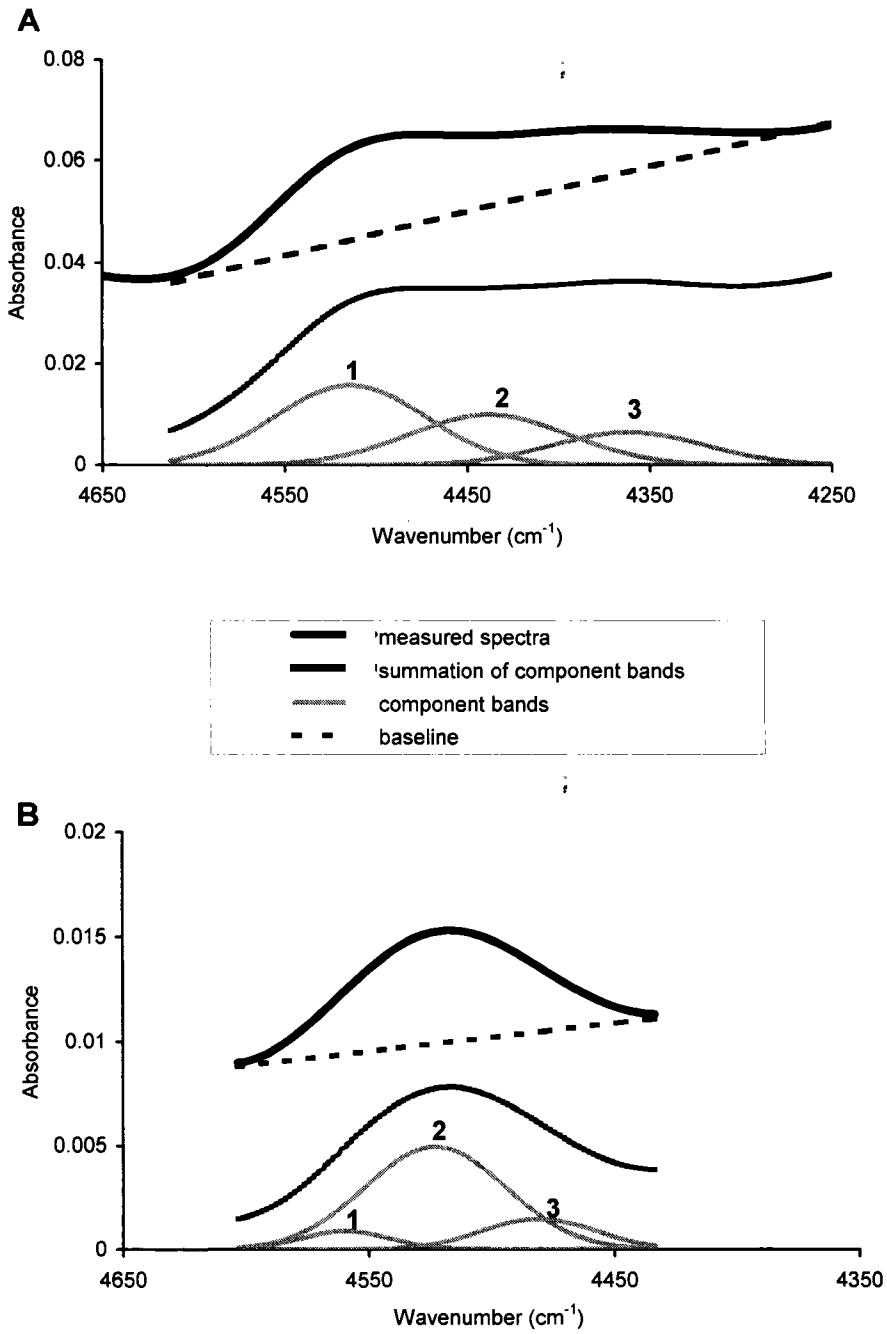

Figure 2.8. Representative FTIR spectra of opal. Component bands (1-3) assigned using the PeakFit program. Component bands 1 and 2 represent type A silanol groups and component band 3 represents type B silanol groups. Summation of component bands has R^2 greater than 0.999. A) Representative FTIR spectrum of silanol band of opal-A (NZ 592, vitreous sinter). B) Representative FTIR spectrum of silanol band of opal-CT (NZ 816, vitreous sinter). The absorbance is a unitless measurement.

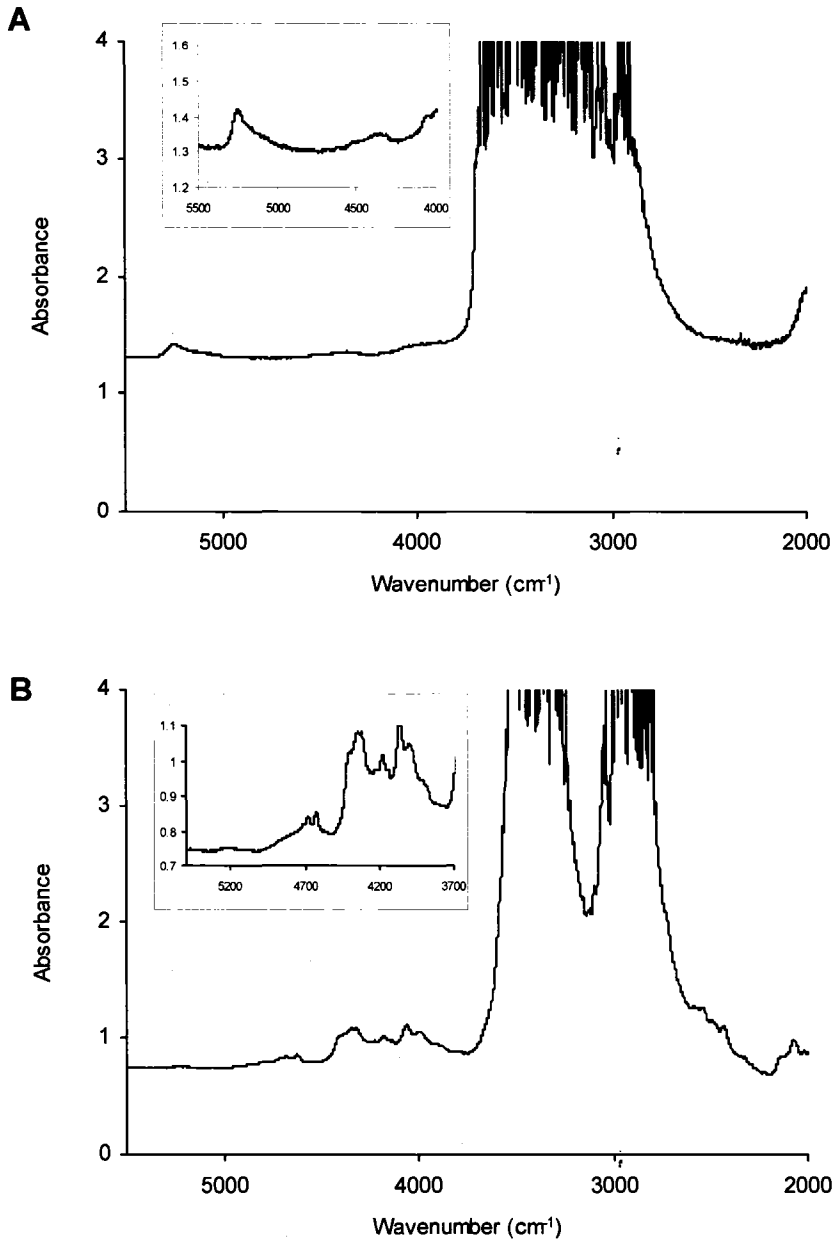

Figure 2.9. A) Sample FTIR spectra illustrating poor transmission of IR light. Absorbance levels above 1 may not used successfully in Lambert-Beer's law. Inset is a close up of NIR portion of the spectrum. **B)** Sample FTIR spectra of sinter and adhesive. Inset is a close up of NIR portion of the spectrum. The absorption region of the adhesive overlaps with absorption region of water, thus inhibiting the determination of water in sinter. The absorbance is a unitless measurement.

(King et al. 2004). Porous friable sinter generally transmits light poorly due to its opaque nature, whereas vitreous sinters readily transmit light because they are generally translucent. Light transmission may be improved by using thinner samples, however, thinner sinter samples (< 250 μm) tended to break apart when separating them from the glass thin section. As a result, the spatial position of the sinter in the sample is lost. Successfully removing the adhesive used to bind the sample to the thin section glass while keeping the sinter intact was another point of difficulty with certain types of sinter. Due to their porous and poorly consolidated nature, porous friable sinter presented the most difficulty in removing the adhesive. Spectra with signs of adhesive were not used in calculating water contents because of overlap with the region of water absorption (4500 and 5200 cm^{-1}) (Fig. 2.9B). Due to these challenges, spectra were not obtained for all types of sinter. Where more than one spectrum was successfully obtained for a given sinter type, an average spectrum was calculated and used to determine the water content.

Multiple measurements using FTIR analyses could not be obtained for each type of sinter, as in EMP analyses; thus, determining the appropriate error for each lamina was not possible. Conservative error estimates ($H_2O_{mol} \pm 0.5$ wt %, $H_2O_{SiOH} \pm 0.1$ wt %, $H_2O_{Total} \pm 0.7$ wt %) are applied here based on the manufacture's error for thickness measurements and *e* determined in the validation of Lambert-Beer's law using error propagation methods. The extinction coefficient used in Lamber-Beer's law also carries a degree of error; however, it has not been published and could not be used in the error estimated here.

Chapter Three – Results

3.1 Mineralogy and Morphology Results

3.1.1 Waikite Geyser Complex, New Zealand

Based on XRD analyses, the sinter samples chosen for analysis from the Waikite Geyser complex are composed entirely of opal-A. Each sample, however, is formed of several different types of sinter (Figs. 3.1A, 3.3A, 3.5). Thin section analyses indicate that sinter with a vitreous luster generally appears translucent to clear in plane polarized light, whereas sinter with a dull luster appears opaque (Figs. 3.1B, 3.3B). At high magnification under plane polarized light, patchy vitreous sinter displays spherical aggregations of non-crystalline silica (Fig. 3.3C).

Spheres, 500 nm to 5 μm in diameter, are common throughout the sinter from the Waikite Geyser complex (Figs. 3.2B, 3.4E, 3.6E). Silicified microbes are found mainly in the porous friable sinter and porous indurated sinter, however, many of the microstructures found in the different types of sinter from the Waikite Geyser complex vary both between samples and within one sample.

NZ 592

Collected from the second terrace below the Waikite Vent, this sinter sample is located closest to the main vent (Fig. 1.1D). It is formed of alternating laminae of porous indurated, dull indurated, vitreous and patchy vitreous sinter (Fig. 3.1). Porous indurated sinter is found surrounding spicules (Fig. 3.1A). Spicules, which are internally laminated elongate structures generally with a rounded end, are commonly formed near geyser vents (Walter 1976; Cady and Farmer 1996; Braustein and Lowe, 2001; Jones and Renaut

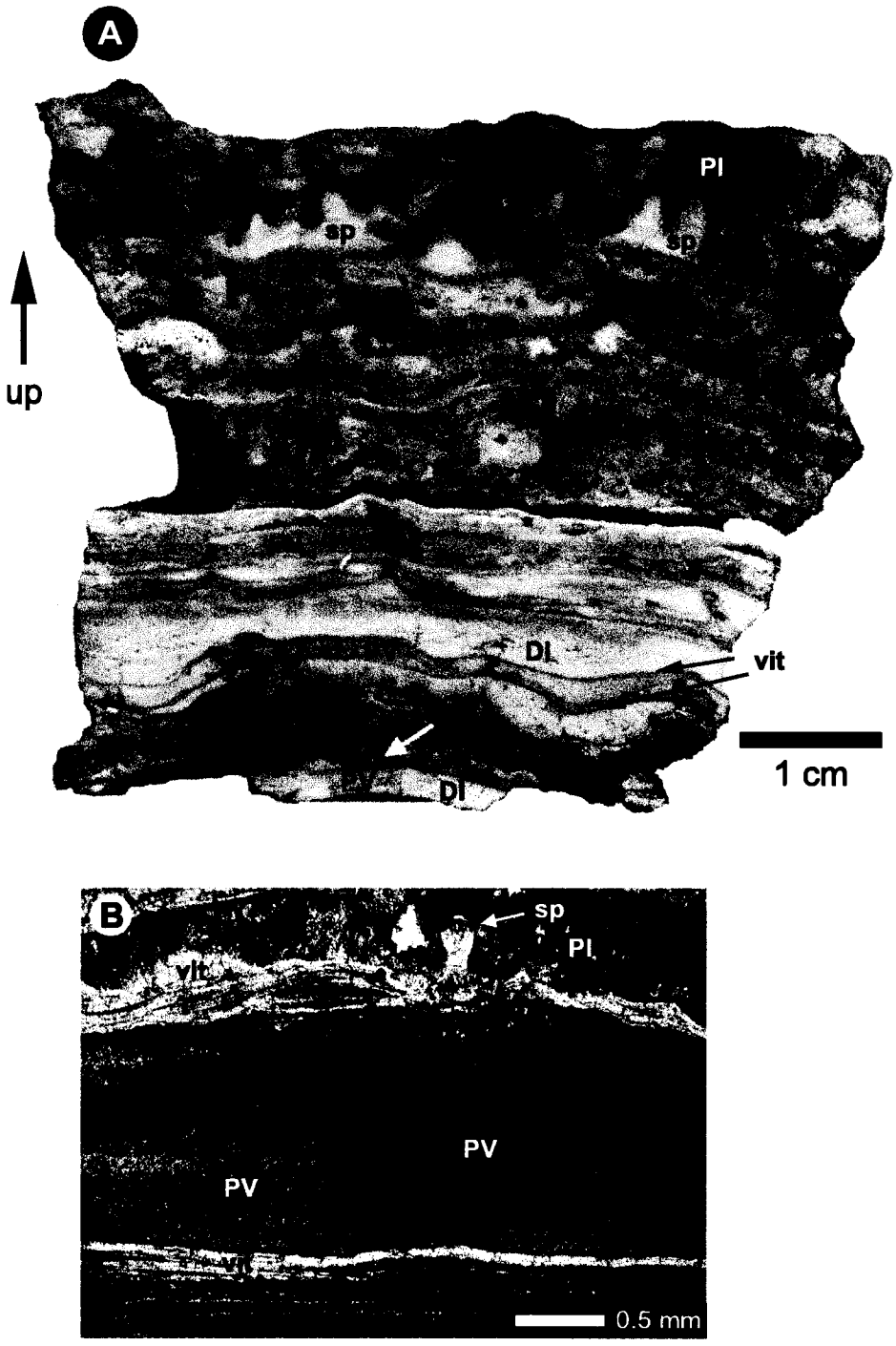

Figure 3.1. Sample NZ 592 from the Waikite Geyser complex, proximal to the main vent. **A)** Hand sample illustrating different types of sinter; patchy vitreous (PV), porous indurated (PI), dull indurated (DI) and vitreous sinter (vit), and spicules (sp) composed of vitreous sinter. White arrow indicates spicule highlighted in photomicrograph in Fig. 3.1B. **B)** Photomicrograph illustrating different types of sinter.

2003a; Lowe and Braunstein 2003). In this sample, spicules, 500 nm to 5 mm high, are composed of vitreous sinter (Fig. 3.1A).

More void spaces between spheres are present in the dull indurated and patchy vitreous sinter than in the vitreous sinter (Fig. 3.2A). The slightly porous dull indurated sinter in this sample is formed largely of silicified microbes (Fig. 3.2C). Connection pads occur between spheres in the patchy vitreous sinter (Fig. 3.2B).

The porous indurated sinter contains spheres and silicified microbes. Other notable features in this type of sinter include distinct gaps between spheres and the surrounding opal cement (Fig. 3.2D). Ringed necks are also found in the porous indurated sinter (Fig. 3.2E). Although not widespread in this sample, the ringed necks further illustrate the variety of sinter microstructures. More common in the porous indurated sinter are multilobed masses of spheres covered in nanospheres (Fig. 3.2F).

NZ 603

Sample NZ 603, collected between the vents of Waikite and Pareia (Fig. 1.1D), is composed of alternating layers of patchy vitreous sinter and porous friable sinter (Fig. 3.3). On the microscale level, the patchy vitreous sinter appears more porous than the porous friable sinter (Fig. 3.4A). The porous friable sinter is formed of multilobed masses of spheres, 3-10 μm in diameter (Fig. 3.4B, C), whereas the patchy vitreous sinter generally displays a scalloped surface (Fig. 3.4B, D). In a transition area between the patchy vitreous sinter and porous friable sinter, connection pads are visible and necks connect adjacent spheres (Fig. 3.4B, E, F).

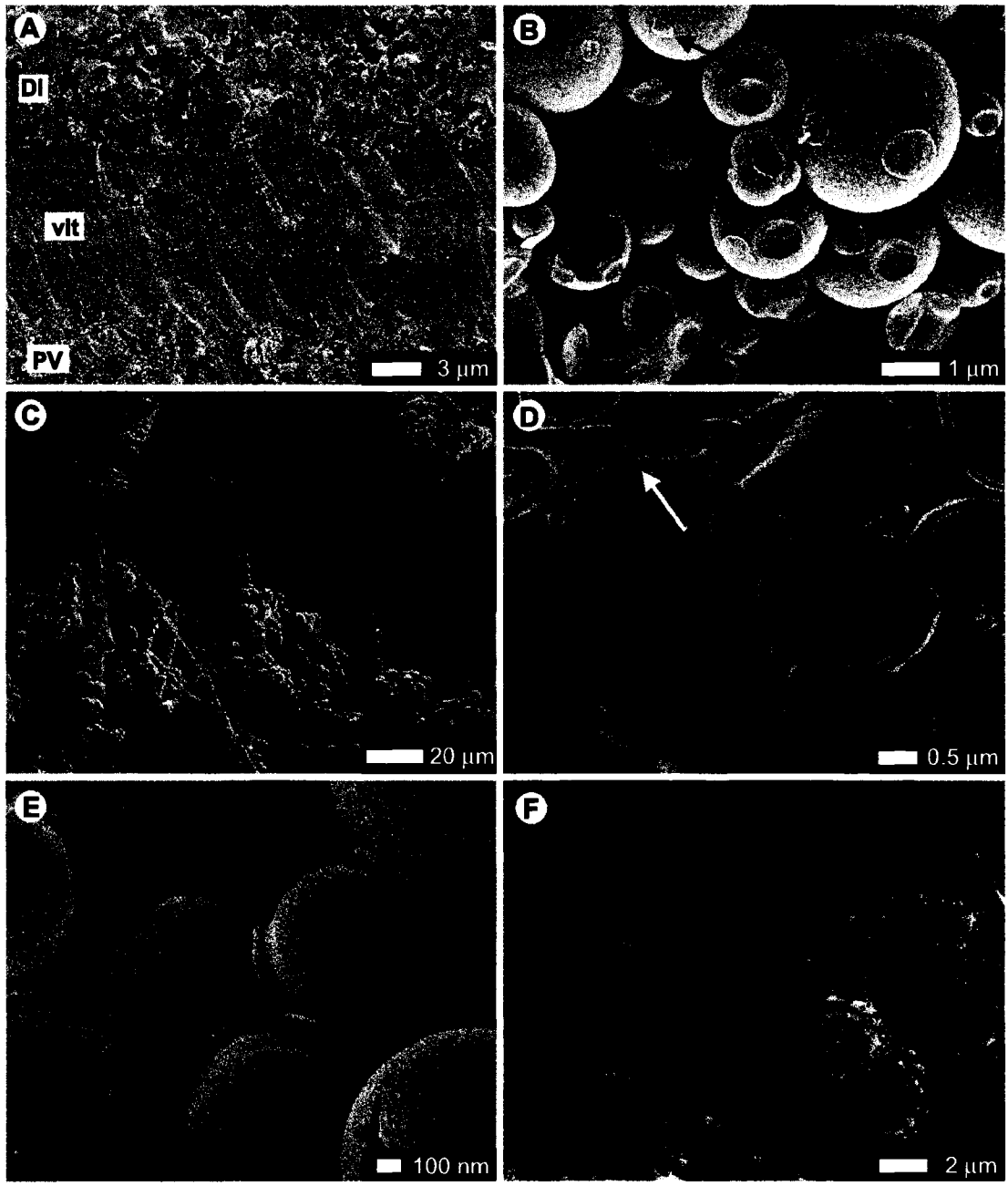

Figure 3.2. Sample NZ 592 from the Waikite Geyser complex. **A)** Variable void spaces in different types of sinter; dull indurated (DI), vitreous (vit), and patchy vitreous sinter (PV). **B)** Spheres with connection pads, indicated with arrows, in PV sinter. **C)** Silicified microbes in DI sinter. **D)** Gaps between cement and spheres, indicated with arrow, in porous indurated (PI) sinter. **E)** Ringed necks in PI sinter. **F)** Nanospheres covering mulilobed masses of spheres in PI sinter.

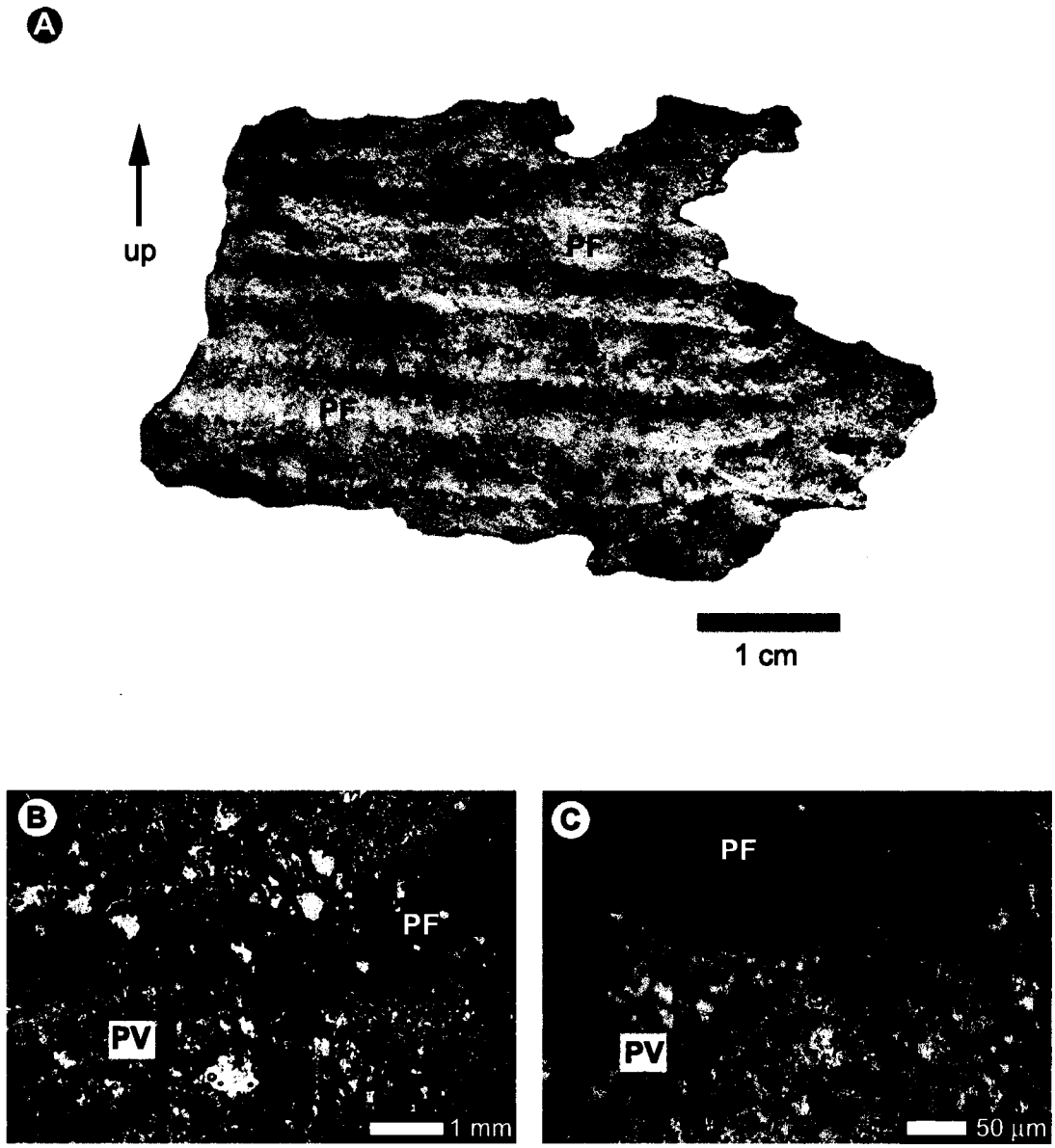

Figure 3.3. Sample NZ 603 from the Waikite Geyser complex, between the Waikite and Pareia vents. **A)** Hand sample illustrating different types of sinter; porous friable (PF) and patchy vitreous (PV). **B)** Photomicrograph of PF and PV sinter. PF sinter appears opaque and PV sinter appears translucent. **C)** Close up photomicrograph of PF and PV sinter illustrating spherical nature of opal-A.

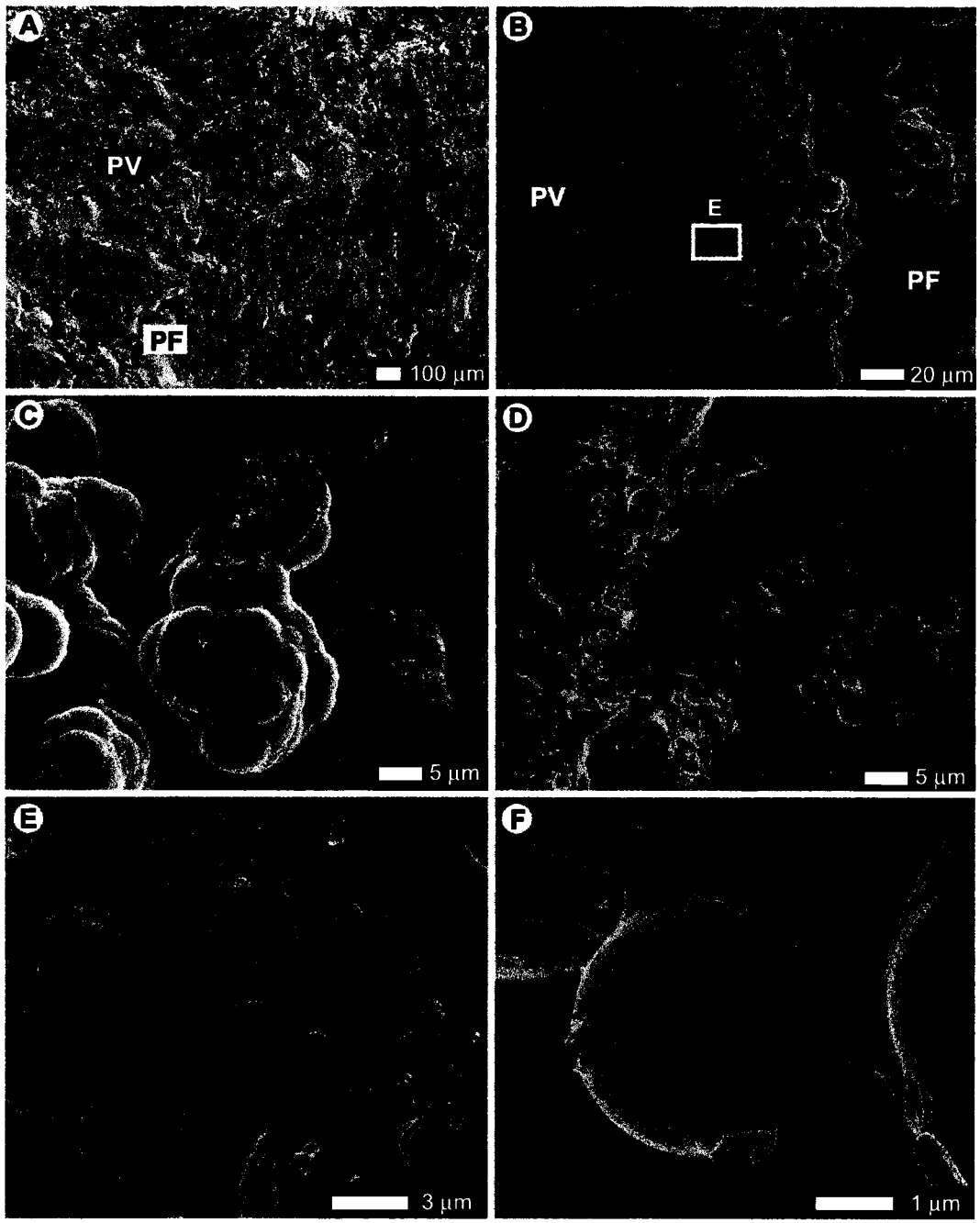

Figure 3.4. Sample NZ 603 from the Waikite Geyser complex, between the Waikite and Pareia vents. **A)** Overview of porous friable (PF) and patchy vitreous (PV) sinter, illustrating relatively porous nature of PV sinter compared to PF sinter. **B)** Boundary between PF and PV sinter. Box E, enlarged in Fig. 3.4E. **C)** Multilobed masses of spheres in PF sinter. **D)** Scalloped surfaces in PV sinter. **E)** Close up of boundary bewteen PF and PV sinter, illustrating spheres connected with necks and connection pads. **F)** Close up of sphere with connection pads and necks.

NZ 601

This sample, the most distal from the vent (Fig. 1.1D), is composed mainly of densely laminated white and grey vitreous sinter with areas of porous indurated sinter and porous friable sinter (Fig. 3.5). In thin section, the white vitreous sinter is opaque whereas the grey vitreous sinter is translucent (Fig. 3.35).

Spores (Fig. 3.6A), pollen grains (Fig. 3.6B), and spheres with ringed necks are found in the upper portion of the porous indurated sinter. Spheres (~ 500 nm in diameter) with small holes (~ 150 nm in diameter) form parts of the upper porous indurated sinter (Fig. 3.6C, D). Although these spheres with holes are most dominant in the upper part of the porous indurated sinter, they are found in all types of sinter in this sample. The lower portion of the porous indurated sinter (Fig. 3.5) is composed of silicified microbes and spiky spheres (Fig. 3.6E, F). The porous friable sinter is formed largely of silicified microbes and silicified plant material (Fig. 3.7A, B).

Spheres found in the white vitreous sinter are 0.5 to 2 μm in diameter and have elongated necks between them (Fig. 3.7C, D). The spheres in the grey vitreous sinter are generally larger, 1 to 5 μm in diameter, with smaller spheres commonly located in the pores between the larger spheres (Fig. 3.7E, F). These small spheres are connected with elongated necks, whereas connection pads are evident on the larger spheres.

3.1.2 Geyser Flat, New Zealand

XRD analysis indicates that the sample from Geyser Flat (NZ 816) is composed of opal-CT and quartz. Alternating flat-lying laminae of vitreous and dull indurated sinter form the lower part of the sample, whereas dull indurated and patchy vitreous

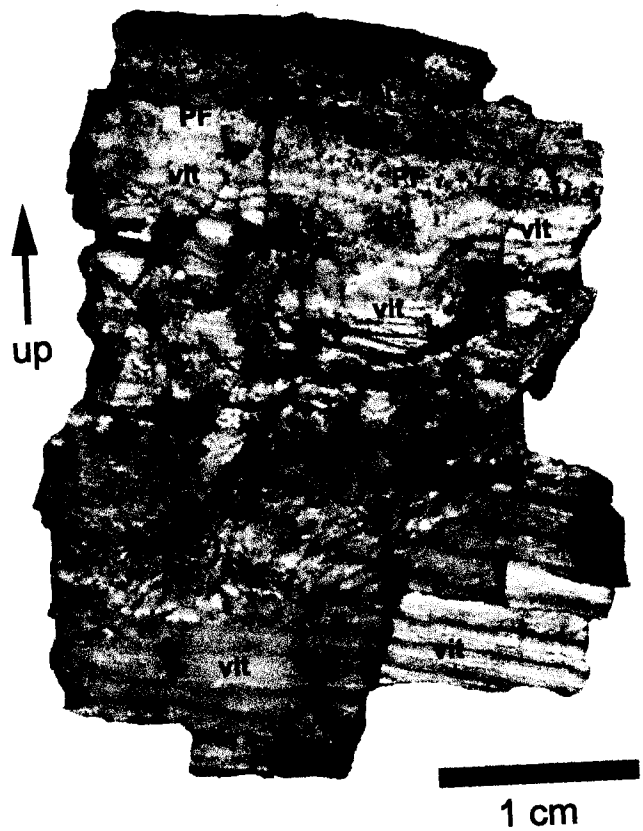

Figure 3.5. Hand sample of NZ 601 from the Waikite Geyser complex on the distal discharge apron. Different types of sinter; porous friable (PF), porous indurated (PI) and vitreous sinter (vit).

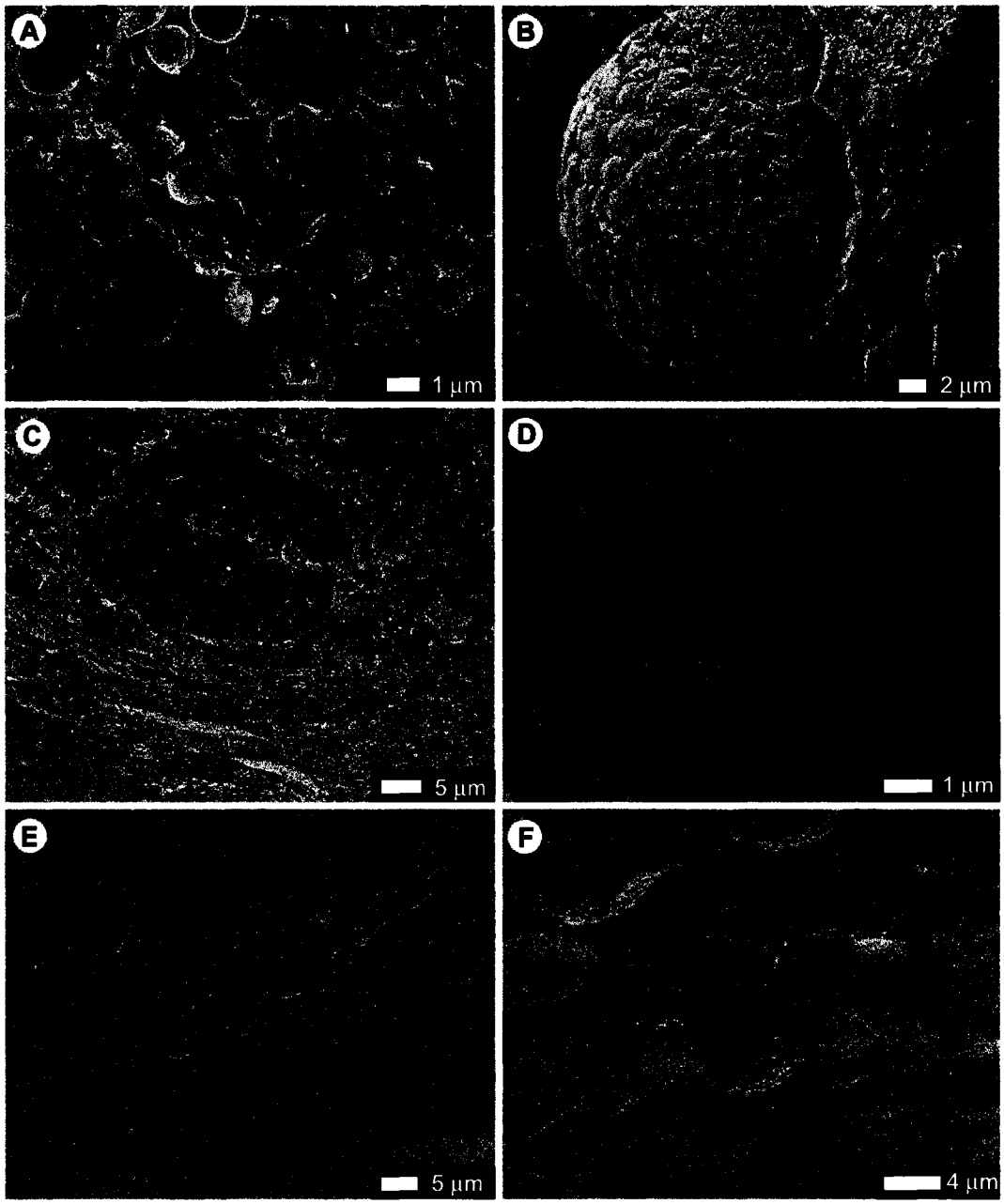

Figure 3.6. Sample NZ 601 from the Wakite Geyser complex on the distal discharge apron. **A)** Spores in porous indurated (PI) sinter. **B)** Pollen grain in PI sinter. **C)** Cluster of spheres surrounded by spheres with holes in PI sinter. **D)** Close up of spheres with holes. **E)** Spiky spheres in PI sinter. **F)** Close up of spiky spheres.

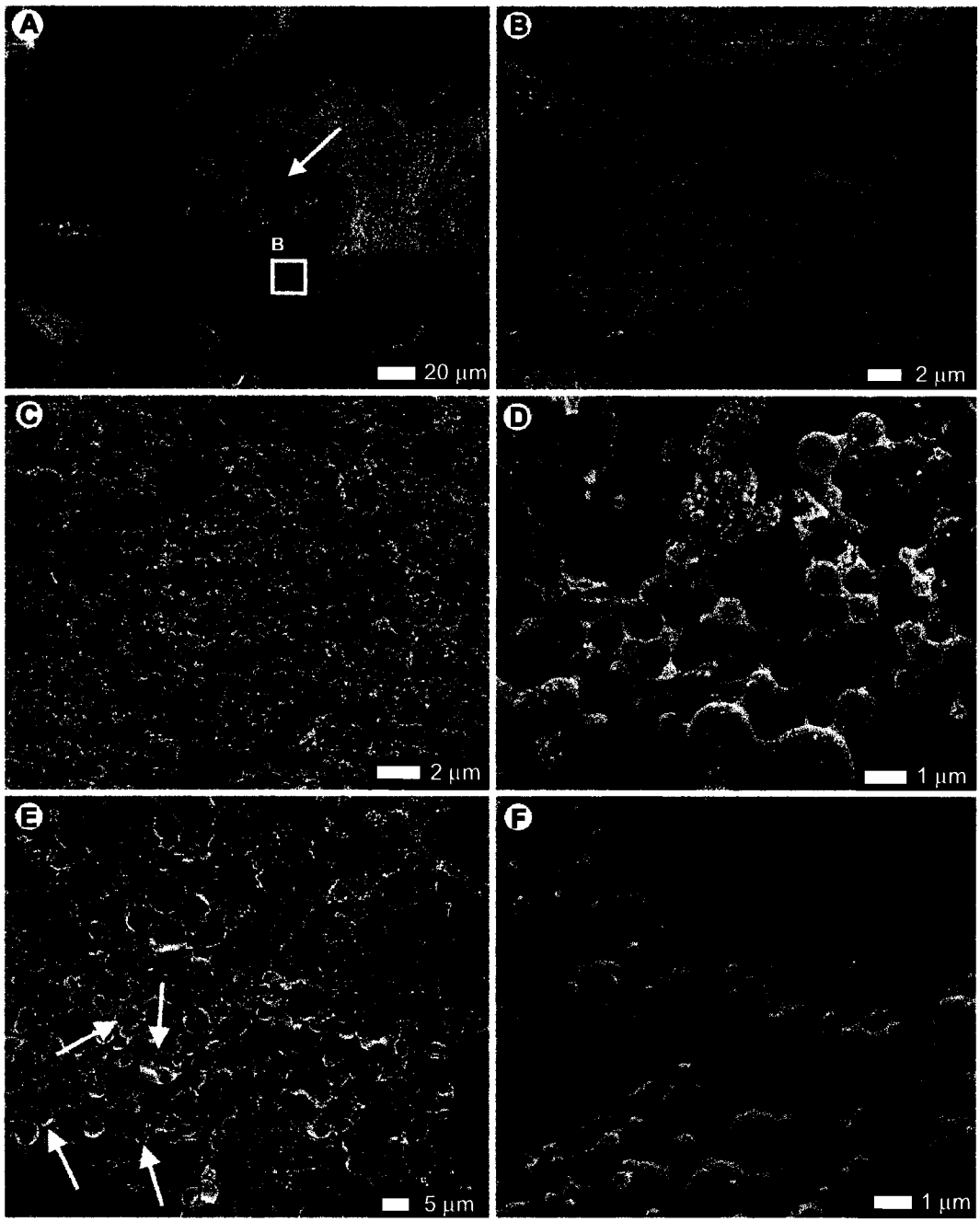

Figure 3.7. Sample NZ 601 from the Waikite Geyser complex on the distal discharge apron. **A)** Arrows indicate silicified microbes in large cavities in porous friable (PF) sinter. Box with letter B indicates location of Fig. 3.7B. **B)** Silicified plant material (?) **C)** Spheres in white vitreous sinter. **D)** Close up of spheres in white vitreous sinter, illustrating elongated necks between spheres. **E)** Spheres in grey vitreous sinter with connection pads (arrows). **F)** Close up of spheres in grey vitreous sinter, illustrating necks and connection pads.

sinter form the upper part (Fig. 3.8). These two parts are separated by a thin layer (0.5 cm) of porous indurated sinter. Large cavities in this sample are lined with a thin (< 100 μm) coating of transparent vitreous sinter (Fig. 3.8B). Detrital quartz grains (~ 10-20 μm) are evident in the vitreous sinter (Fig. 3.8B).

Lepispheres are common throughout most types of sinter in the Geyser Flat sample; however, numerous other microstructures are equally abundant. The vitreous sinter is composed mainly of lepispheres (Fig. 3.9B-D). Intercalated platelets dominate the non-porous areas surrounding cavities containing lepispheres (Fig. 3.9E). Nanospheres are common in the lower vitreous laminae (Fig. 3.9A, F). Angular detrital quartz grains, identified by EDX, are also found in the vitreous sinter (Fig. 3.10B). The transparent vitreous sinter lining the large cavities (Fig. 3.8B) throughout the sample is composed mainly of multilobed masses of spheres with very little void space (Fig. 3.10C, D).

The dull indurated sinter contains lepispheres and knobby lepispheres (Fig. 3.10A). In some areas of the dull indurated sinter, numerous silica divots are found amongst lepispheres (Fig. 3.11D-F).

Silica divots are also found throughout the patchy vitreous sinter. The patchy vitreous sinter additionally contains multilobed masses of bumpy spheres surrounded by platelets (Fig. 3.11A-C). The platelets are arranged in the same intersecting manner as they are in lepispheres. Lepispheres, however, commonly have a solid interior (Fig. 3.9C). A bumpy texture is evident in the spherical depressions in areas where bumpy spheres are removed also (Fig. 3.11C). A distinct gap, ~ 150 nm thick, occurs between the bumpy spheres and the platelets (Fig. 3.11B).

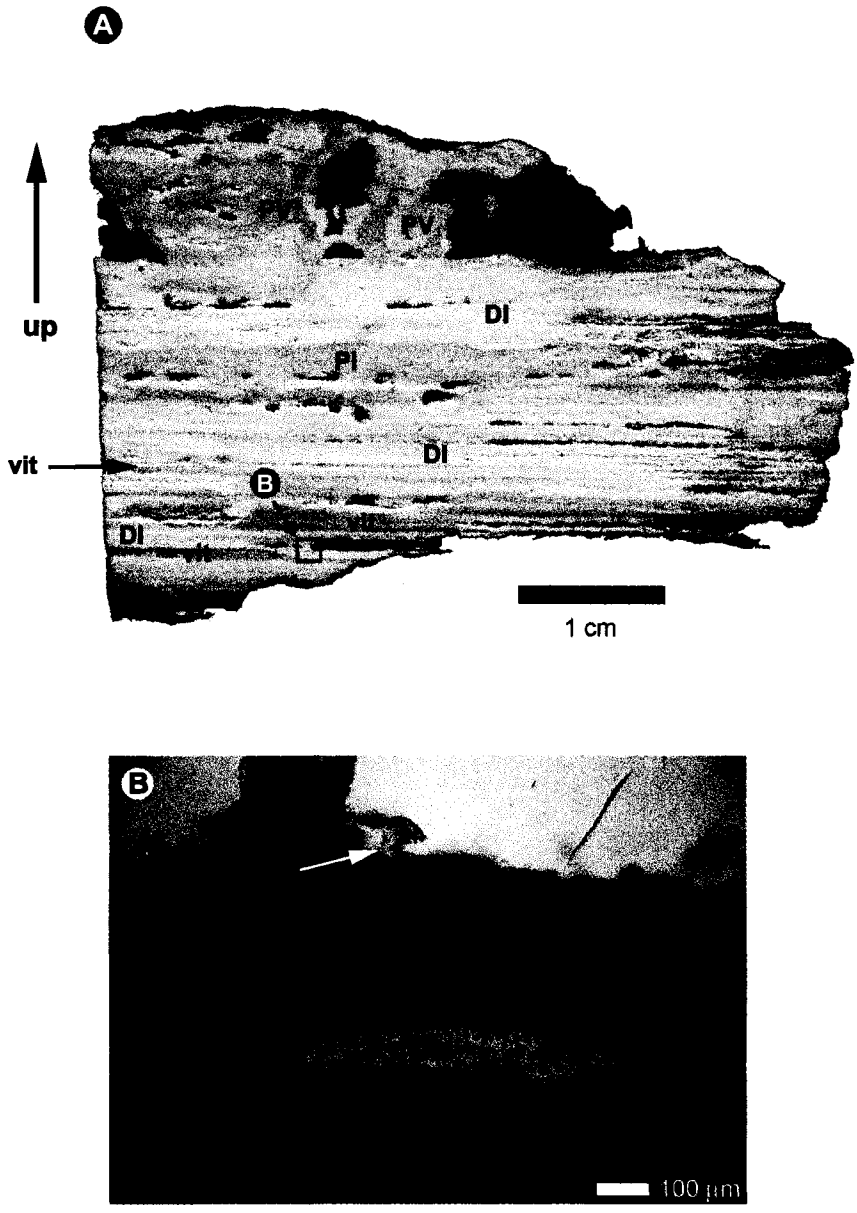

Figure 3.8. Sample NZ 816 from Geyser Flat. **A)** Hand sample illustrating different types of sinter; patchy vitreous (PV), dull indurated (DI), porous indurated (PI) and vitreous (vit) sinter. Box with letter B indicates location of Fig. 3.8B. **B)** Photomicrograph of translucent silica lining large cavities (white arrow) and quartz grains (black arrows) in vitreous sinter.

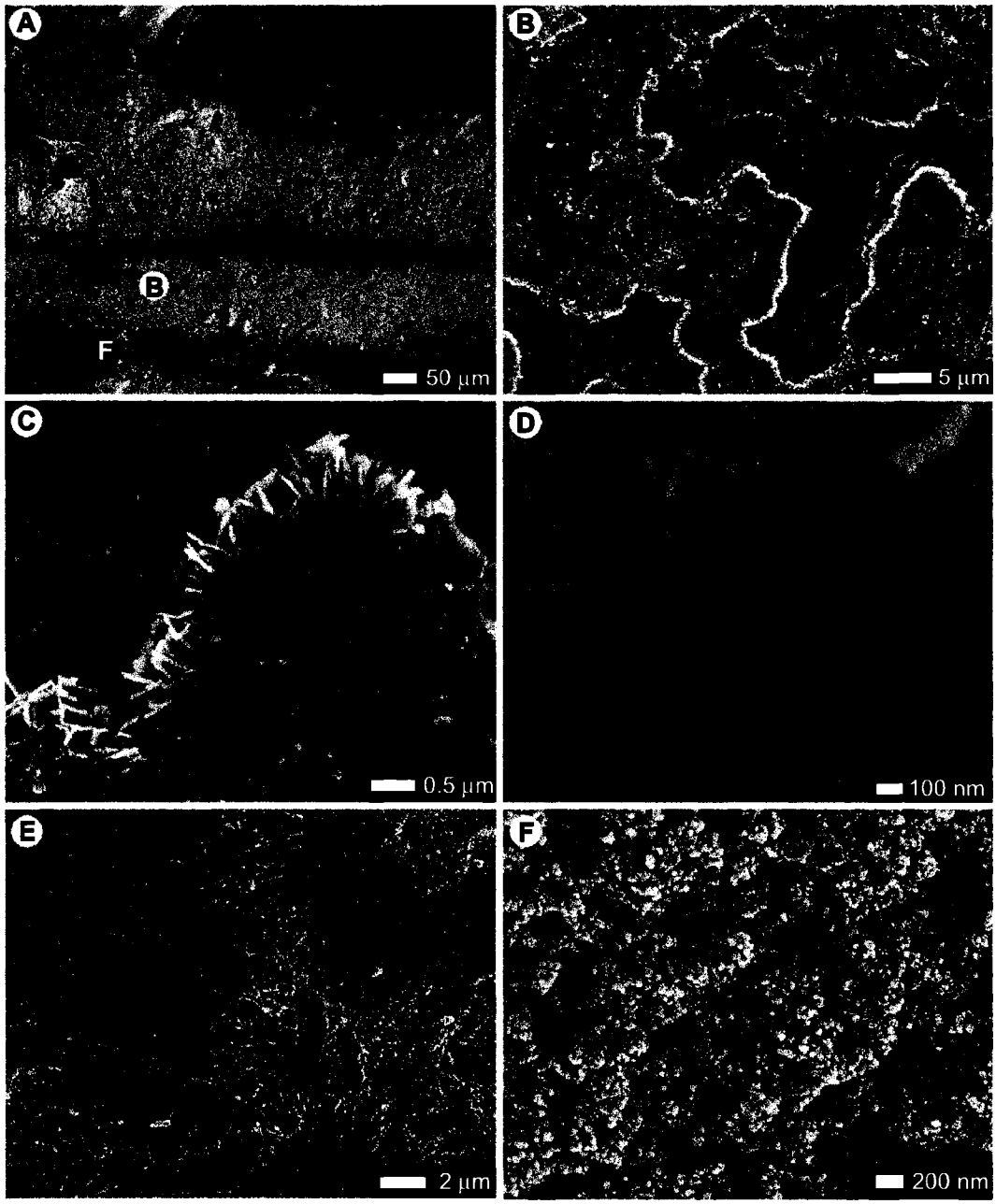

Figure 3.9. Sample NZ 816 from Geyser Flat. **A)** Laminae of vitreous sinter. Letters (B and F) indicate location of Fig. 3.9B and F. **B)** Lepispheres in vitreous sinter. **C)** Cross section of lepispheres in vitreous sinter. **D)** Intersecting platelets of lepispheres. **E)** Intercalated platelets in vitreous sinter. **F)** Nanospheres in vitreous sinter.

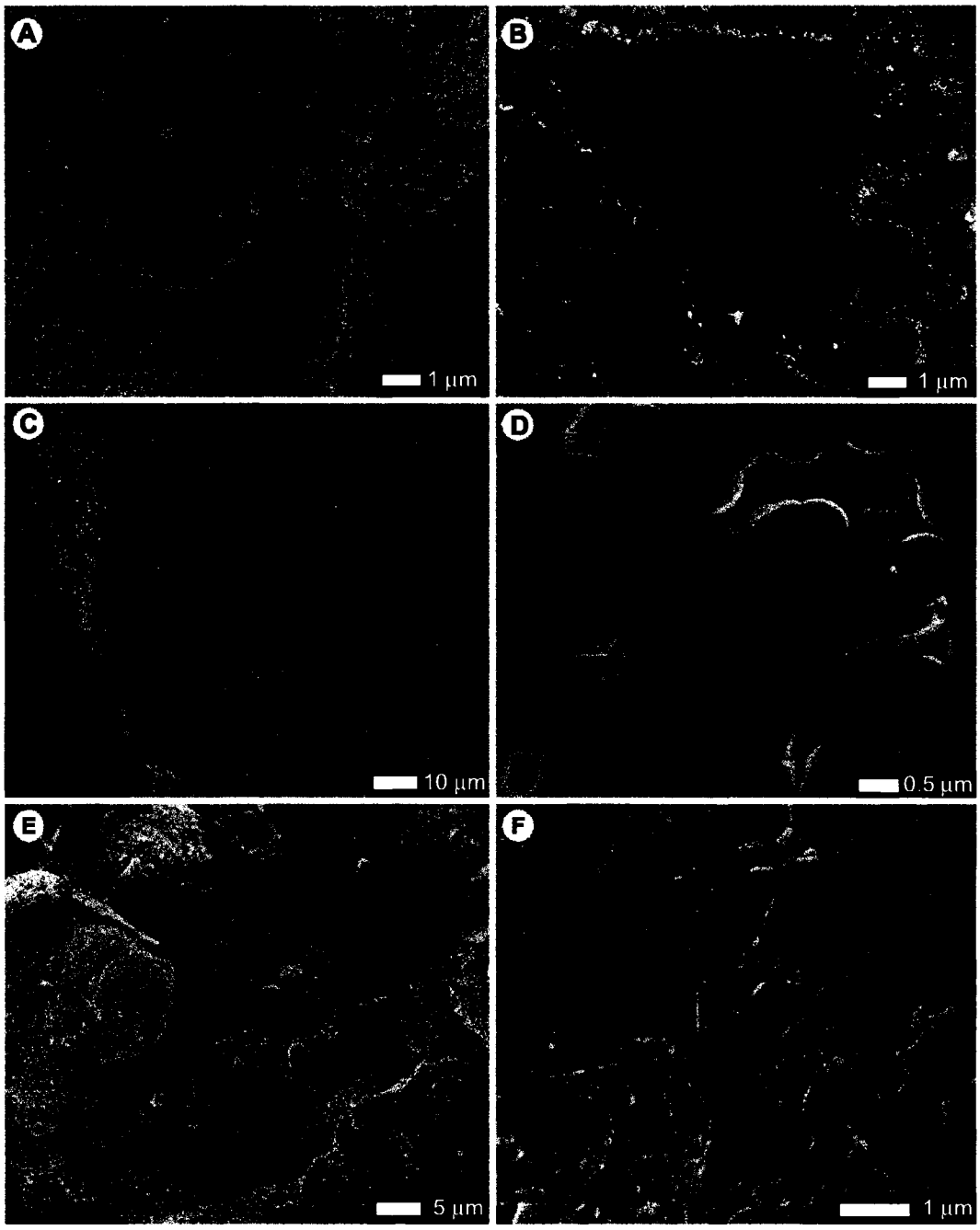

Figure 3.10. Sample NZ 816 from Geyser Flat. **A)** Knobby lepispheres in dull indurated sinter (DI). **B)** Angular quartz grain in vitreous sinter. **C)** SEM photomicrograph of vitreous sinter coating large cavity. **D)** Close up of vitreous sinter coating illustrating multilobed masses of spheres with very little void space. **E)** Mulilobed mass of spheres in amongst coated lepispheres in porous indurated (PI) sinter. **F)** Close up of coated lepispheres.

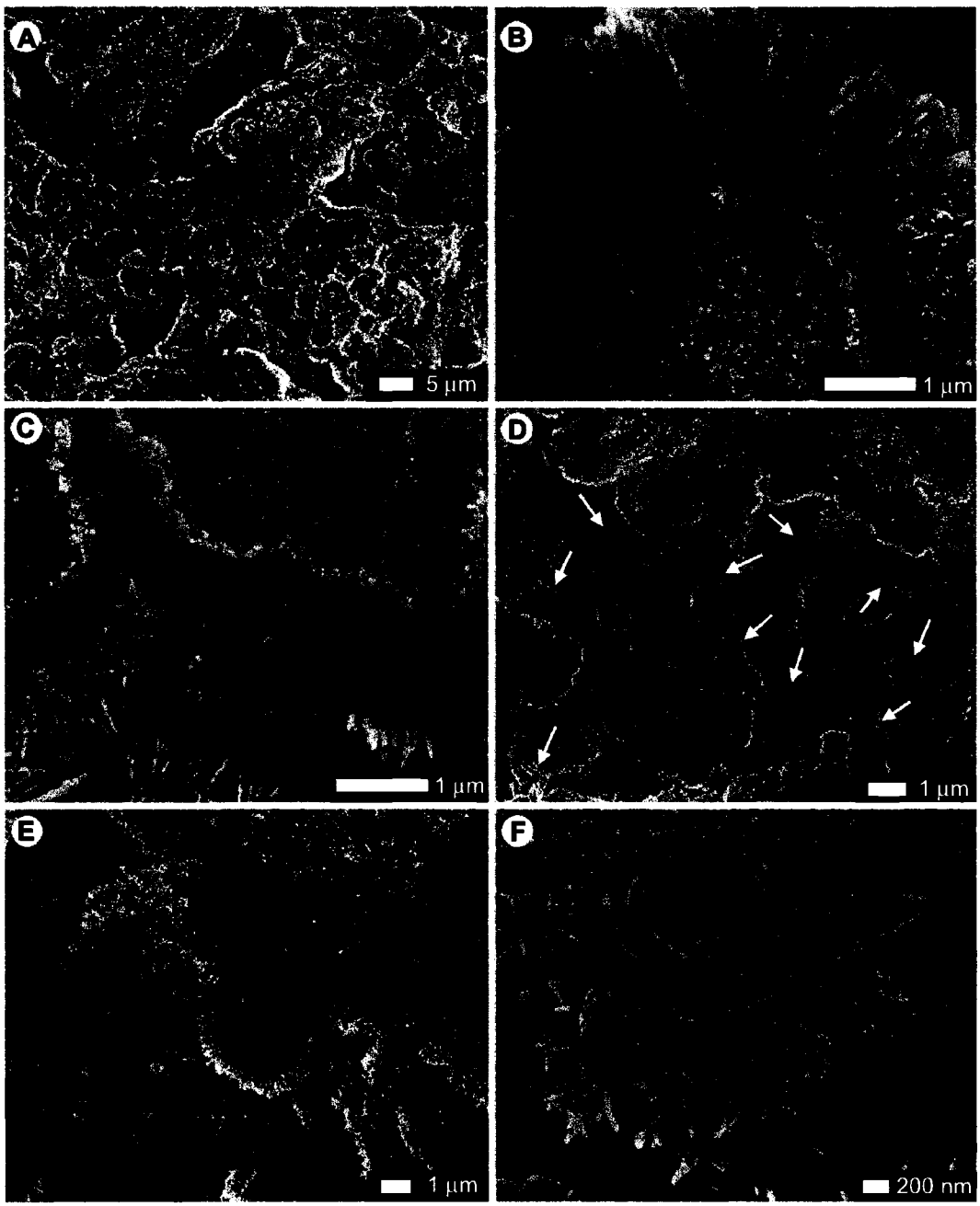

Figure 3.11. Sample NZ 816 from Geyser Flat. **A)** Multilobed masses of bumpy spheres coated in platelets in patchy vitreous (PV) sinter. **B)** Close up of bumpy sphere coated in platelets. **C)** Area vacated of bumpy spheres coated in platelets. **D)** Silica divots (arrows) found amongst lepispheres in PV sinter. **E)** Close up of silica divots and lepispheres. **F)** Close up of silica divot, formed of interesting elongated rods.

In the porous indurated sinter, multilobed masses of spheres lie amongst partially coated lepispheres (Fig. 3.10E, F). All the lepispheric microstructures observed in this lamina are partially covered in a secondary coating of silica, which merges the platelets (Fig. 3.10F).

3.1.3 Te Anarata, New Zealand

Based on XRD analyses, the sinter samples chosen for analysis from Te Anarata are composed of opal-A and opal-CT. The oldest sample, closest to the dated tephra layer, is composed of opal-CT and the youngest sample, highest above the tephra layer, is composed of opal-A. Each sample in the vertical sequence from Te Anarata is composed of several different types of siliceous sinter (Figs. 3.12A, 3.15, 3.21, 3.25).

The porous friable sinter from Te Anarata, composed of opal-A as well as opal-CT, is largely formed of silicified microbes (e.g. Fig. 3.13D-F). Other types of sinter, however, vary considerably in their microstructures.

NZ 625

This sample of siliceous sinter is the youngest sinter from the vertical sequence of strata at Te Anarata (Fig. 1.2). This sample is composed of opal-A, based on XRD analysis. The uppermost part of this sample is composed of a matrix supported breccia that is formed of porous patchy vitreous sinter with vitreous sinter fragments (Fig. 3.12). The sinter fragments in the patchy vitreous sinter are generally ~ 2 mm long. A lamina of porous friable sinter separates the patchy vitreous sinter. The lower part of this sample is composed of alternating white and grey flat-lying vitreous laminae (Fig. 3.12A).

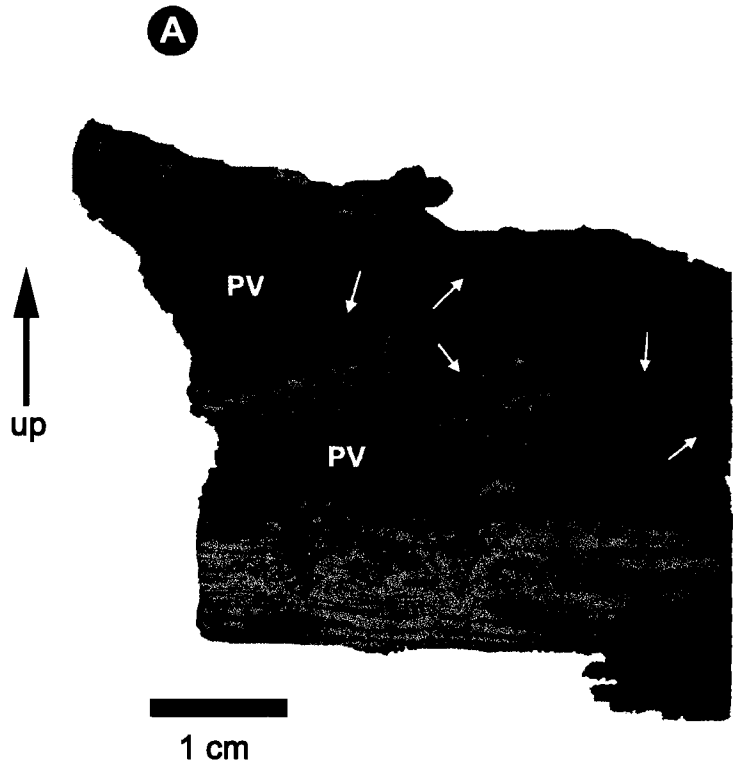

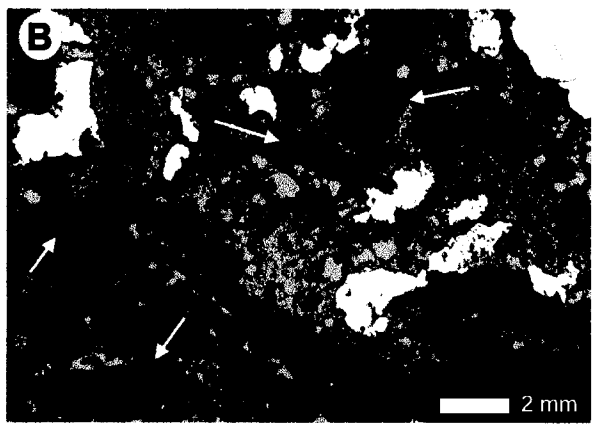

Figure 3.12. Sample NZ 625 from the top of the Te Anarata vertical section. **A)** Hand sample illustrating different type of sinter; patchy vitreous (PV), porous friable (PF), and vitreous (vit) sinter. Fragments of vitreous sinter located in the PV sinter are indicated with arrows. **B)** Photomicrograph of PV sinter with fragments of vitreous sinter (arrows).

The patchy vitreous sinter is formed of silicified microbes (Fig. 3.13A, D-F), silicified plant material (Fig. 3.13A, B), and sinter fragments (Fig. 3.13C). The porous friable sinter is formely largely of spheres, ~ 0.5 μm in diameter, and silicified microbes (Fig. 3.13E, F). The vitreous sinter is formed of spheres, 0.5-3 μm in diameter, and featureless opal (Fig. 3.14). The white vitreous sinter contains less void space than the grey vitreous sinter (Fig. 3.14A). A unimodal size distribution is found in some laminae of grey vitreous sinter (Fig. 3.14B), whereas other laminae display a variety of sphere sizes (Fig. 3.14C). Necks and connection pads are both common in the vitreous sinter (Fig. 3.14B, C, F). The vitreous sinter also displays type II inverse porosity (Fig. 3.14E). Type II inverse porosity is best illustrated in areas where spheres connected with necks are found in the immediate vicinity of spheres surrounded by cement. Illustrating the rapid changes in microstructures, spiky spheres connected with thin elongated necks are found less than 20 μm away from the type II inverse porosity (Fig. 3.14D-F).

NZ 622

In the suite of samples from the vertical succession at Te Anarata, sample NZ 622 is the second youngest sinter and is located 2 meters above the tephra deposit (Fig. 1.2). As identified by XRD analyses, the upper half of the sample (patchy vitreous, vitreous and porous indurated sinter) is composed of opal-CT whereas the lower half (patchy vitreous and porous friable) is composed of opal-A (Fig. 3.15). This sample is composed largely of highly porous patchy vitreous sinter. The transition between the porous friable, patchy vitreous and porous indurated sinter is gradational.

The patchy vitreous sinter which lies above the lamina of vitreous sinter is composed of lepispheres and bumpy spheres. Nanospheres located in pockets of smooth

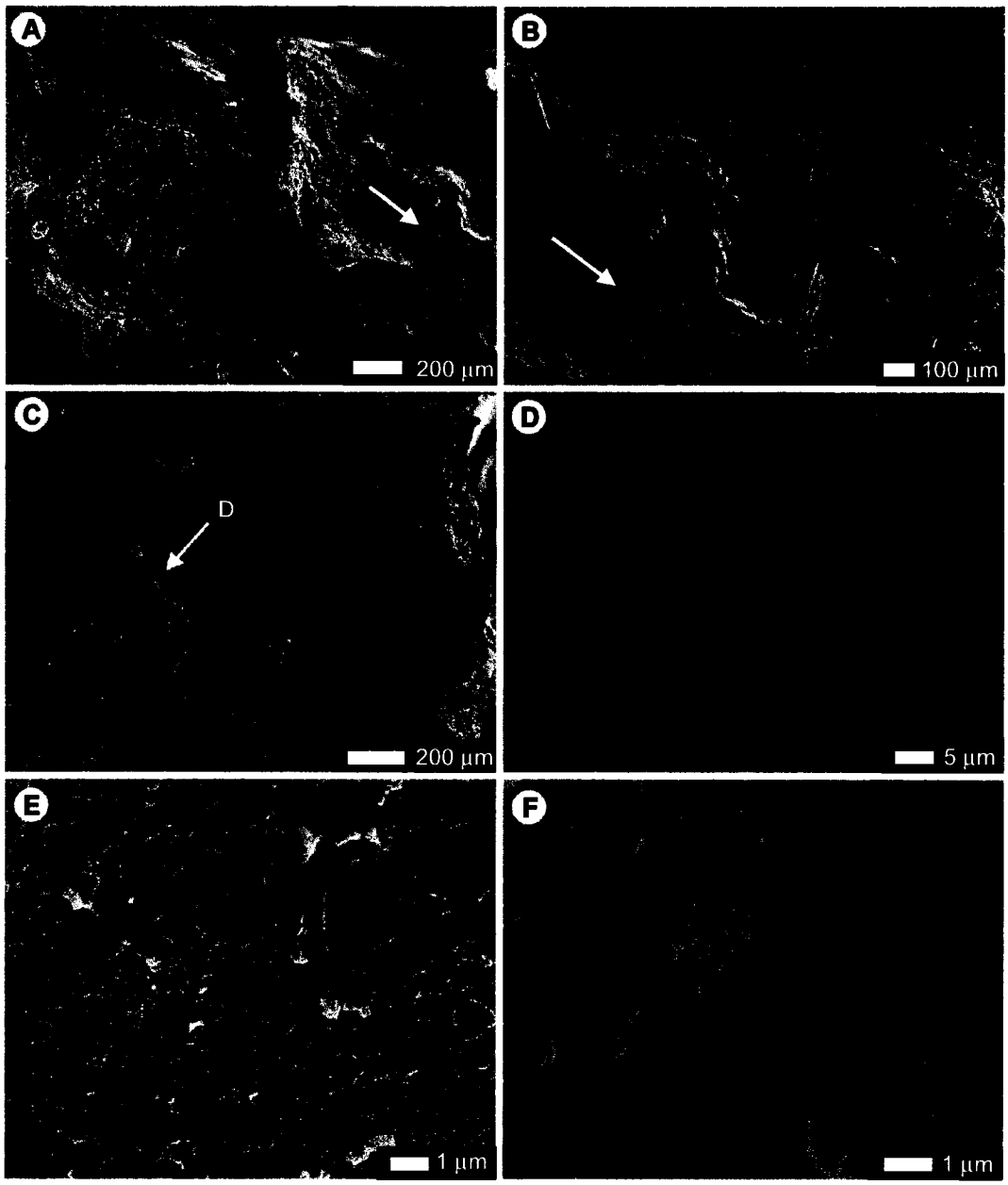

Figure 3.13. Sample NZ 625 from Te Anarata. **A)** Silicified microbes (indicated with black arrow) and plant material (white arrow, indicates location of Fig. 3.13B) in patchy vitreous (PV) sinter. **B)** Silicified plant material. Arrow is in the same location as Fig. 3.13A. **C)** Fragment of silica in PV sinter. Arrow with letter D indicates location of Fig. 3.13D. **D)** Silificified microbes in PV sinter. **E)** Cement coated spheres and silicified microbes in porous friable (PF) sinter. **F)** Spheres and silicified microbes in PV sinter.

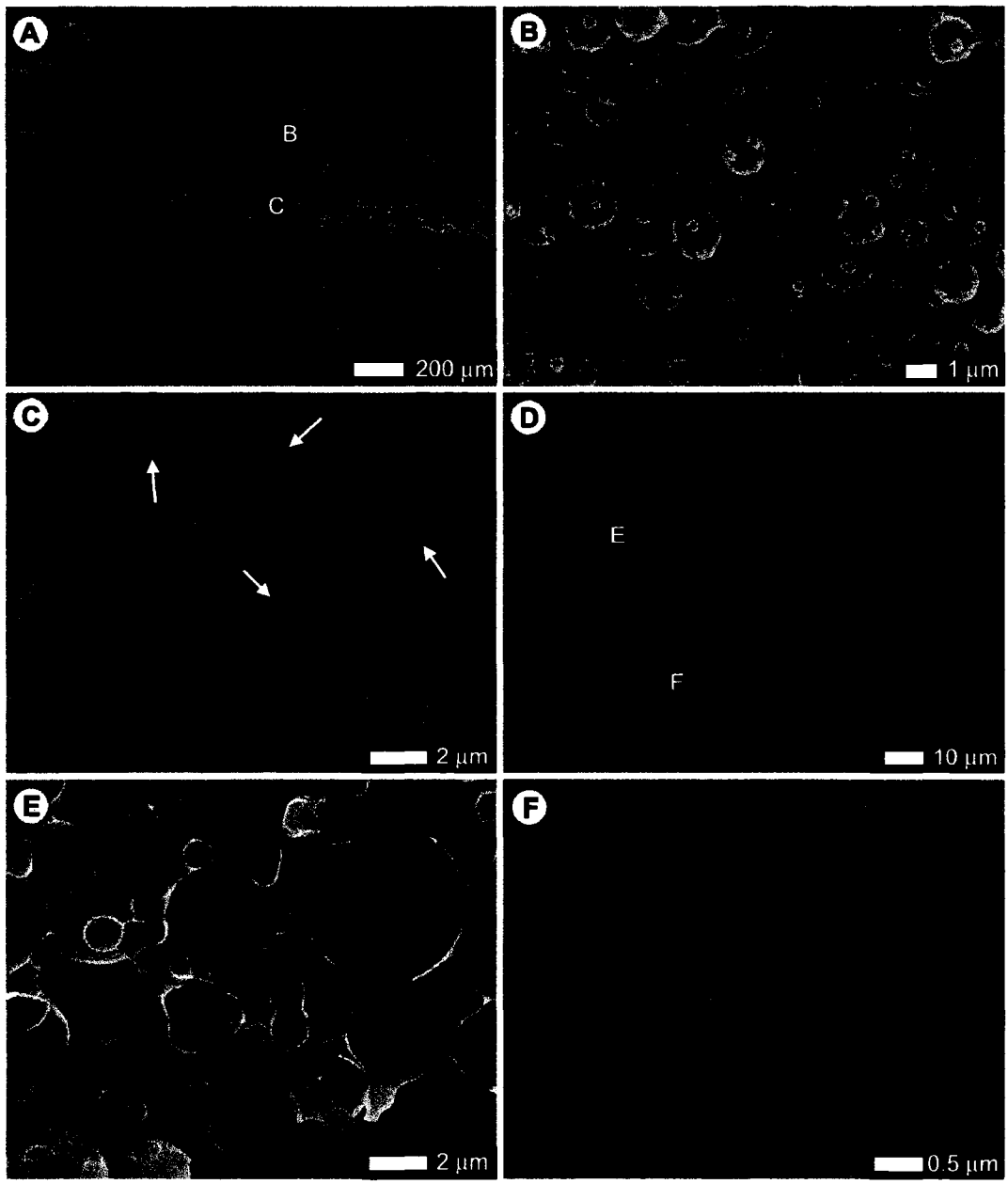

Figure 3.14. Sample NZ 625 from Te Anarata. **A)** SEM photomicrograph of vitreous sinter. Letters (B and C) indicate location of Fig. 3.14B and C. **B)** Spheres with connection pads and necks. **C)** Various sizes of spheres. Smaller spheres are connected with necks (arrows). **D)** SEM photomicrograph of vitreous sinter. Letters (E and F) indicate location of Fig. 3.14E and F. **E)** Type II inverse opal. Spheres are connected with necks in the absence of cement. **F)** Spiky spheres connected with necks in vitreous sinter.

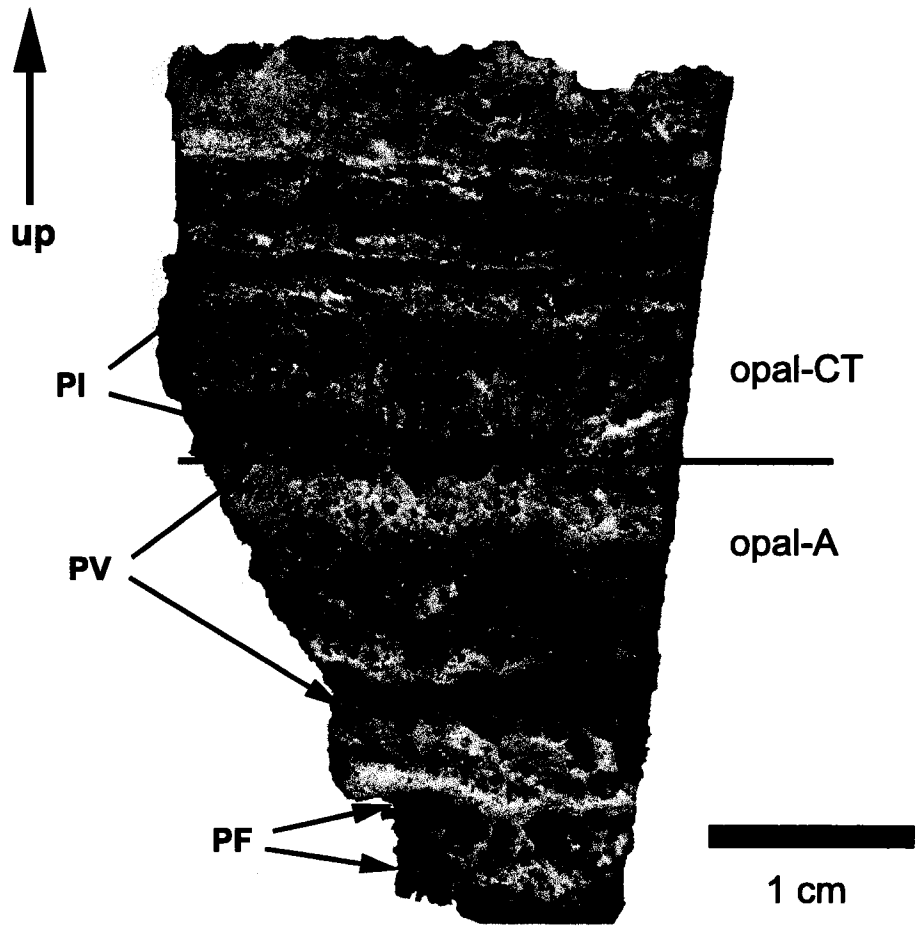

Figure 3.15. Hand sample NZ 622 from the upper portion of the Te Anarata succession illustrating different types of sinter; patchy vitreous (PV), vitreous (vit), porous indurated (PI), and porous friable (PF) sinter. Upper part of the sample is composed of opal-CT and the lower part of the sample is composed of opal-A.

featureless opal are also prominent features in this lamina of patchy vitreous sinter (Fig. 3.16A, B).

The vitreous sinter is composed largely of lepispheres. Isopachous laminae (Fig. 3.16D-F), spheres (Fig. 3.16D), type I inverse opal (Fig. 3.16C, E, F), and a relatively flat coating of ordered intersecting "microclumps" of silica (Fig. 3.16F) are also found in the vitreous sinter. Some areas of the type I inverse opal display a radiating pattern on the inner portion where spheres were once located (Fig. 3.16C).

The porous indurated sinter is formed largely of silicified microbes covered in a rough coating of silica (Fig. 3.17A, B). Partially covered bumpy spheres are also common in the porous indurated sinter (Fig. 3.17C, D). Knobby lepispheres, 2-3 μm in diameter, are found in cavitities surrounded by featureless opal (Fig. 3.17E). Smaller knobby lepispheres, 0.5 μm in diameter, contour the edge of these cavities. Smooth spheres also occur in amongst bumpy spheres in the porous indurated sinter (Fig. 3.17F).

The section of patchy vitreous sinter immediately below the porous indurated sinter is formed of clusters of bumpy spheres, which cover featureless opal (Fig. 3.18). These bumpy spheres, 200 nm to 1 μm in diameter, cluster in varying densities over smooth featureless opal (Fig. 3.18A). In cross section the bumpy spheres merge imperceptibly with featureless opal (Figs. 3.18C, 3.19B). Spherical holes, ~ 1 μm in diameter, showing isopachous laminae are found in the patchy vitreous sinter (Fig. 3.18D-F). Bumpy spheres are found in and around these holes. Nanospheres are found in the voids between bumpy spheres in the mid-section of the porous patchy vitreous sinter (Fig. 3.19A, C). Type I inverse opal is found surrounding knobby lepispheres (Fig. 3.19D, E). Bumpy spheres connected by necks are also found in the porous patchy

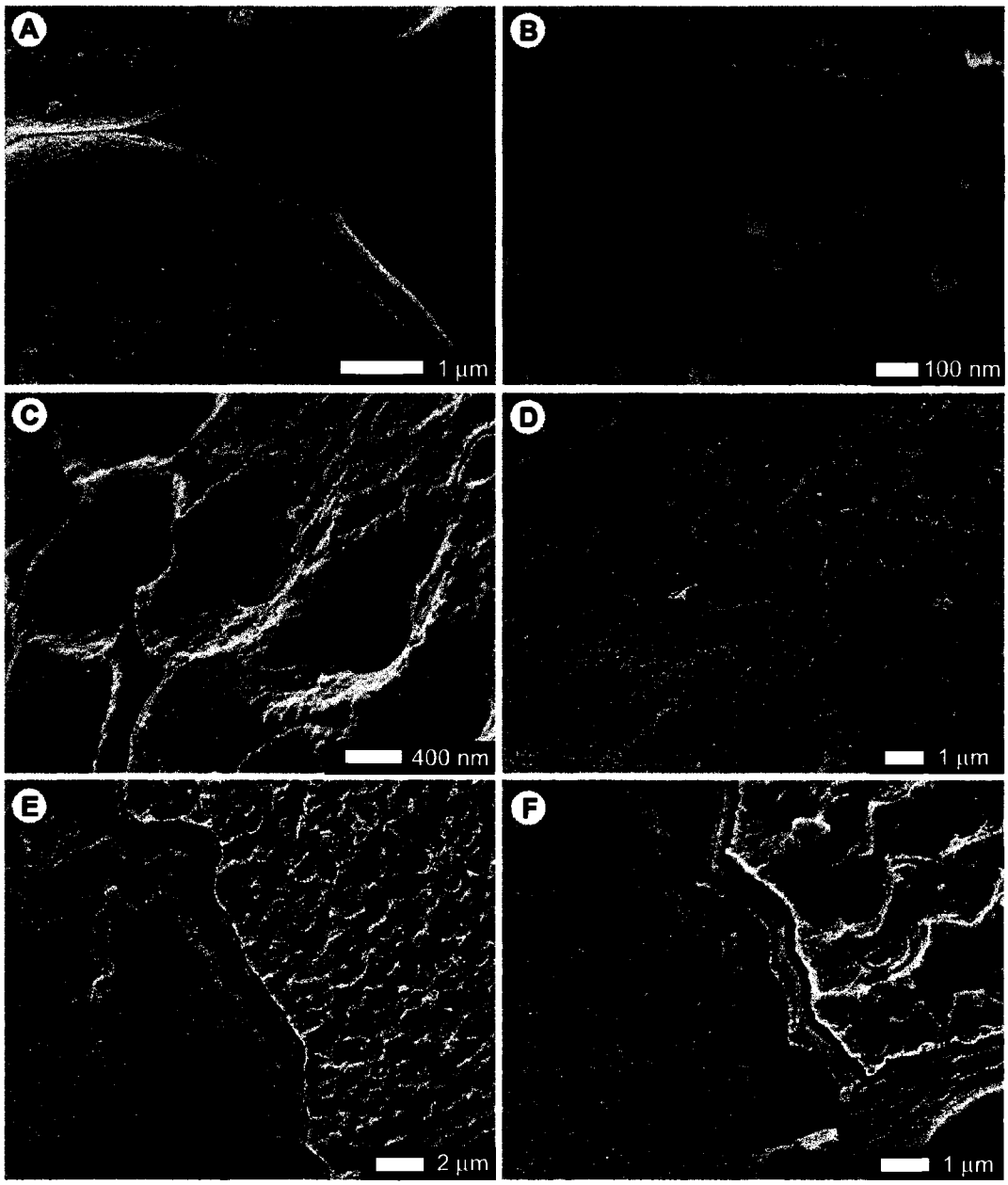

Figure 3.16. Sample NZ 622 from the upper portion of the Te Anarata succession. **A)** Nanospheres covering featureless opal in patchy vitreous (PV) sinter. **B)** Close up of nanospheres. **C)** Type I inverse opal in vitreous sinter. **D)** Isopachous laminae and spheres in vitreous sinter. **E)** Isopachous laminae separating type I inverse opal and intersecting microclumps of silica in vitreous sinter. **F)** Close up of boundary between intersecting microclumps of silica and type I inverse opal.

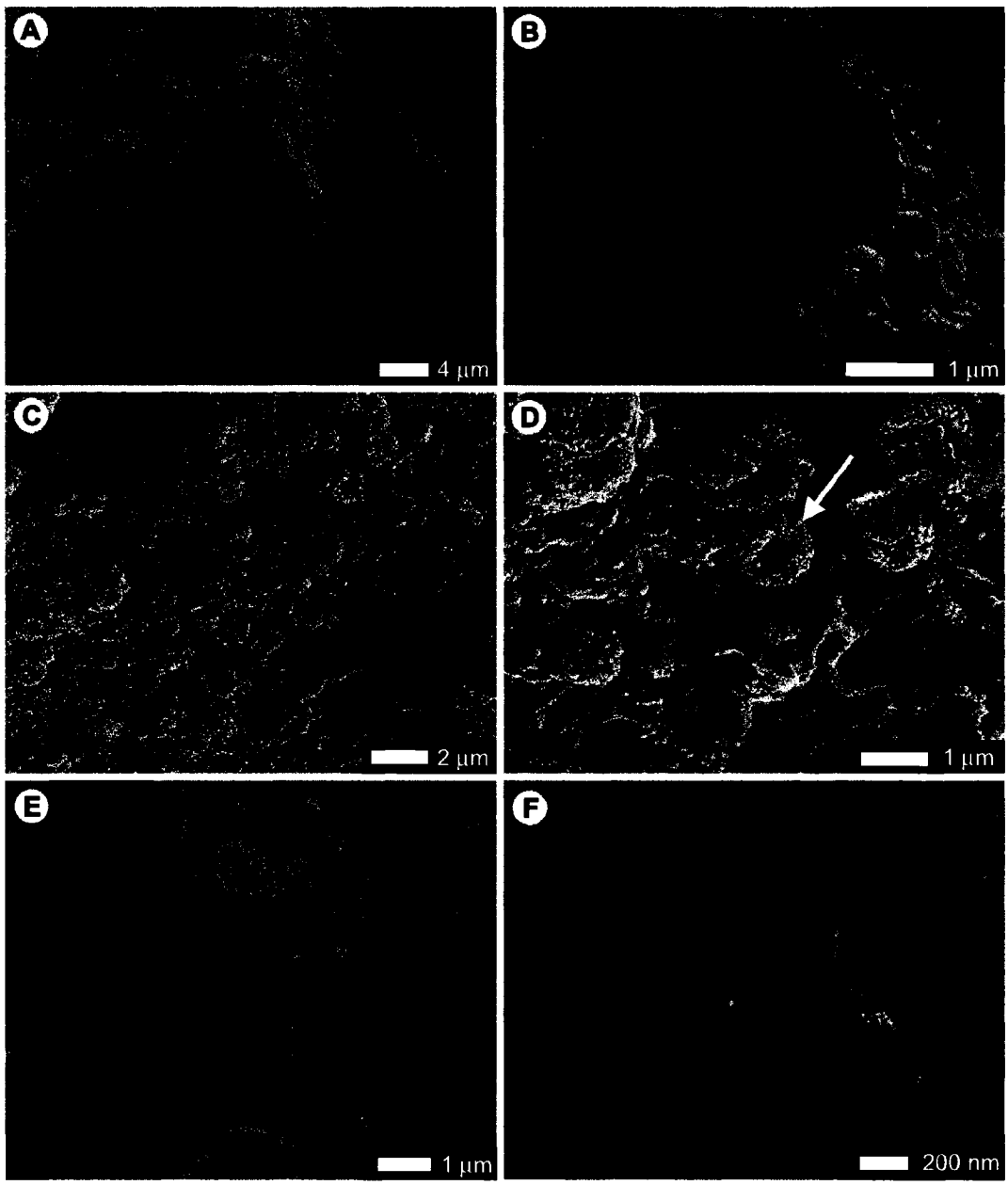

Figure 3.17. Sample NZ 622 from the upper portion of the Te Anarata succession. **A)** Silicified microbes covered in a rough coating of silica in porous indurated (PI) sinter. **B)** Hollow tube of silicified microbe has been filled in with silica. **C)** Bumpy spheres in PI sinter. **D)** Close up illustrating partially covered bumpy spheres in PI sinter. **E)** Knobby lepispheres lining cavity surrounded by featureless opal in PI sinter. **F)** Spheres and bumpy spheres in PI sinter.

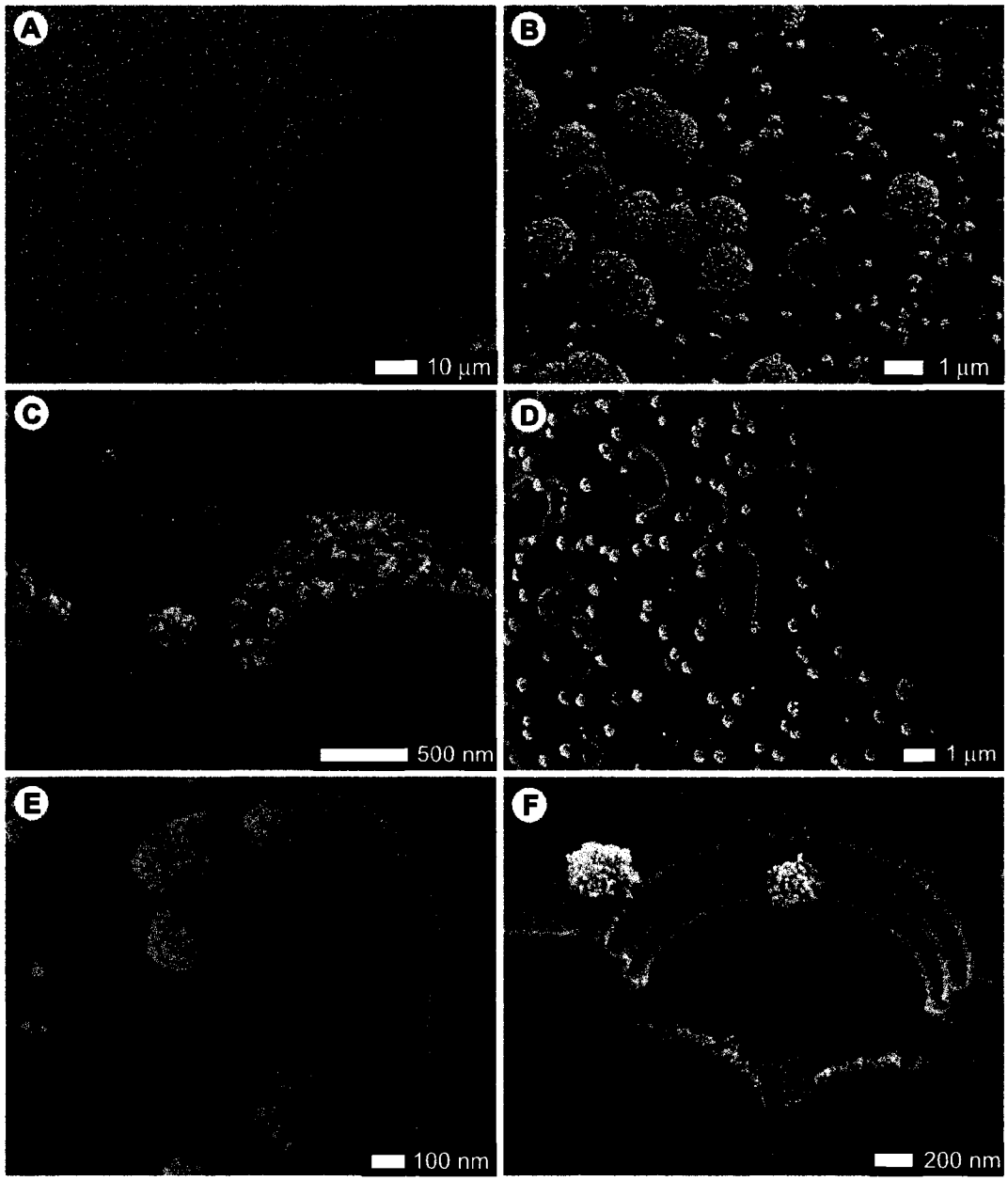

Figure 3.18. Patchy vitreous sinter in sample NZ 622 from the upper portion of the Te Anarata succession. **A)** Dense cluster of bumpy spheres covering featureless opal. **B)** Bumpy spheres and nanospheres. **C)** Cross section of bumpy sphere merging with featureless opal. **D)** Holes in featureless opal displaying isopachous laminae. **E)** Bumpy spheres in and around hole. **F)** Cross section of hole and bumpy spheres.

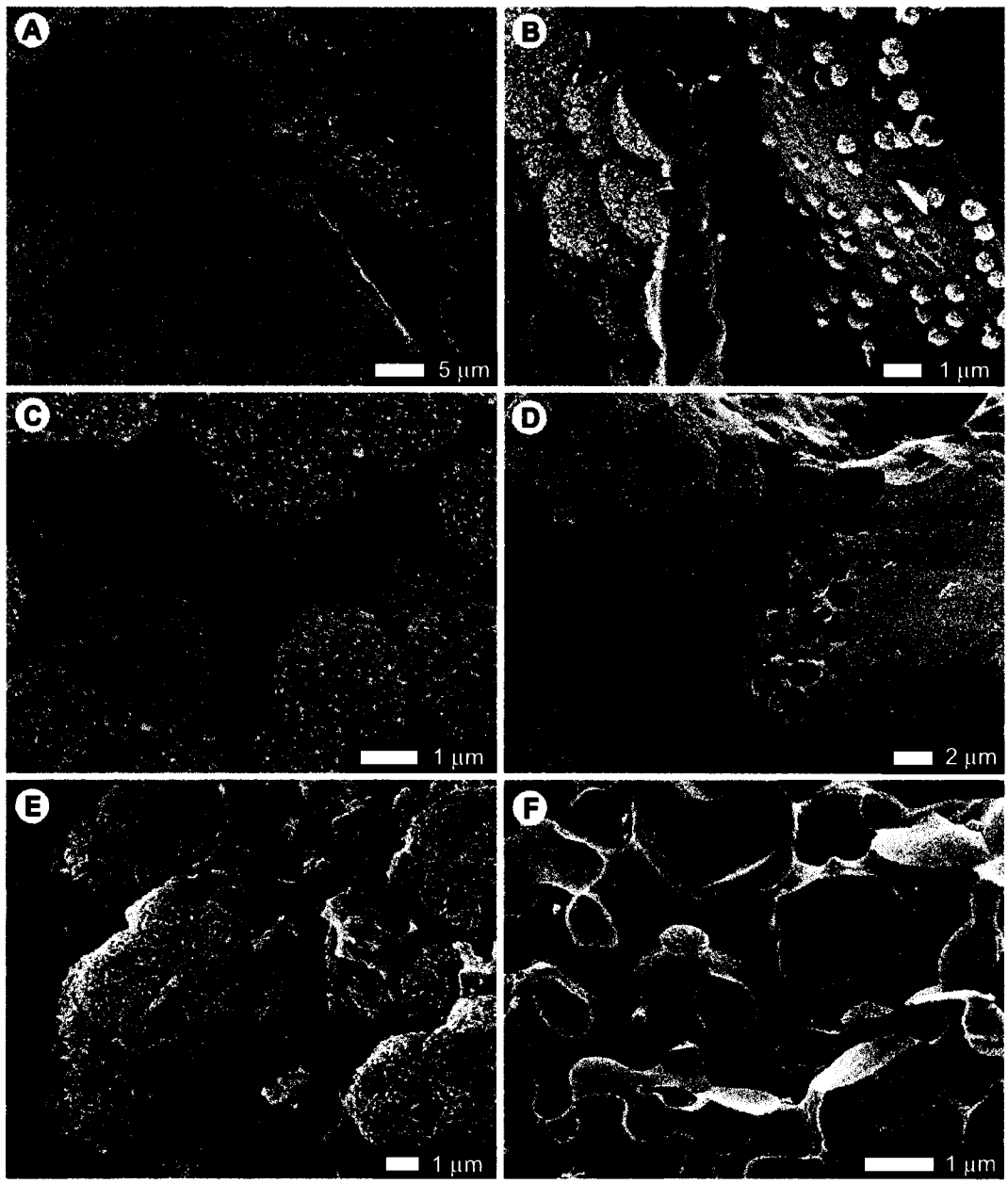

Figure 3.19. Patchy vitreous sinter in sample NZ 622 from the upper portion of the Te Anarata succession. **A)** Bumpy spheres. **B)** Bumpy spheres of variable sizes. Cross section shows solid interior of bumpy spheres. **C)** Nanospheres located between bumpy spheres. **D)** Type I inverse opal and knobby lepispheres. **E)** Knobby lepispheres with remains of type I inverse opal. **F)** Bumpy spheres connected with necks.

vitreous sinter (Fig. 3.19F). The lower portion of the patchy vitreous sinter, immediately above the porous friable sinter, is formed of nodular spheres (Fig. 3.20A, B) and smooth silicified microbes (Fig. 3.20C, D). The porous friable sinter is formed of silicified microbes with a bumpy texture (Fig. 3.20E, F).

NZ 618

Located 1.6 meters above the tephra deposit (Fig. 1.2), this sample is formed of patchy vitreous and porous friable sinter with flat-lying laminae of vitreous sinter (Fig. 3.21A). This sample is composed entirely of opal-CT, based on XRD analysis.

The upper patchy vitreous sinter is composed primarily of type I inverse opal (Fig. 3.22A-D). In the type I inverse opal, there are spheres with connection pads (Fig. 3.22B), and bumpy spheres surrounded by cement (Fig. 3.22D). The lower patchy vitreous sinter is comprised largely of bumpy spheres with much less cement than type I inverse opal (Fig. 3.23C-E). Lepispheres are also common in the lower patchy vitreous sinter (Fig. 3.23F).

The porous friable sinter is composed of silicified microbes (Fig. 3.22E). Scalloped surfaces, isopachous laminae, bumpy spheres, and nanospheres are found around the silicified microbes in much of the porous friable sinter (Fig. 3.22E). The nanospheres cover otherwise featureless opal (Fig. 3.22F). The vitreous sinter is formed of closely neighbouring spheres, intercalated platelets and bumpy spheres (Fig. 3.23A, B).

NZ 613

This sample is the oldest deposit in the Te Anarata sequence, as it lies direcly above the tephra deposit (Fig. 1.2). Opal-CT and quartz were identified using XRD

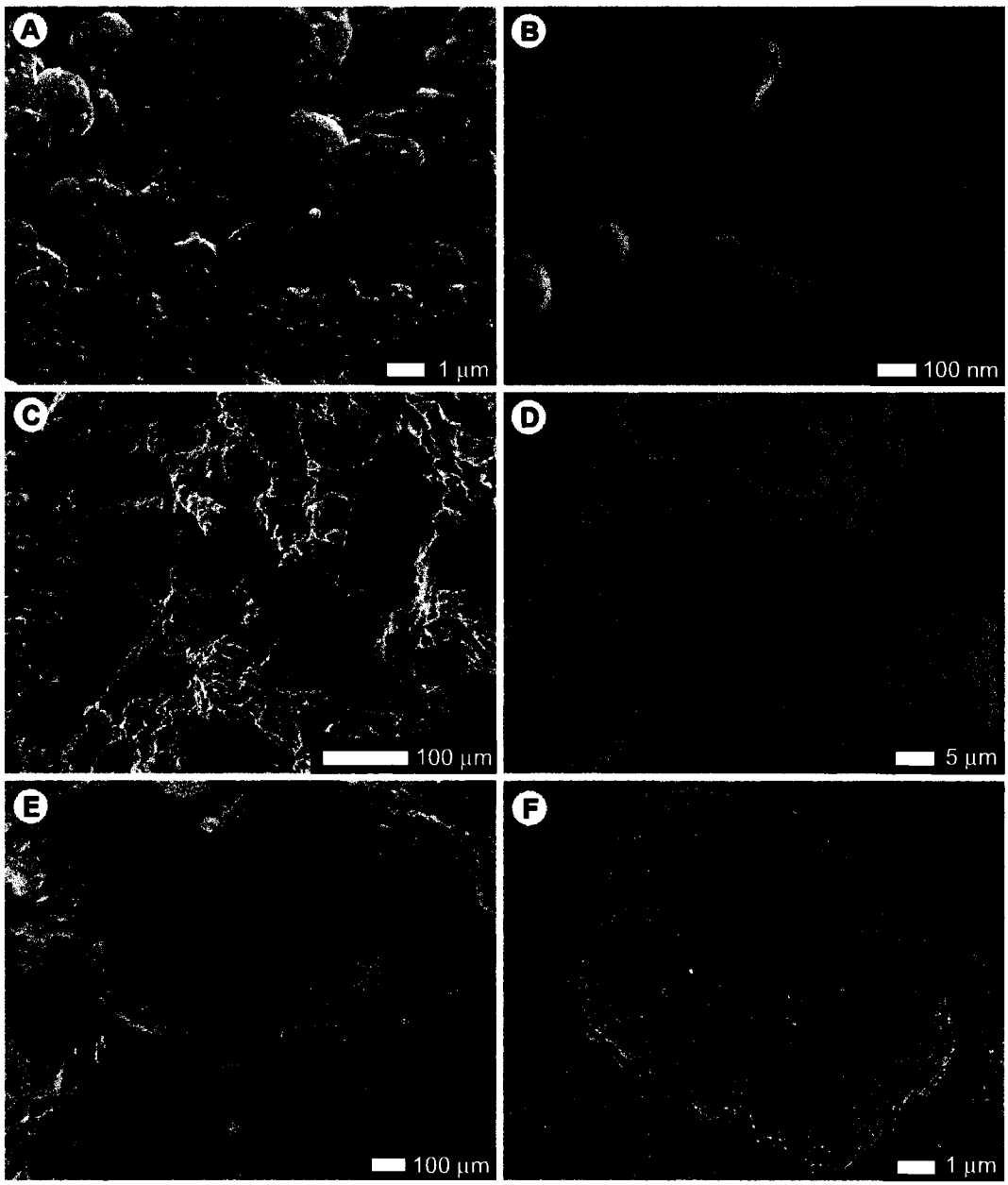

Figure 3.20. Sample NZ 622 from the upper portion of the Te Anarata succession. **A)** Nodular spheres in patchy vitreous (PV) sinter. **B)** Close up of nodular spheres. **C)** Silicified microbes in PV sinter. **D)** Close up showing smooth coating of silicified microbes in PV sinter. **E)** Silicified microbes in porous friable (PF) sinter. **F)** Close up showing bumpy coating of silicified microbes in PF sinter.

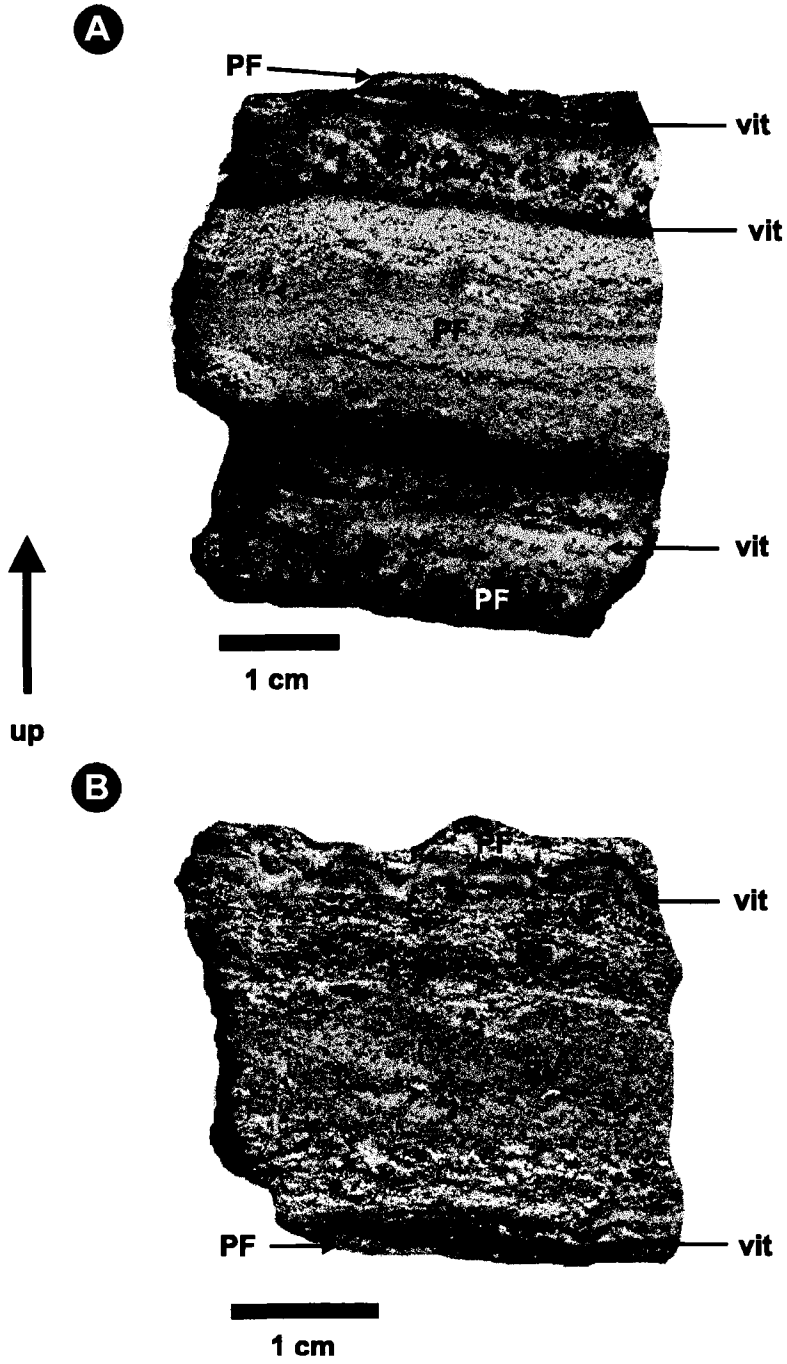

Figure 3.21. Hand samples from lower portion of Te Anarata succession showing different types of sinter; porous friable (PF), patchy vitreous (PV), and vitreous (vit) sinter. **A)** Sample NZ 618. **B)** Sample NZ 613.

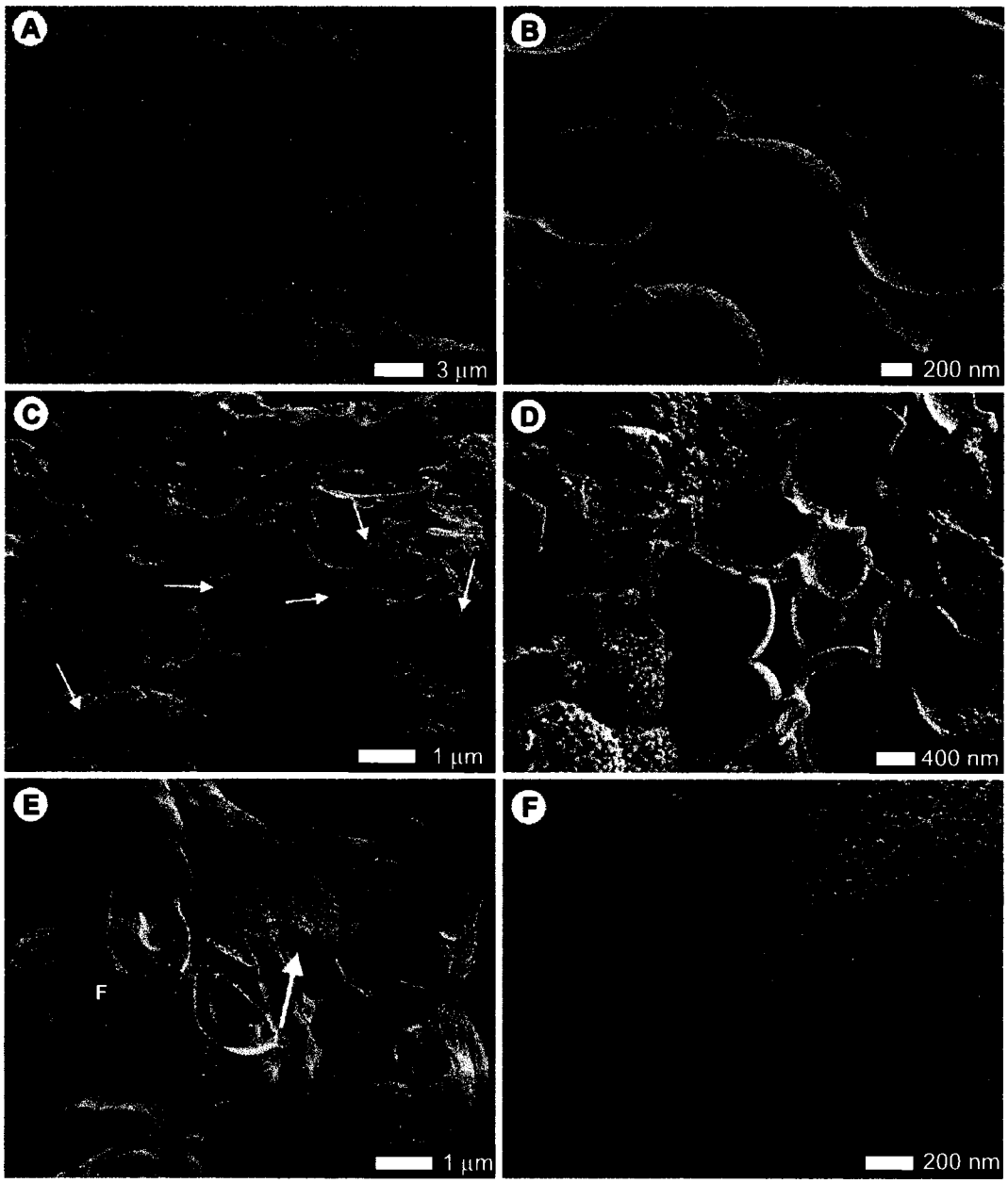

Figure 3.22. Sample NZ 618 from the lower portion of the Te Anarata succession. **A)** Type I inverse opal in patchy vitreous (PV) sinter. **B)** Close up of type I inverse opal showing spheres with connection pads. **C)** Type I inverse opal in PV sinter with bumpy spheres (arrows). **D)** Type I inverse opal in PV sinter with bumpy spheres. **E)** Silicified microbe showing hollow tube. Scalloped surface and bumpy spheres (white arrow) in porous friable (PF) sinter. Letter F indicates location of Fig. 3.22F. **F)** Close up showing nanospheres.

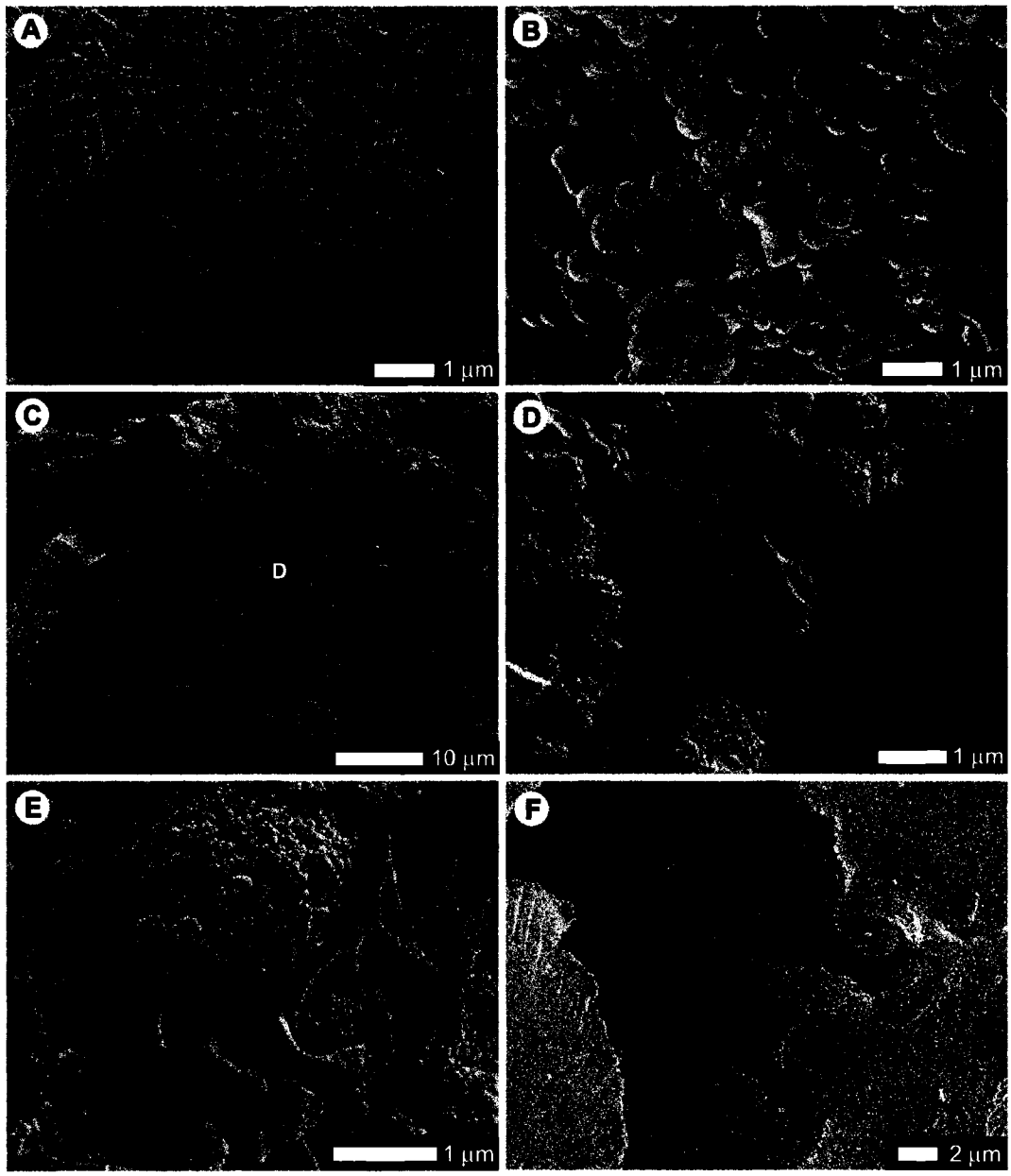

Figure 3.23. Sample NZ 618 from the lower portion of the Te Anarata succession. **A)** Intercalated platelets with spheres in vitreous sinter. **B)** Spheres and bumpy spheres in vitreous sinter. **C)** Overview of patchy vitreous (PV) sinter. Letter D indicates location of Fig. 3.23D. **D)** Bumpy spheres with cement from type I inverse opal. **E)** Close up of bumpy spheres with cement from type I inverse opal. **F)** Lepispheres lining cavity in PV sinter surrounded by featureless opal.

analysis of this sample. This sample is composed of relatively flat-lying laminae of porous friable, patchy vitreous, and vitreous sinter (Fig. 3.21B).

The porous friable sinter is formed of numerous silicified microbes covered in multilobed masses of spheres (Fig. 3.24A, B). The patchy vitreous sinter is composed of bumpy spheres, 1-2 μm in diameter, surrounded by nanospheres (Fig. 3.24C, D). Lepispheres were only observed in the vitreous sinter. Knobby lepispheres (Fig. 3.24E) and nanospheres are also found in the vitreous sinter throughout the sample. In the upper wavy lamina of vitreous sinter, gypsum crystals are observed (Fig. 3.24F). These crystals, are formed of Ca and S as identified by EDX (cf. XRD results).

3.1.4 Geysir, Iceland

The two samples chosen for analyses denote an important mineralogical discontinuity in the sinter succession in Geysir (Jones and Renaut in press). Sample ICE-87, composed of opal-A, lies immediately above sample ICE-86, composed of opal-CT (Fig. 1.4). Both samples are formed of several different types of sinter (Fig. 3.25) with variable microstructures.

ICE-87

This siliceous sinter, composed of opal-A, is formed of porous friable sinter and patchy vitreous sinter (Fig. 3.25A).

The porous friable sinter is composed of multilobed masses of spheres (Fig. 3.26A). The interiors of these masses are formed of scalloped surfaces and rough masses of silica (Fig. 3.26B). Isopachous laminae are prominent in the patchy vitreous sinter (Fig. 3.26C-F). The isopachous laminae highlight the interior features of multilobed

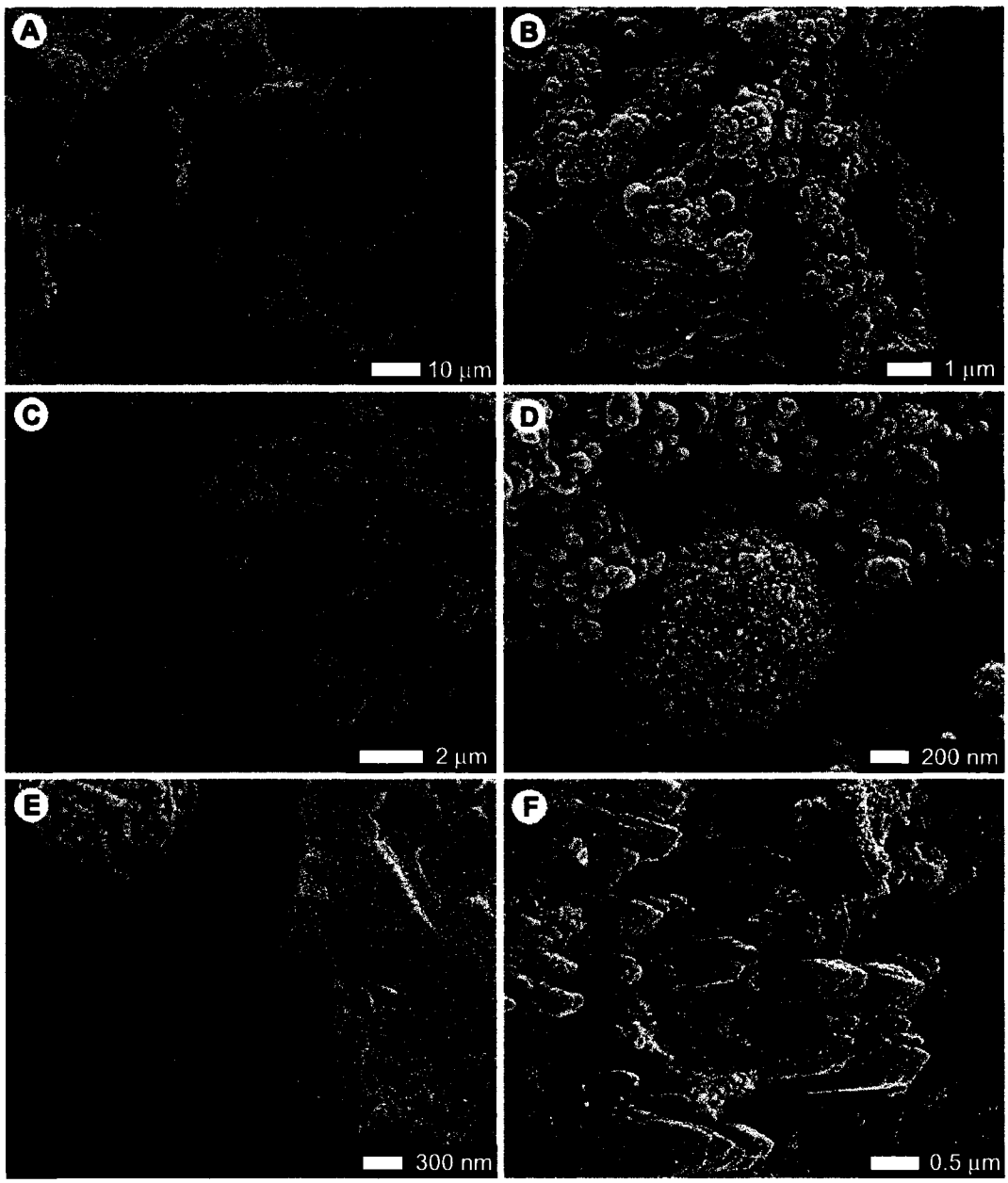

Figure 3.24. Sample NZ 613, the oldest sinter in the Te Anarata succession. **A)** Silicified microbes in porous friable (PF) sinter. **B)** Close up of silicified microbes in PF sinter showing multilobed masses of spheres. **C)** Bumpy spheres and nanospheres in patchy vitreous (PV) sinter. **D)** Close up of a bumpy sphere surrounded by nanospheres in PV sinter. **E)** Knobby lepispheres lining a cavity surrounded by featureless opal in vitreous sinter. **F)** Gypsum crystals in featureless opal in vitreous sinter.

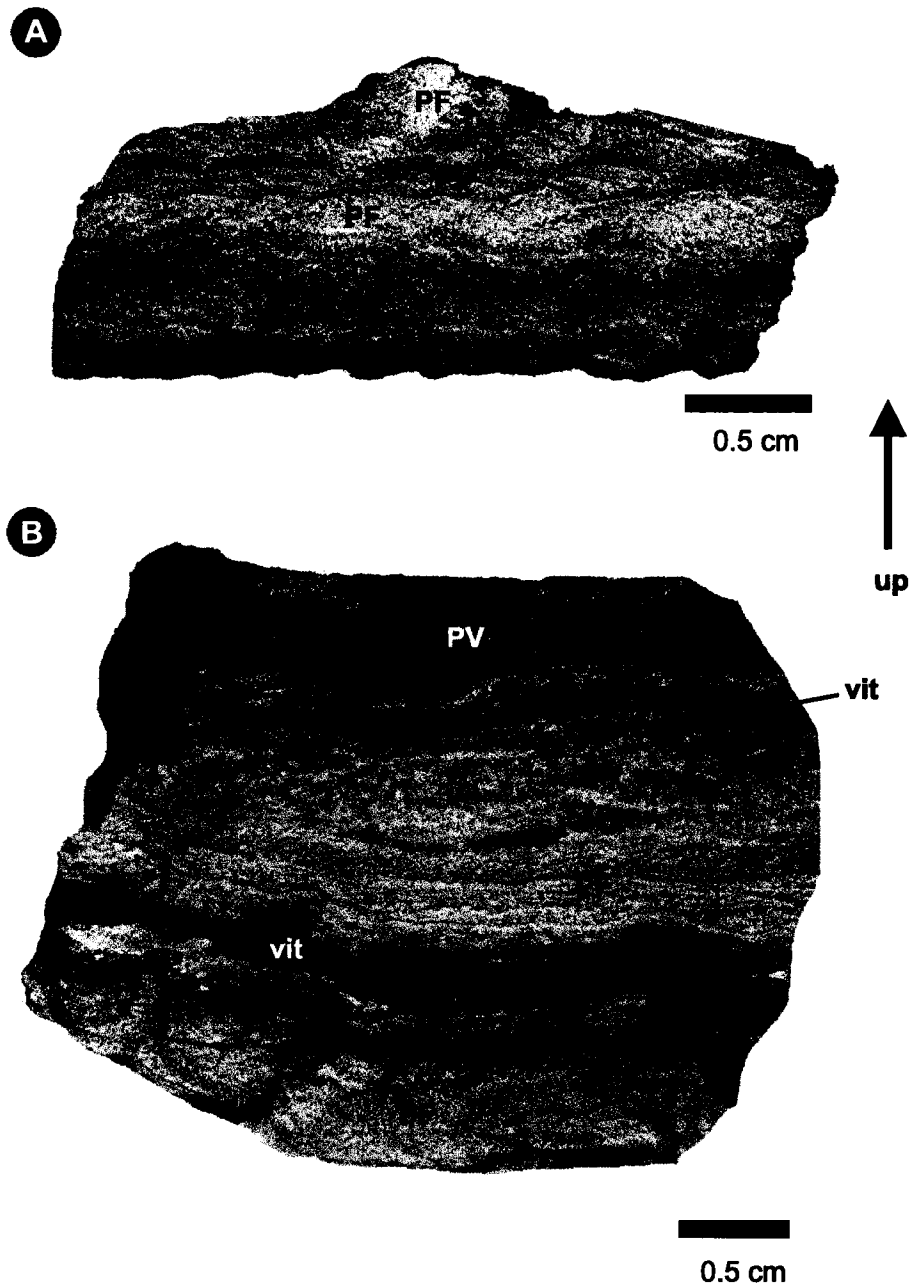

Figure 3.25. Hand samples from Geysir, Iceland showing different types of sinter; patchy vitreous (PV), porous friable (PF) and vitreous (vit) sinter. **A)** Sample ICE-87, composed of opal-A. **B)** Sample ICE-86, composed of opal-CT.

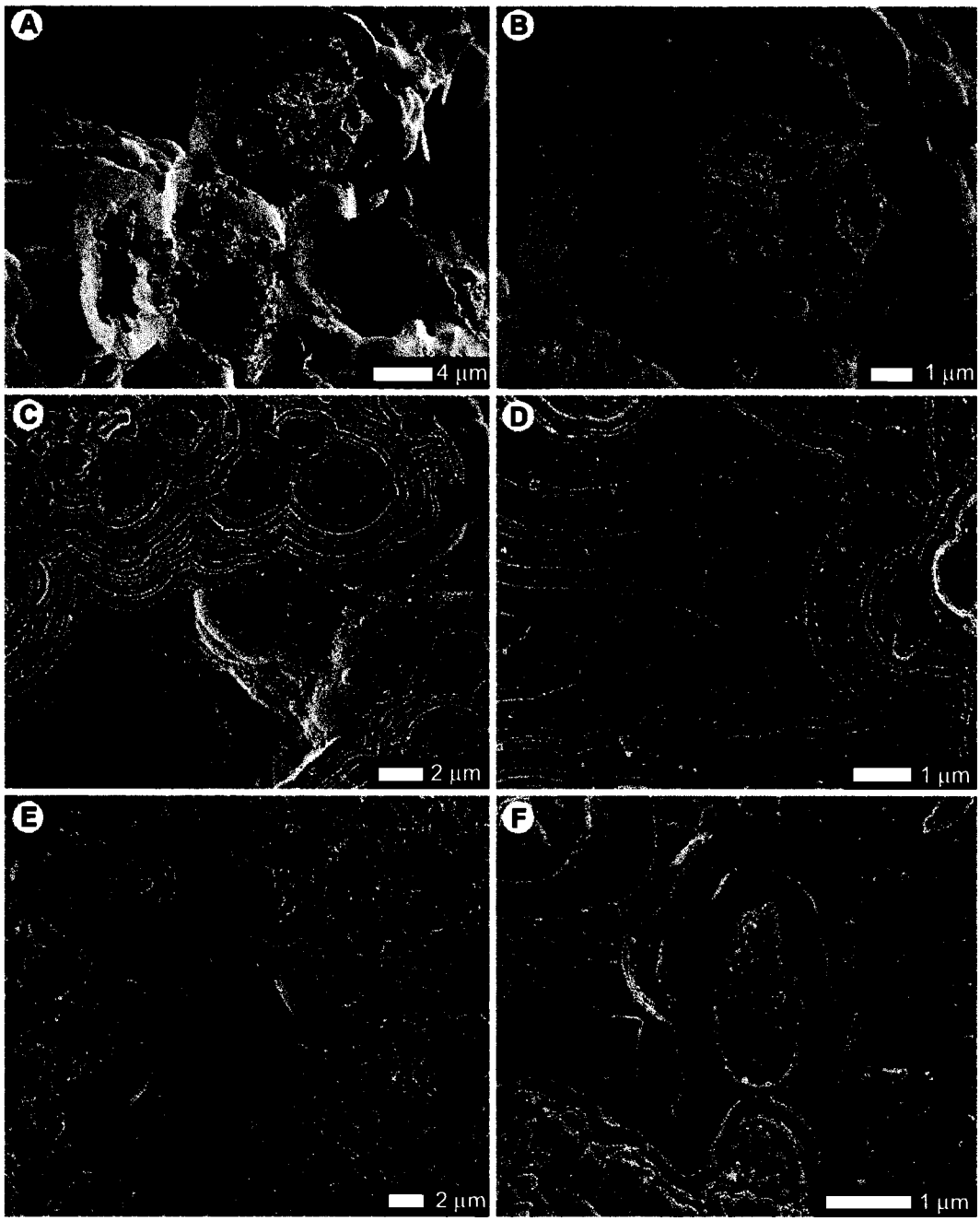

Figure 3.26. Sample ICE-87 from Geysir, Iceland. **A)** Multilobed masses of spheres with rough silica mass in porous friable (PF) sinter. **B)** Close up of rough silica mass in PF sinter. **C)** Etching of multilobed masses of spheres showing inner structure of spheres and multiple layers of silica in patchy vitreous (PV) sinter. **D)** Isopachous laminae of opal cement in PV sinter. **E)** Isopachous laminae in PV sinter, **F)** Etching of silicified microbe in PV sinter.

masses of spheres (Fig. 3.26C), the formation of opal cements (Fig. 3.26D, E) and in some instances highlight the presence of silicified microbes (Fig. 3.26F).

ICE-86

This sample is located directly below sample ICE-87 in the vertical sequence at Geysir. XRD analysis indicates this sample is composed of opal-CT. It is formed of flat-lying to slightly undulose laminae of patchy vitreous, porous friable, and vitreous sinter (Fig. 3.25B).

The patchy vitreous sinter is composed of silicified microbes, spheres connected with ringed necks (Fig. 3.27A) and type I inverse opal (Fig. 3.27B). Bumpy spheres are found in some areas of type I inverse opal. Spheres, ~ 1 μm in diameter, are found in cavities adjacent to intercalated platelets (Fig. 3.27C). The porous friable sinter is composed of silicified microbes (Fig. 3.27F). The upper laminae of vitreous sinter is composed of spheres, whereas the lower vitreous laminae is composed mainly of type I inverse opal surrounding large bumpy spheres (Fig. 3.27E).

3.1.5 Morphology Synopsis: Opal-A vs. Opal-CT

Siliceous sinters composed of opal-A and/or opal-CT are generally formed of a variety of different sinter types (e.g., Figs. 3.1, 3.15, 3.25). It is apparent that neither deposits of opal-A nor opal-CT are dominated by any particular type of sinter; for example porous friable sinter is common to sinters composed of opal-A as well as sinters composed of opal-CT (e.g. Fig. 3.25). It is not possible to distinguish opal-A from opal-CT in hand sample, they are only distinguished using XRD analysis.

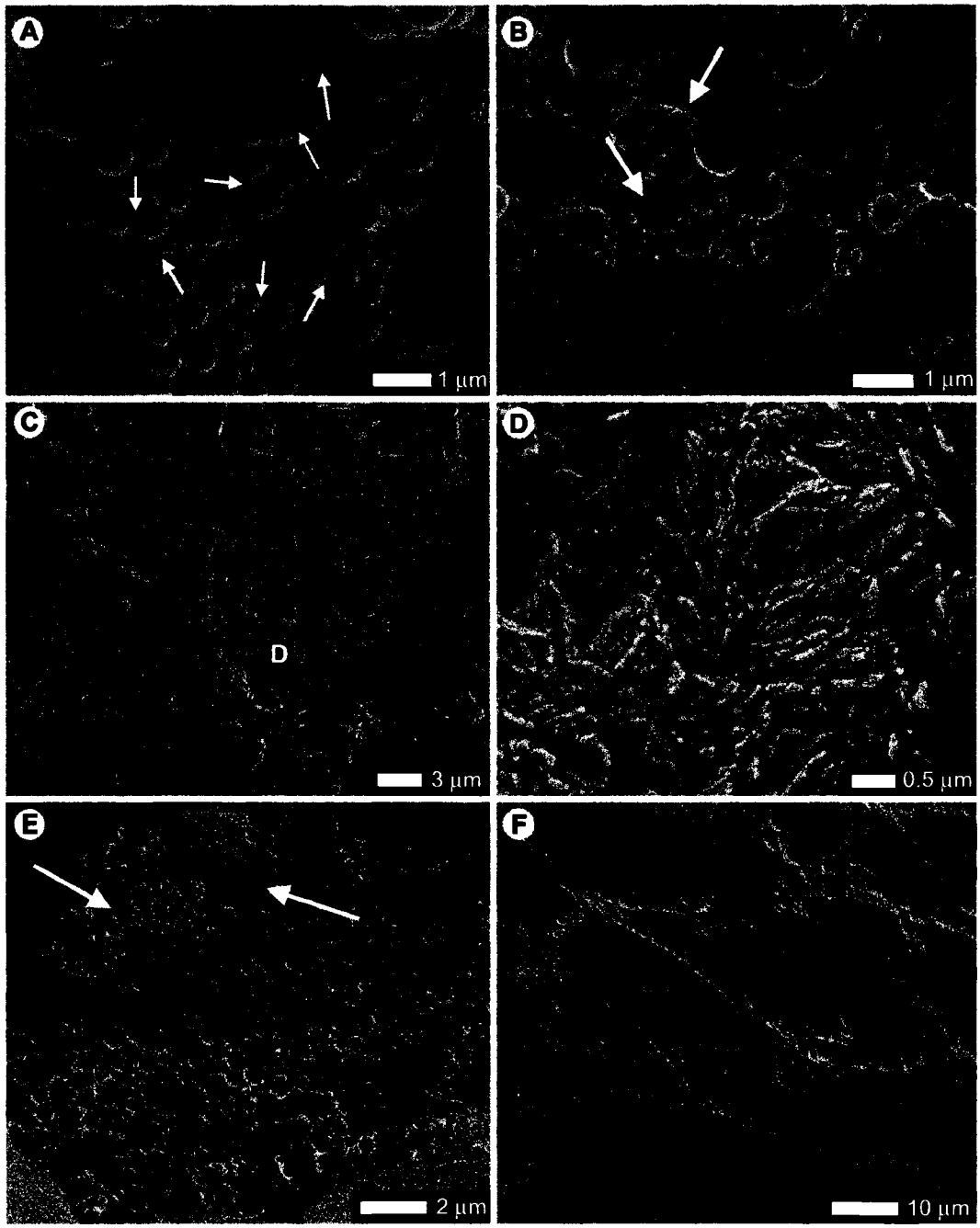

Figure 3.27. Sample ICE-86 from Geysir, Iceland. **A)** Spheres connected with ringed necks (arrows) in patchy vitreous (PV) sinter. **B)** Type I inverse opal with bumpy spheres developing in spherical cavities (arrows) in PV sinter. **C)** Cavity of spheres neighboured by intercalated platelets. Letter D indicates location of Fig. 3.27D. **E)** Bumpy spheres (arrows) and type I inverse opal in vitreous sinter. **F)** Silicified microbes in porous friable sinter.

Sinters composed of opal-A are commonly formed of spheres, featureless opal, and silicified microbes (Fig. 3.28). The spheres found in sinter composed of opal-A are commonly connected with connection pads and necks, and less commonly by ringed necks. Features such as bumpy spheres and inverse opal are rarely found in sinter composed of opal-A. Sinters composed of opal-CT are most commonly formed of lepispheres, bumpy spheres, silicified microbes, and nanospheres (Fig. 3.28). Knobby lepispheres, intercalated platelets, type I inverse opal, and spheres are also common in sinter composed of opal-CT. Isopachous laminae and scalloped surfaces occur in sinters composed of either opal-A or opal-CT. Silicified microbes are the most widespread feature found in siliceous sinter composed of either opal-A or opal-CT (Fig. 3.28).

3.2 Water Content Results

3.2.1 Waikite Geyser Complex, New Zealand

NZ 592

Sample NZ 592 (opal-A), located closest to the main vent, is composed of porous indurated sinter with spicules, and flat-lying laminae of vitreous, patchy vitreous and dull indurated sinter. The spicules in this sample, composed of vitreous sinter, are formed of alternating laminations of dark and light grey opal (BSEI) (Fig. 3.29B, C). Respectively, the dark and light grey opal (BSEI) laminations in the vitreous sinter correspond to the opaque and translucent laminations seen in thin section (Fig. 3.29A). Flat-lying laminae of vitreous sinter in this sample show similar laminations of dark and light grey opal (BSEI). The porous indurated, patchy vitreous and dull indurated sinters in this sample appear homogeneous in grey shades on BSEI (Fig. 3.29D). Elements other than Si and O

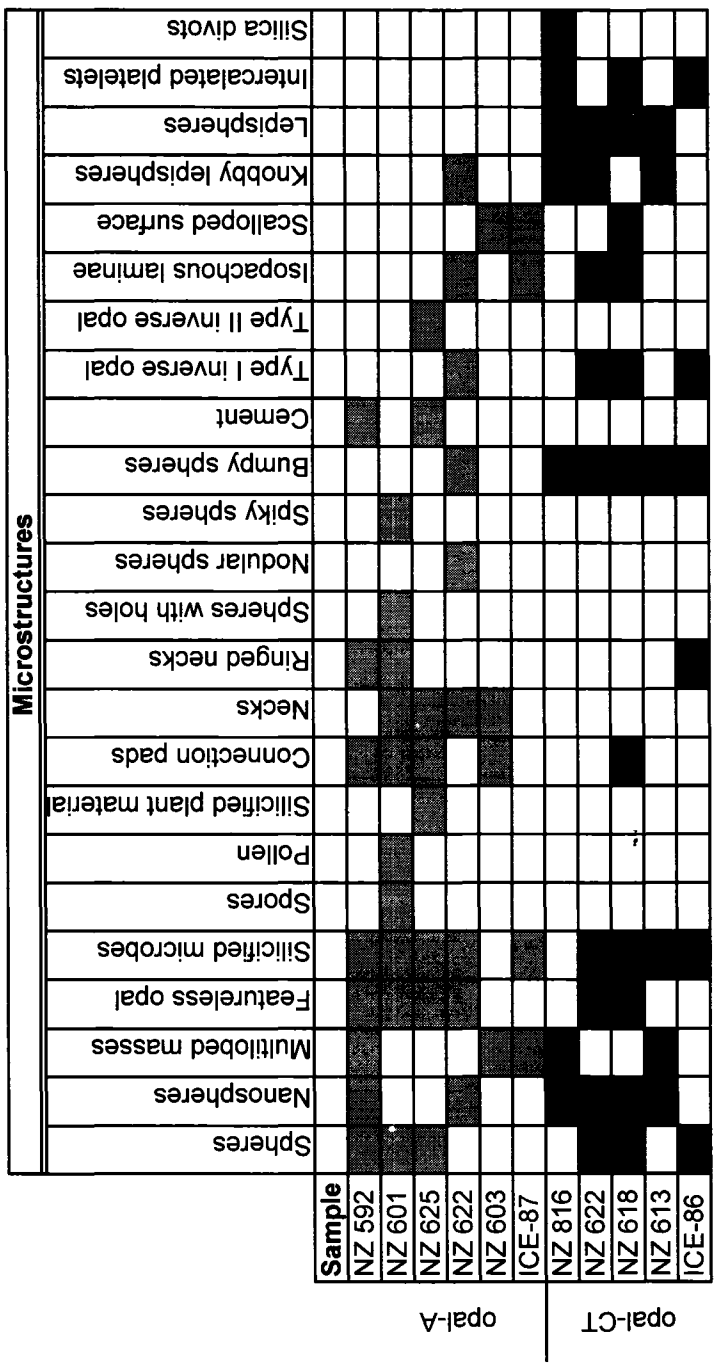

Figure 3.28. Distribution of microstructures in sinter deposits composed of opal-A (grey) and opal-CT (black).

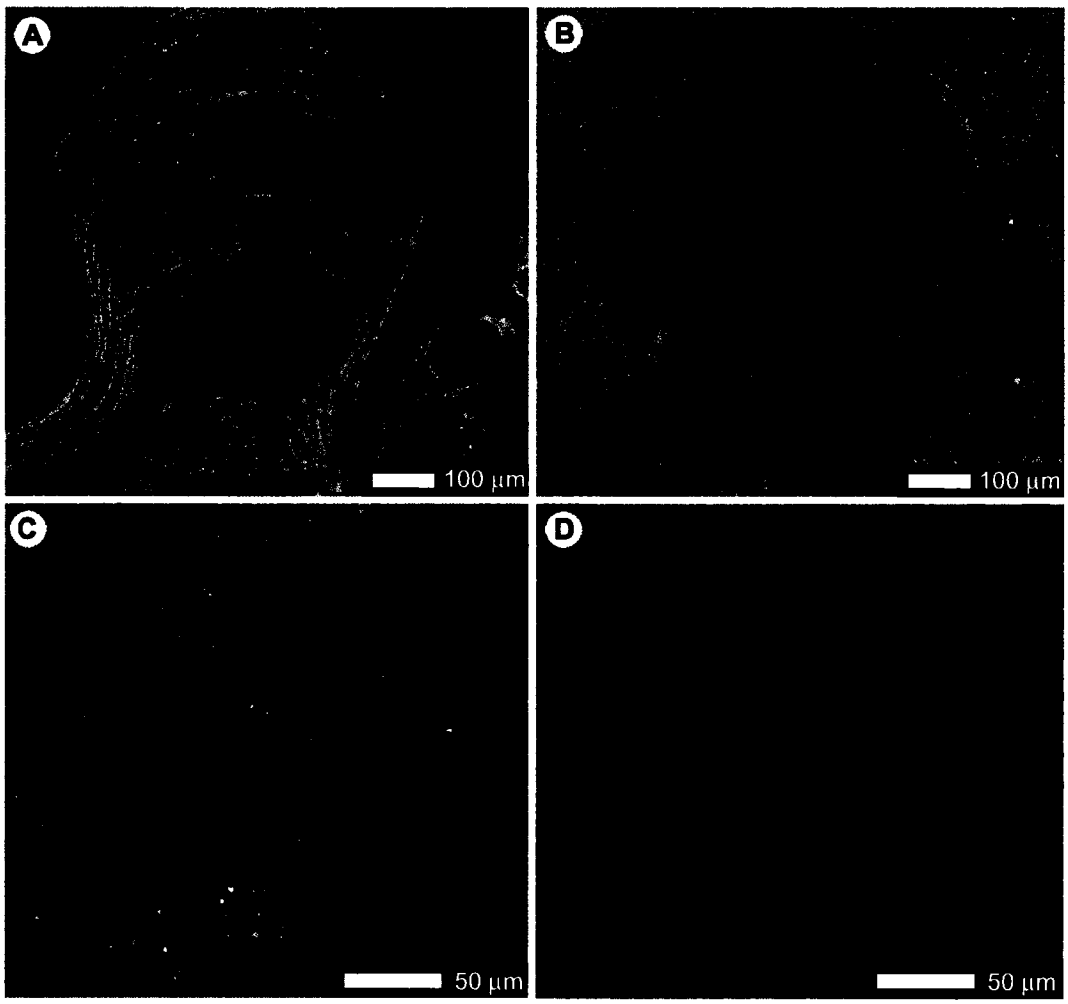

Figure 3.29. Sample NZ 592 from the Waikite Geyser complex, proximal to the main vent. **A)** Photomicrograph of a spicule, composed of vitreous sinter, showing thin laminations. **B)** Backscattered electron image (BSEI) of spicule from Fig. 3.29A showing corresponding light and dark opal (BSEI) laminations. Electron microprobe analysis indicates light opal (BSEI) contains 8.5 wt % total water and dark opal (BSEI) contains 12.1 wt % total water. **C)** BSEI close up of the base of the spicule. **D)** Close up of porous indurated sinter surrounding the spicule. No constrast in average atomic weight is evident. Dark areas have a high porosity.

(Al, Ca, Mg etc.) comprise less than 1 wt % of this sample. The dark and light grey opal (BSEI) observed in this sample must therefore reflect variations in total water content (Jones and Renaut 2004). Dark grey opal (BSEI) has 11-12 wt % total water, whereas the associated light grey opal contains 6-8 wt % total water (Table 3.1, Fig. 3.30A).

The total water contents obtained using EMP and FTIR analyses are within the limits of analytical error for all types of sinter in this sample, except for the porous indurated sinter (e.g. 4.7 ± 0.8 wt % vs. 9.4 ± 0.7 wt %; EMP vs. FTIR, respectively) (Table 3.1). The differences in total water content calculated in the porous indurated sinter are probably due to complications in FTIR sample preparation and it is necessary to use caution when comparing absolute quantities of water calculated in this type of sinter. The total water content of the vitreous sinter (> 7.9 ± 0.5 wt %) in sample NZ 592 is significantly higher than that of the patchy vitreous sinter (< 5.4 ± 0.8 wt %) (Table 3.1, Fig. 3.30A).

Most of the molecular water in this sample is in the form of type B molecular water (Fig. 3.31A). The vitreous sinter contains more type B molecular water than the other types of sinter in this sample. The silanol groups range from equivalent proportions of type A and type B silanol groups to type A silanol groups comprising most of the H_2O_{SiOH} (Fig. 3.32A). There is no trend with respect to the type of silanol groups (i.e. type A vs. type B silanol groups) contained in the different types of sinter. The dull indurated sinter has a higher amount of H_2O_{SiOH} (0.9 ± 0.1 wt %) compared to the vitreous in this sample (< 0.7 ± 0.1 wt %), whereas the vitreous sinter has a higher amount of H_2O_{mol} (9.2 ± 0.5 wt %) than the dull indurated sinter (< 6.5 ± 0.5 wt %) (Fig. 3.33A).

Table 3.1. Water contents of sinters as determined by EMP and FTIR analyses of different types of sinter; porous friable (PF), porous indurated (PI), dull indurated, (DI), patchy vitreous (PV), vitreous (vit), and spicules (sp) from New Zealand. Number subscripts denote different laminae of the same type of sinter within a sample. EMP spot analyses of BSEI indicated by dark (dark opal, BSEI), light (light opal, BSEI), and random (BSEI, homogeneous; random spot analyses taken). Total water content adjusted according to quartz standards due to EMP drift; indicated by *.

				EMP							FTIR					
Location	Sample	Mineralogy	Type of Sinter	BSEI	N	wt% Si	wt% O	mol H_2O	Wt% H_2O_{Total}	Wt% H_2O_{avg}	d (μm)	$Ã_{5200}$	Wt% H_2O_{mol}	$Ã_{4500}$	Wt% H_2O_{SiOH}	Wt% H_2O_{Total}
Waikite Geyser complex	NZ 592	opal-A	sp_1	random	26	41.0	54.6	0.34	**7.9** ±0.5*							
			sp_3	dark	10	40.7	58.0	0.50	**12.1** ±0.6*	10.3	260	72.88	9.2	3.53	0.7	**9.9**
				light	7	41.7	55.9	0.35	**8.5** ±1.2*							
			PI_1	random	35	42.0	51.7	0.16	**4.7** ±0.8		260	69.85	8.7	3.20	0.7	**9.4**
			PI_2	random	15	41.9	51.8	0.17	**4.9** ±0.9		350	70.34	6.5	2.49	0.4	**6.9**
			PV_1	random	33	42.1	52.5	0.19	**5.4** ±0.8		-	-	-	-	-	-
			PV_2	random	12	42.2	51.2	0.13	**3.7** ±0.7		-	-	-	-	-	-
			DI	random	16	42.3	54.1	0.25	**6.9** ±1.0		240	47.46	6.5	4.45	0.9	**7.4**
			vit_1	dark	5	40.4	56.5	0.46	**12.1** ±0.7		-	-	-	-	-	-
				light	7	42.2	53.3	0.22	**6.2** ±0.9							
			vit_2	dark	6	40.1	54.8	0.40	**10.7** ±0.8	9.1	285	85.29	9.8	1.88	0.4	**10.3**
				light	10	42.3	54.7	0.27	**7.4** ±0.8							
	NZ 603	opal-A	PF	light	105	45.7	55.8	0.14	**2.1** ±0.4*		300	8.50	1.0	3.11	0.5	**1.5**
				dark	70	39.3	57.4	-	-							
			PV	random	4	45.6	56.2	0.16	**2.6** ±0.5*		300	10.78	1.2	6.54	1.1	**2.3**
	NZ 601	opal-A	PI_1	random	45	43.2	56.0	0.40	**7.6** ±0.6		285	57.97	6.7	5.22	0.9	**7.6**
			PI_2	random	44	42.2	55.8	0.32	**8.7** ±0.4		300	62.95	6.8	4.38	0.8	**7.6**
			PI_3	random	43	42.0	55.3	0.31	**8.5** ±0.8		310	62.95	7.3	4.38	0.8	**8.1**
			PF	random	32	43.2	56.7	0.30	**5.4** ±0.5*		285	28.68	3.3	6.89	1.2	**4.5**
			vit_{white}	random	20	41.5	55.3	0.34	**8.0** ±0.6*		285	65.17	7.4	4.24	0.8	**8.2**
			vit_{grey}	random	30	41.7	55.0	0.32	**7.5** ±0.4*		285	54.25	6.2	6.30	1.2	**7.4**
Geyser Flat	NZ 816	opal-CT	PV	dark	30	43.9	53.3	0.13	**3.8** ±0.7		-	-	-	-	-	-
				light	47	45.7	53.0	0.04	**1.1** ±0.7							
			PI	dark	39	44.2	53.8	0.14	**4.0** ±0.6	3.5	260	29.90	3.8	0.04	0.01	**3.8**
				light	9	45.8	53.2	0.04	**1.2** ±0.7							
			DI_1	random	27	43.9	52.1	0.08	**2.5** ±0.9		-	-	-	-	-	-
			DI_2	random	13	40.7	51.4	0.22	**6.1** ±1.1		485	75.60	5.1	0.35	0.04	**5.1**
			vit_1	random	7	43.4	54.2	0.19	**5.5** ±0.7		485	75.22	5.1	0.08	0.01	**5.1**
			vit_2	random	10	44.5	53.7	0.12	**3.4** ±0.6		-	-	-	-	-	-
			vit_3	dark	32	43.4	52.9	0.14	**4.0** ±0.9		-	-	-	-	-	-
				light	35	44.9	52.9	0.07	**2.0** ±0.7							
			vit_4	random	34	42.7	53.0	0.18	**5.1** ±0.8		485	78.69	5.3	0.13	0.01	**5.3**

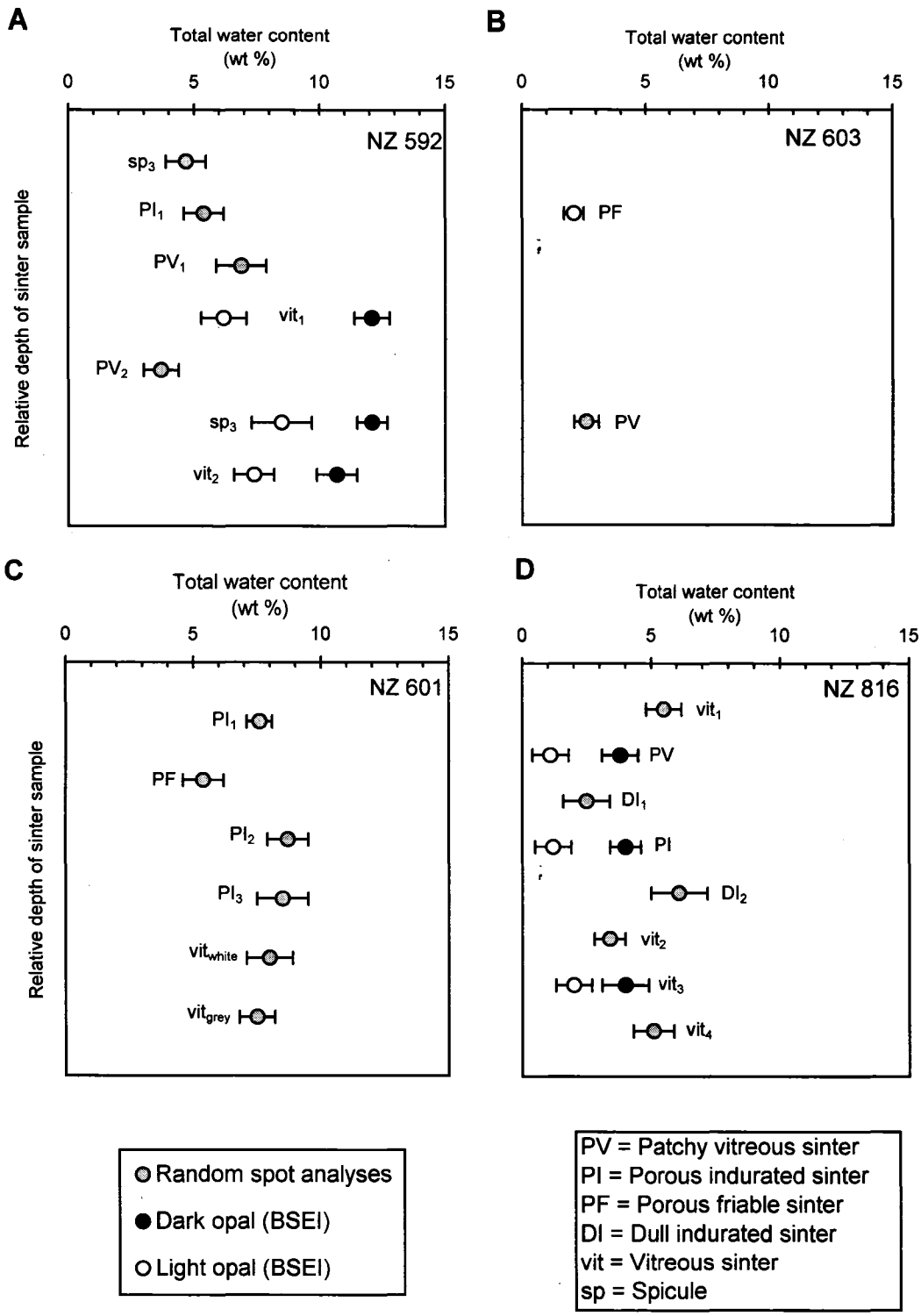

Figure 3.30. Mean total water content (wt %) of different types of sinter from New Zealand calculated using EMP analysis. Subscripts indicate different laminae of the same type of sinter in a deposit. Error bars are based on propogation of standard error of the mean.

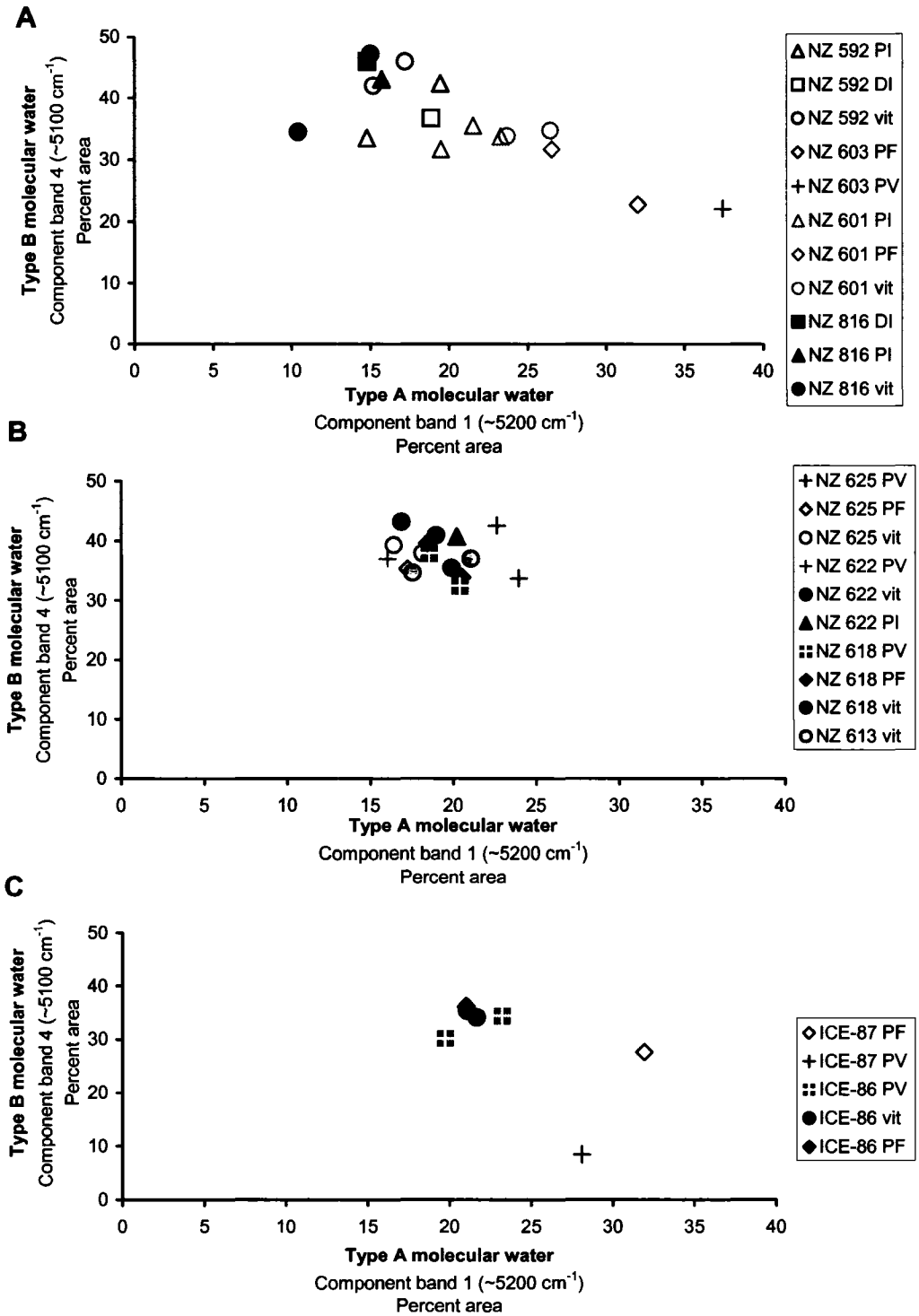

Figure. 3.31. Distribution of type A and type B molecular water. Colour filled symbols indicate sinter composed of opal-CT and blank symbols indicate sinter composed of opal-A. **A)** Sinter from Waikite Geyser and Geyser Flat, New Zealand. **B)** Sinter from Te Anarata, New Zealand. **C)** Sinter from Geysir, Iceland. PV = patchy vitreous sinter, PF = porous friable sinter, PI = porous indurated sinter, DI = dull indurated sinter, vit = vitreous sinter.

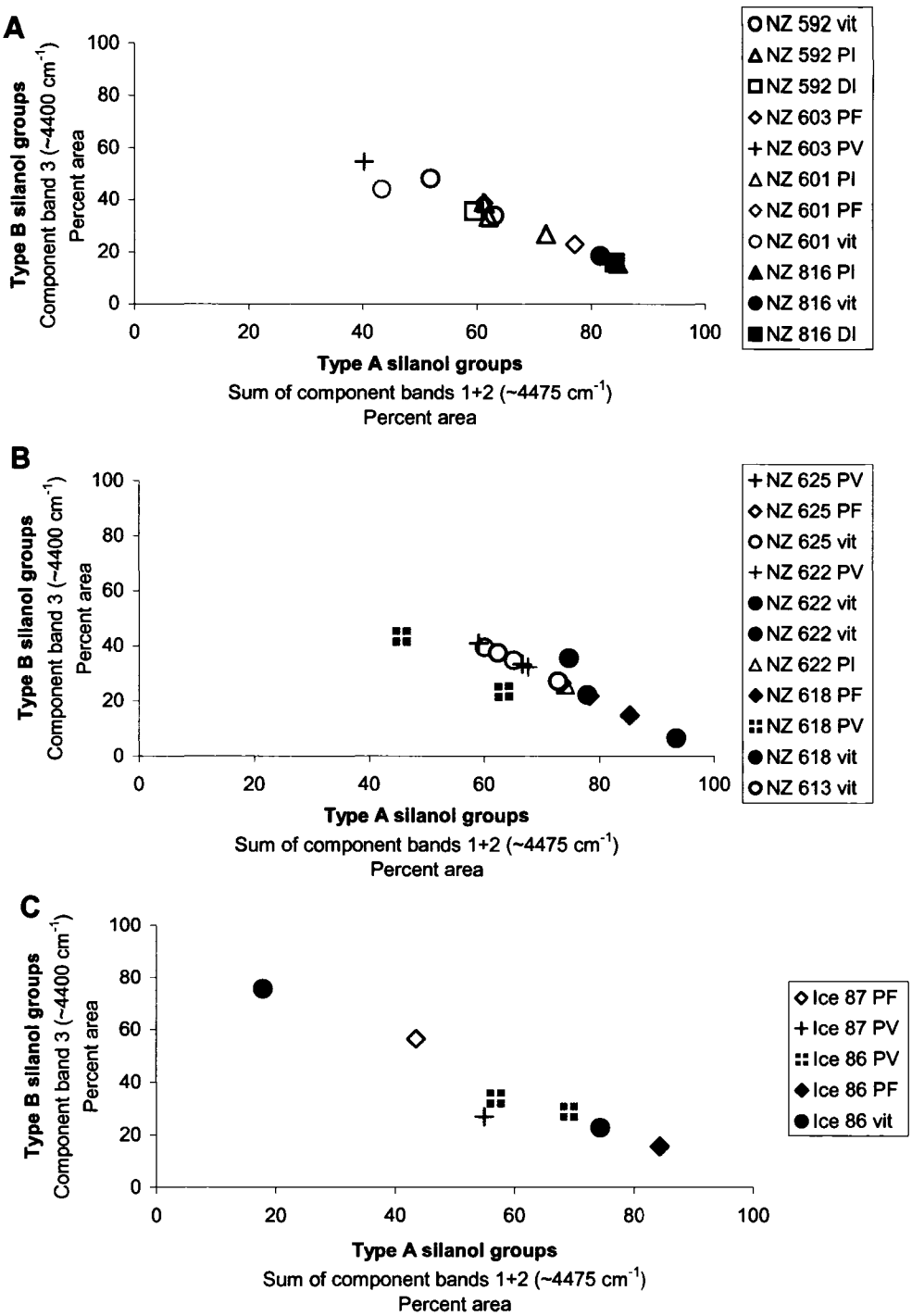

Figure 3.32. Distribution of type A and type B silanol groups. Colour filled symbols indicate sinter composed of opal-CT and blank symbols indicate sinter composed of opal-A. **A)** Sinter from Waikite Geyser complex, New Zealand. **B)** Sinter from Te Anarata, New Zealand. **C)** Sinter from Geysir, Iceland. PV = patchy vitreous sinter, PF = porous friable sinter, PI = porous indurated sinter, DI = dull indurated sinter, vit = vitreous sinter.

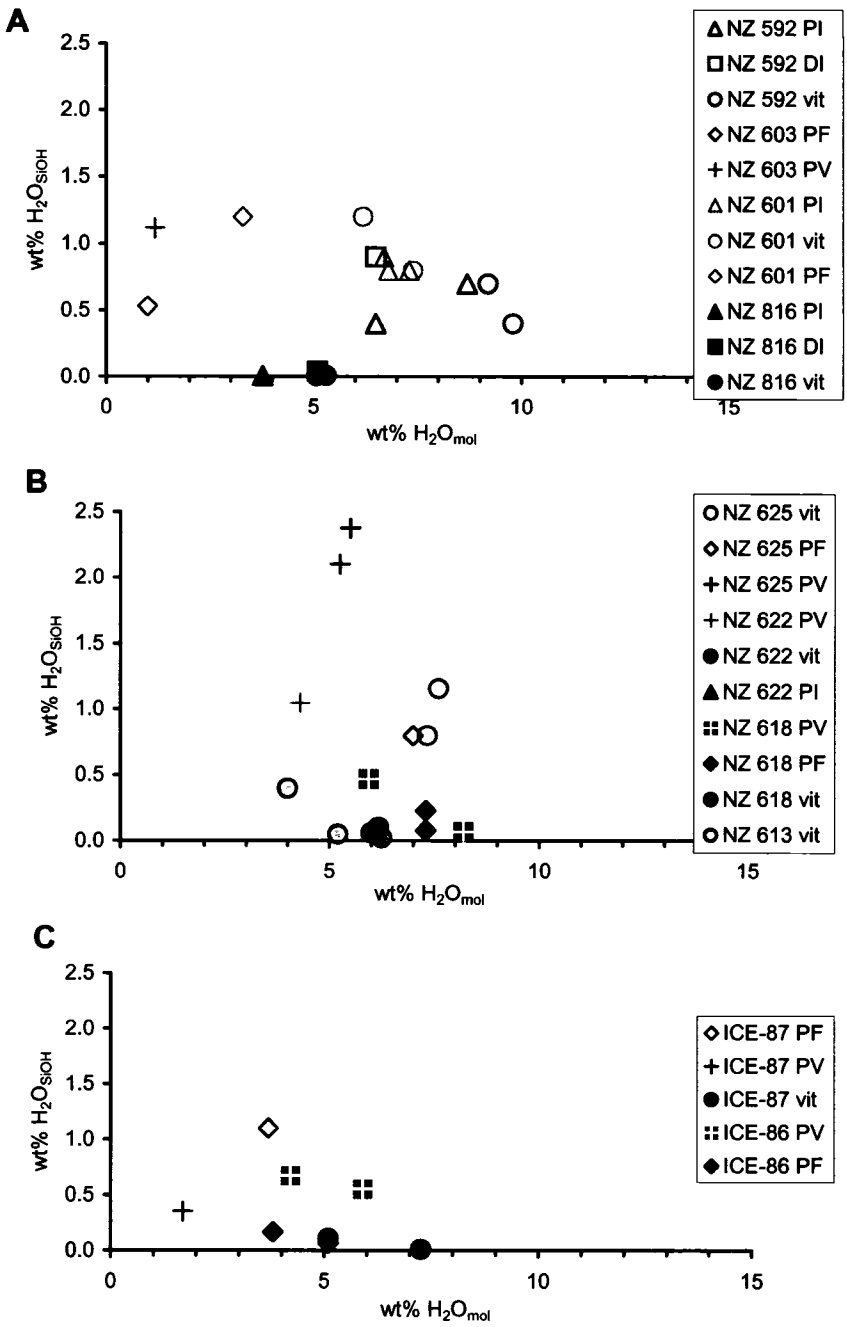

Figure 3.33. Concentrations of molecular (H_2O_{mol}) and silanol group (H_2O_{SiOH}) water. Colour filled symbols indicate sinter composed of opal-CT and blank symbols indicate sinter composed of opal-A. **A)** Sinter from Waikite Geyser complex and Geyser Flat, New Zealand. **B)** Sinter from Te Anarata, New Zealand. C) Sinter from Geysir, Iceland. PV = patchy vitreous sinter, PF = porous friable sinter, PI = porous indurated sinter, DI = dull indurated sinter, vit = vitreous sinter.

NZ 603

Sample NZ 603 (opal-A), located between two vents, is formed of alternating laminae of patchy vitreous and porous friable sinter. The porous friable sinter in this sample is formed of irregular intermeshed patches of dark and light grey opal (BSEI) (Fig. 3.34). The dark opal (BSEI) contains 1-7 wt % Al and could not be used to calculate total water content (Fig. 3.34B). The light grey opal (BSEI) does not contain significant amounts of elements other than Si and O, and was used to determine total water content for the porous friable sinter (2.1 ± 0.4 wt %).

The patchy vitreous sinter appears homogeneous in grey shades on BSEI. Finding suitable points (> 90 total wt %) for EMP analysis in the patchy vitreous sinter was difficult due to its extremely porous nature (Fig. 3.34A), thus few points could be used to determine its total water content (2.6 ± 0.5 wt %). The total water content of the patchy vitreous and porous friable sinter is essentially the same (2.6 ± 0.5 wt % vs. 2.1 ± 0.4 wt %) (Table 3.1, Fig. 3.30B). Total water contents obtained using EMP analyses are within the limits of analytical error of the total water contents determined using FTIR analyses (e.g. 2.1 ± 0.4 wt % vs. 1.5 ± 0.7 wt %; EMP vs. FTIR, respectively) (Table 3.1).

The molecular water in both types of sinter in this sample is mostly type A molecular water (Fig. 3.31A). The porous friable sinter has more type A silanol groups compared to the patchy vitreous sinter (Fig. 3.32A). The proportion of H_2O_{mol} to H_2O_{SiOH} is roughly equivalent in both types of sinter; patchy vitreous sinter has 1.2 ± 0.5 wt % H_2O_{mol} and 1.1 ± 0.1 wt % H_2O_{SiOH}, and porous friable sinter has 1.0 ± 0.5 wt % H_2O_{mol} and 0.5 ± 0.1 wt % H_2O_{SiOH} (Fig. 3.33A).

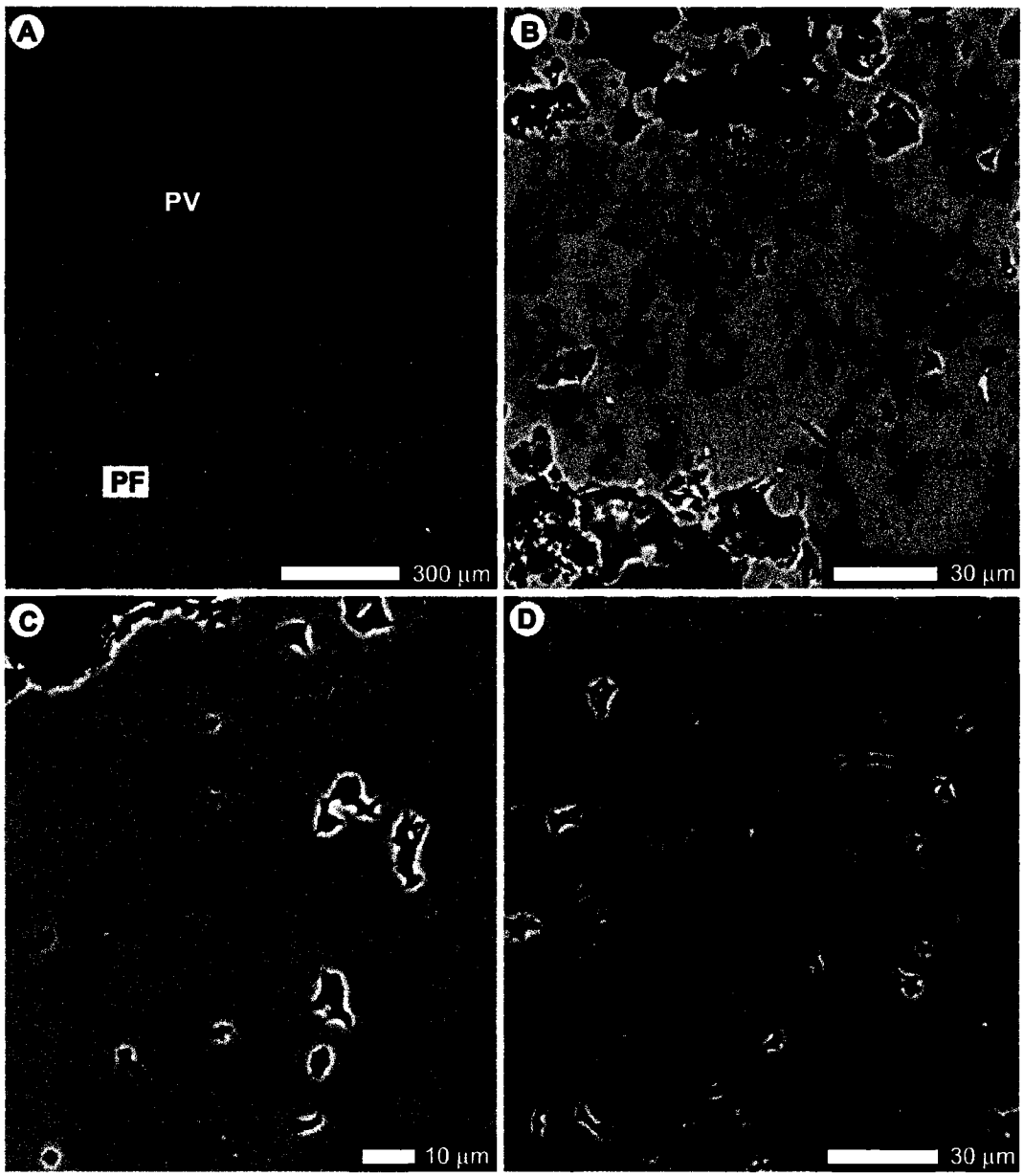

Figure 3.34. Backscattered electron images of sample NZ 603 from the Waikite Geyser complex. **A)** Patchy vitreous (PV) and porous friable (PF) sinter. **B)** Close up of PF sinter. Numbers indicate wt % Al of dark and light opal (BSEI). Due to high Al content, the dark opal (BSEI) could not be used to determine the total water content. Total water content determined using light opal (BSEI) is 2.1 wt %. **C)** Dark and light opal (BSEI) in PF sinter. Dark opal (BSEI) has Al content > 1 wt %, light opal (BSEI) has Al content < 1 wt %. **D)** Intricate patterns of dark and light opal (BSEI) in PF sinter. Dark opal (BSEI) has Al content > 1 wt %, light opal (BSEI) has Al content < 1 wt %.

NZ 601

Sample NZ 601 (opal-A), the most distal sample from the main vent, is composed of porous indurated, porous friable, and white and grey vitreous sinter. Respectively, the porous and non porous (BSEI) laminations correspond to the opaque and translucent laminations seen in thin section (Fig. 3.35A, B). No variations in average atomic weight were evident on BSEI in any of the sinter types in sample NZ 601 (Fig. 3.35C). The porous friable sinter in this sample has a significantly lower total water content (5.4 ± 0.1 wt %) compared to the other types of sinter in this sample (7.5 to 8.7 ± 0.4 wt %) (Table 3.1, Fig. 3.30C). There is no significant difference in the total water contents obtained using EMP analyses compared to those obtained with FTIR analyses in this sample (e.g. 5.4 ± 0.5 wt % vs. 4.5 ± 0.7 wt %; EMP vs. FTIR, respectively) (Table 3.1).

The molecular water in all types of sinter in this sample is comprised mainly of type B molecular water (Fig. 3.31A). The type of silanol groups range from equivalent proportions of type A and type B silanol groups to type A silanol groups being the dominant type of silanol (Fig. 3.32A). The porous friable sinter has a higher proportion of H_2O_{SiOH} to H_2O_{mol} (1.2 ± 0.1 wt % H_2O_{SiOH} and 3.3 ± 0.5 wt % H_2O_{mol}) compared to other types of sinter in this sample (0.8-1.2 ± 0.1 wt % H_2O_{SiOH} and 6.2-7.4 ± 0.1 wt % H_2O_{mol}) (Fig. 3.33A).

3.2.2 Geyser Flat, New Zealand

Sample NZ 816 (opal-CT) is formed of interlaminated dull indurated, vitreous, patchy vitreous and porous indurated sinter. Variations in average atomic weight are evident on BSEI in the patchy vitreous, porous indurated sinter and some laminae of

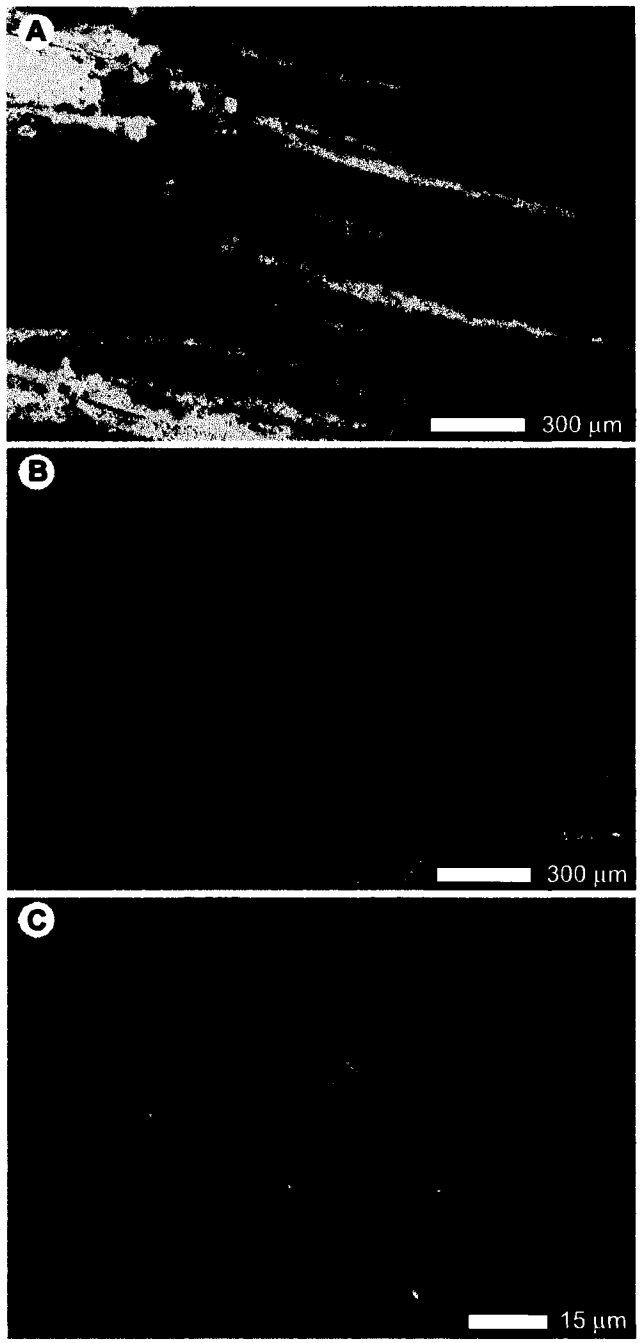

Figure 3.35. Sample NZ 601 from the Waikite Geyser complex on the distal discharge apron. **A)** Photomicrograph of vitreous sinter showing thin opaque and translucent laminations. **B)** Backscattered electron image (BSEI) of vitreous sinter in Fig. 3.35A, illustrating porous and nonporous laminations, which correspond respectively to the opaque and translucent laminations observed in thin section. **C)** Close up BSEI of porous and nonporous lamination. Opaque\porous laminations are composed of spheres with large void spacesand the translucent\nonporous laminations are composed of spheres with very little void space.

vitreous sinter of sample NZ 816 (Fig. 3.36). Light grey opal (BSEI) typically appears as angular to subrounded fragments surrounded by dark grey opal (BSEI) in the vitreous sinter (Fig. 3.36A, B). The porous indurated sinter is formed of irregular intergrown patches of dark and light grey opal (BSEI) (Fig. 3.36C). The dull indurated sinter appears homogeneous in grey shades on BSEI; however, intricate patterns of opal masses surrounded by opal cement are observed (Fig. 3.36D).

The dark grey opal (BSEI) has 4 wt % total water content, whereas the light grey opal (BSEI) contains 1-2 wt % total water (Table 3.1, Fig. 3.30D). The transparent vitreous rim around many of the large cavities and the dull indurated sinter located below the lamina of porous indurated sinter have the highest total water contents in this sample (5.5 ± 0.7 and 6.1 ± 1.1 wt %, respectively) (Fig. 3.30D). Compared to the sinter samples from Waikite Geyser, the sample from Geyser Flat generally has less type A molecular water, more type A silanol groups, and a significantly lower amount of H_2O_{SiOH} (Figs. 3.31A, 3.32A, 3.33A). The different types of sinter in sample NZ 816 contain variable amounts of type A and type B molecular water and silanol groups.

3.2.3 Te Anarata, New Zealand

NZ 625

Sample NZ 625 (opal-A), the youngest sample in the Te Anarata succession, is composed of patchy vitreous, porous friable, and laminated vitreous sinter. The patchy vitreous and porous friable sinter is formed of intergrown patterns of dark and light grey opal (BSEI) (Fig. 3.37A, C), whereas the laminated vitreous sinter appears homogeneous in grey shades (BSEI). In the porous friable sinter, the dark grey opal (BSEI) contains

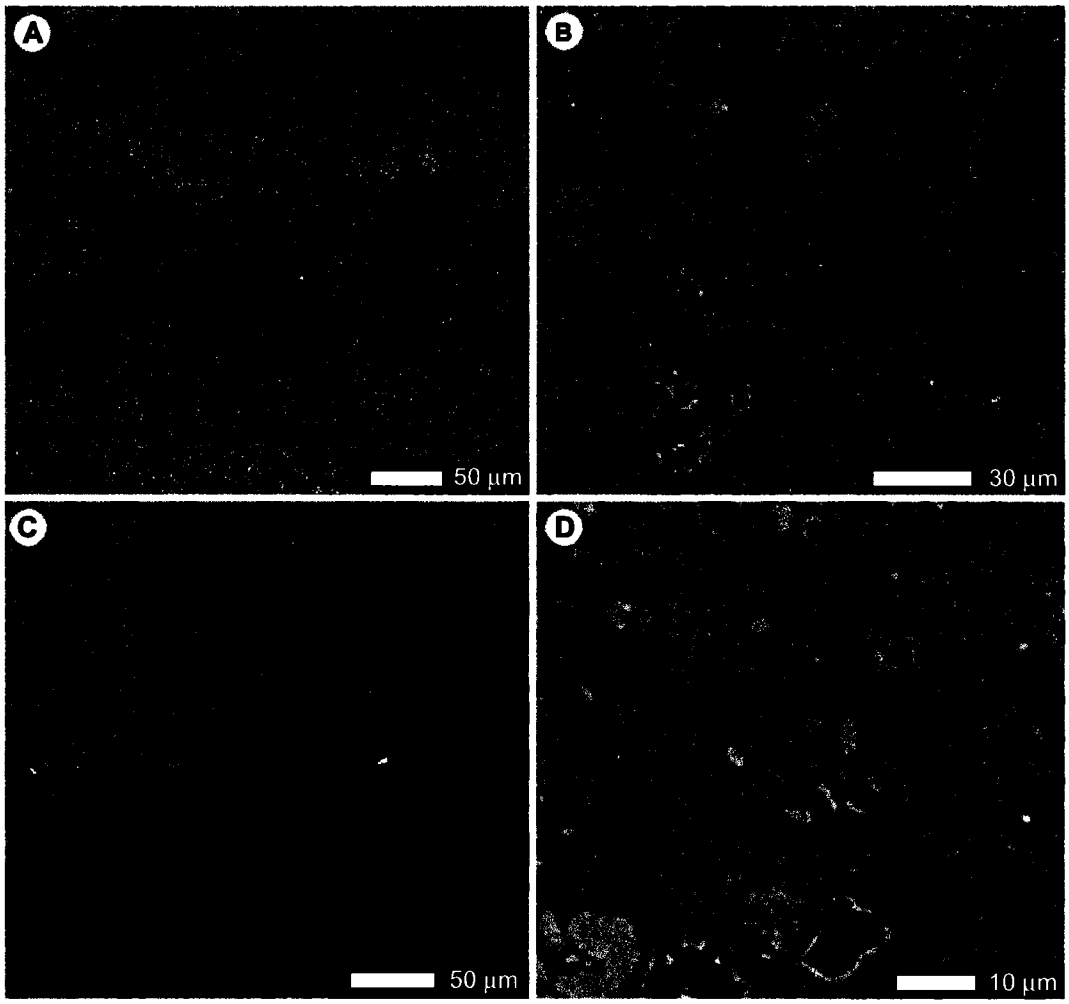

Figure 3.36. Backscattered electron images (BSEI) of sample NZ 816 from Geyser Flat. **A)** Vitreous sinter. Arrows indiate areas of light opal (BSEI). Electron microprobe analysis indidates light opal (BSEI) contains 2 wt % total water and dark opal (BSEI) contains 4 wt % total water. **B)** Angular to subrounded fragments in vitreous sinter. **C)** Intergrown patches of light and dark grey opal (BSEI) in porous indurated sinter. Light grey opal (BSEI) contains 1.2 wt % total water and dark grey opal (BSEI) contains 4 wt % total water. **D)** Dull indurated sinter displays intricate patterns but appears homogeneous in terms of average weight percent. Dark areas are areas of high porosity.

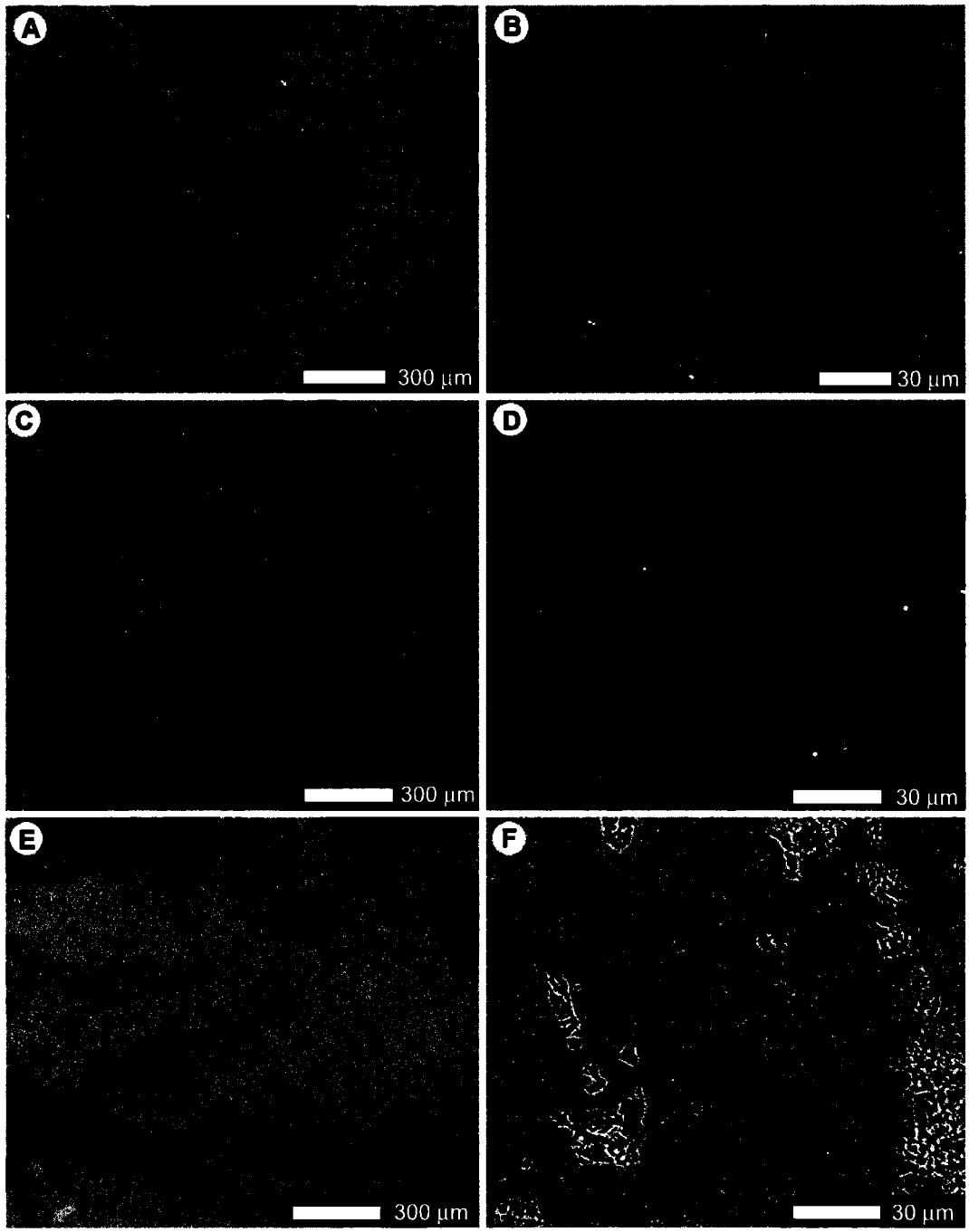

Figure 3.37. Backscattered electron images (BSEI) from Te Anarata, New Zealand. **A)** Sample NZ 625, from the top of the succession, porous friable (PF) sinter, composed of opal-A. **B)** Close up of Fig. 3.37A illustrating light and dark opal (BSEI) with 7.7 and 9.4 wt % total water, respectively. **C)** Sample NZ 618, from the lower part of the succession, PF sinter, composed of opal-CT. **D)** Close up of Fig. 3.37C illustrating light and dark opal (BSEI), with 7.0 and 9.2 wt % total water, respectively. **E)** Sample NZ 613, from the bottom of the succession, patchy vitreous sinter, composed of opal-CT. **F)** Close up of Fig. 3.37E illustrating light and dark opal (BSEI), with 1.0 and 5.1 wt % total water, respectively.

9.4 ± 0.8 wt % total water whereas light grey opal (BSEI) contains 7.7 ± 0.4 wt % total water (Table 3.2, Fig. 3.38A). Similarly, in the patchy vitreous sinter the dark grey opal (BSEI) has a higher total water content than the associated light grey opal (BSEI) (9.9 ± 0.6 wt % vs. 7.2 ± 0.7 wt %, respectively) (Table 3.2).

The fragments of vitreous sinter have a slightly higher total water content, 8.6 ± 0.7 wt % compared to 7.4 ± 0.5 wt % in the surrounding patchy vitreous sinter (Fig. 3.38A). The porous friable sinter has a lower total water content compared to the laminated vitreous sinter (7.6 ± 0.5 wt % vs. 9.1 ± 0.5 wt %). The molecular water in this sample is dominantly comprised of type B molecular water (Fig. 3.31B). The patchy vitreous sinter in this sample has more type A molecular water content than the porous friable and vitreous sinter. The sinters in this sample range in their proportions of type A to type B silanol groups; however, all are dominantly formed of type A silanol groups (Fig. 3.32B). The patchy vitreous sinter has roughly twice the amount of H_2O_{SiOH} (2.1-2.4 ± 0.1 wt %) as the porous friable and vitreous sinter (< 1.2 ± 0.1 wt %), and less H_2O_{mol} (5.5 ± 0.5 wt %) compared to the porous friable and vitreous sinter (> 7.0 ± 0.5 wt %) (Fig. 3.33B).

NZ 622

The upper portion of sample NZ 622 is composed of patchy vitreous, vitreous, and porous indurated sinter (opal-CT) and the lower portion is composed of patchy vitreous and porous friable sinter (opal-A). The vitreous sinter, composed of opal-CT, is the only type of sinter in this sample which displays variations in grey shades on BSEI (Table 3.2, Fig. 3.38B). The dark grey opal (BSEI) contains 6.4 ± 0.4 wt % total water, whereas the light grey opal (BSEI) contains 4.3 ± 0.5 wt % total water. The total water

Table 3.2. Water contents of sinters as determined by EMP and FTIR analyses of different types of sinter; porous friable (PF), porous indurated (PI), dull indurated, (DI), patchy vitreous (PV), vitreous (vit), and spicules (sp) from New Zealand. Number subscripts denote different laminae of the same type of sinter within a sample. EMP spot analyses of BSEI indicated by dark (dark opal, BSEI), light (light opal, BSEI), and random (BSEI, homogeneous; random spot analyses taken). Total water content adjusted according to quartz standards due to EMP drift; indicated by *.

				EMP							FTIR					
Location	Sample		Type of Sinter	BSEI	N	wt% Si	wt% O	mol	Wt% H_2O_{Total}	Wt% H_2O_{avg}	d (μm)	$Å_{5200}$	Wt% H_2O_{mol}	$Å_{4500}$	Wt% H_2O_{SiOH}	Wt% H_2O_{Total}
Te Anarata	NZ 625	opal-A	PV_{matrix}	random	39	43.1	55.6	0.27	**7.4** ±0.5		280	38.74	5.5	10.68	2.4	**7.9**
			$PV_{fragments}$	dark	35	42.0	56.6	0.37	**9.9** ±0.6	8.6	230	36.97	5.3	9.55	2.1	**7.4**
				light	26	43.8	56.4	0.26	**7.2** ±0.7							
			PF	dark	7	42.9	57.3	0.35	**9.4** ±0.8							
				light	8	44.6	57.8	0.28	**7.7** ±0.4	7.6	310	66.51	7.0	4.88	0.8	**7.8**
				random	36	44.0	56.8	0.27	**7.4** ±0.5							
			vit white	random	9	43.7	57.8	0.32	**8.8** ±1.0		310	69.58	7.3	4.50	0.8	**8.1**
			vit grey	random	63	43.7	58.1	0.33	**9.1** ±0.5		310	72.12	7.6	7.02	1.2	**8.8**
	NZ 622	opal-CT	PV_1	random	29	43.8	57.9	0.32	**7.5** ±0.3*		-	-	-	-	-	-
		opal-A	PV_2	random	46	43.8	56.8	0.27	**5.7** ±0.5*		-	-	-	-	-	-
		opal-A	PV_3	random	43	43.3	56.0	0.27	**5.0** ±0.5*		340	44.41	4.3	6.97	1.0	**5.3**
		opal-A	PV_4	random	27	43.0	56.1	0.29	**4.7** ±0.5*		-	-	-	-	-	-
		opal-CT	vit_1	dark	45	43.9	56.9	0.28	**6.4** ±0.4*	5.9	450	85.99	6.3	0.22	0.03	**6.3**
				light	13	44.7	56.0	0.20	**4.3** ±0.5*							
		opal-CT	vit_2	random	50	43.5	56.2	0.27	**6.0** ±0.4*		450	81.80	6.0	0.53	0.06	**6.0**
		opal-CT	PI	random	49	43.9	55.5	0.22	**4.7** ±0.3*		450	84.24	6.1	0.82	0.1	**6.2**
		opal-A	PF	random	47	43.2	56.1	0.28	**3.7** ±0.4*		-	-	-	-	-	-
	NZ 618	opal-CT	PV_1	dark	71	43.2	57.3	0.33	**8.9** ±0.4							
				light	11	44.3	57.0	0.26	**7.3** ±0.5	8.7	350	86.48	8.2	0.47	0.07	**8.2**
			PV_2	dark	22	43.6	55.7	0.24	**6.8** ±0.5							
				light	5	44.3	55.1	0.19	**5.3** ±1.0							
				random	15	43.8	54.9	0.20	**5.7** ±0.5	6.2	350	63.52	5.9	3.21	0.5	**6.4**
			vit	dark	11	43.7	56.3	0.26	**6.8** ±0.6*							
				light	3	44.3	54.4	0.16	**4.0** ±0.7*							
				random	37	43.9	56.0	0.24	**6.2** ±0.5*	6.2	350	66.36	6.2	0.51	0.1	**6.3**
			PF_1	dark	28	43.6	55.9	0.25	**7.1** ±0.5							
				light	18	44.2	55.7	0.21	**6.0** ±0.5	6.7	350	77.55	7.3	0.55	0.08	**7.3**
			PF_2	dark	10	43.1	57.5	0.34	**9.2** ±0.6							
				light	8	43.7	56.1	0.25	**7.0** ±0.7							
				random	23	43.5	55.9	0.26	**7.2** ±0.7	7.6	350	77.65	7.3	1.58	0.2	**7.5**
			PF_3	random	44	41.8	53.8	0.26	**7.3** ±2.5*		-	-	-	-	-	-

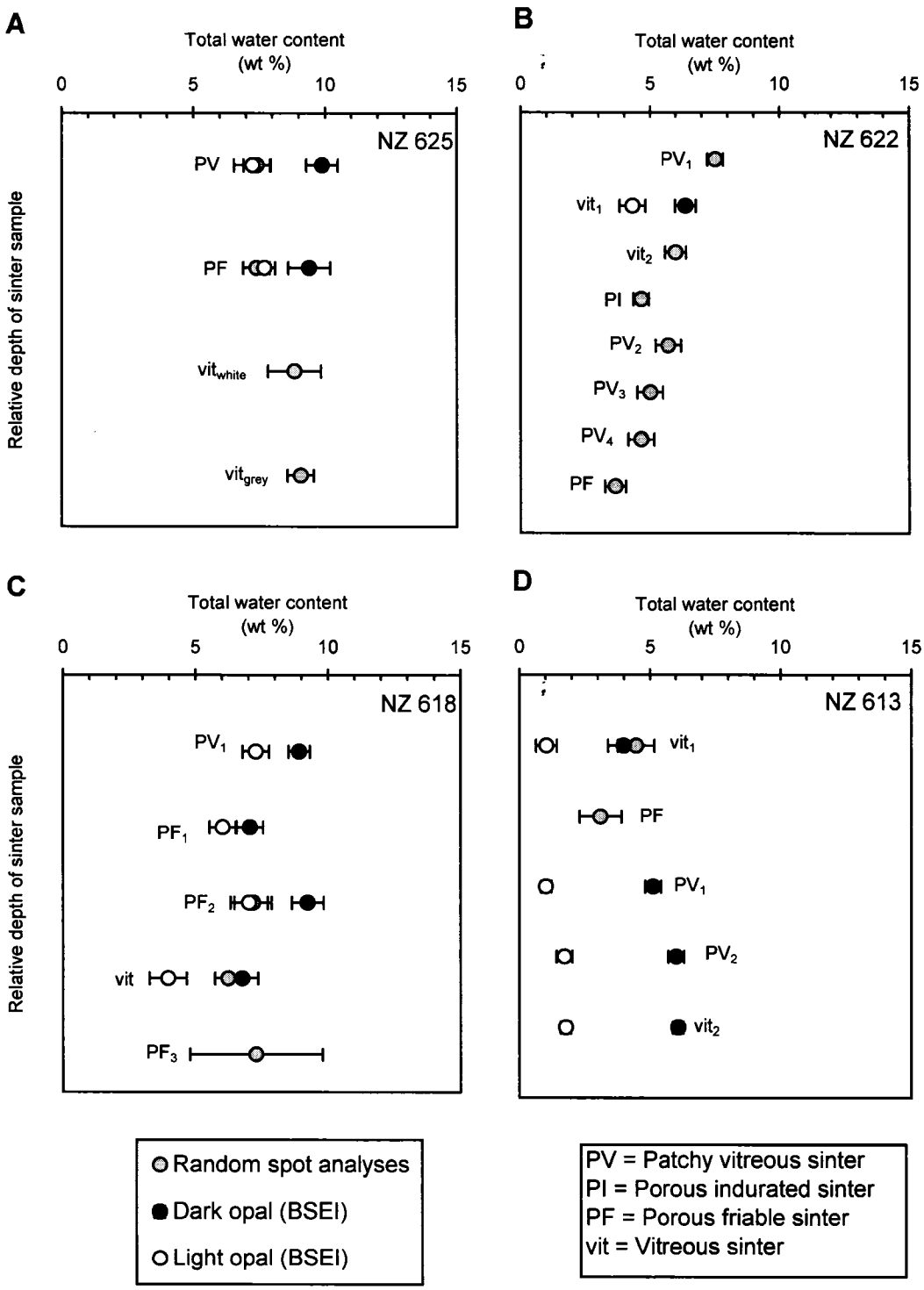

Figure 3.38. Mean total water content (wt %) of different types of sinter from the Te Anarata succession calculated using EMP analysis. Subscripts indicate different laminae of the same type of sinter in a deposit. Error bars are based on propogation of standard error of the mean.

content determined using EMP analysis is within experimental error of the total water content determined using FTIR analysis for all sinter in this sample except for the porous indurated sinter (4.7 ± 0.3 wt % vs. 6.2 ± 0.5 wt %, respectively) (Table 3.2).

The total water content in this sample gradually decreases with depth; the patchy vitreous sinter at the top of the sample has a significantly higher water content (7.5 ± 0.3 wt %) than the porous friable sinter at the bottom (3.7 ± 0.4 wt %) (Fig. 3.38B). Type B molecular water forms most of the H_2O_{mol} and type A silanol groups comprises most of H_2O_{SiOH} in this sample (Fig. 3.31B). The patchy vitreous sinter (opal-A) has a significantly higher amount of H_2O_{SiOH} compared to the vitreous (opal-CT) and porous indurated sinter (opal-CT) (1.0 ± 0.1 wt % vs. < 0.06 ± 0.1 wt %, respectively) (Fig. 3.32B). The patchy vitreous sinter (opal-A) has a lower amount of H_2O_{mol} compared to the vitreous and porous indurated sinter (4.3 ± 0.5 wt % vs. > 6.0 ± 0.5 wt %, respectively) (Fig. 3.33B).

NZ 618

Sample NZ 618 (opal-CT) is formed of interlaminated porous friable, patchy vitreous, and vitreous sinter. Most of the sinter in this sample is composed of opal with variations in grey shades on BSEI (Fig. 3.37C, D). The porous friable sinter has the smallest variation in total water content between dark and light grey opal (BSEI) (7.1 ± 0.5 wt % vs. 6.0 ± 0.5 wt %, respectively), whereas the vitreous sinter has the largest difference in total water content between dark and light grey opal (BSEI) (6.8 ± 0.6 wt % vs. 4.0 ± 0.7 wt %, respectively) (Table 3.2, Fig. 3.38C). The total water contents calculated using EMP methods are within the limits of analytical error of total water

content calculated using FTIR methods in this sample (e.g. 6.7 ± 0.5 wt % vs. 7.3 ± 0.7 wt %, respectively) (Table 3.2).

The sinter in this sample has a fairly narrow range in total water content; between 6.2 and 8.7 ± 0.7 wt % (Fig. 3.38C). Type B molecular water forms most of the H_2O_{mol} and type A silanol groups forms most of the H_2O_{SiOH} found in this sample (Fig. 3.31B). The patchy vitreous and vitreous sinter in this sample have a very high proportion of type A silanol groups compared to other types of sinter from Te Anarata (Fig. 3.32B). The sinter in this sample contains 6-8 ± 0.5 wt % H_2O_{mol} and less than 0.5 ± 0.1 wt % H_2O_{SiOH} (Fig. 3.33B).

NZ 613

Sample NZ 613 (opal-CT), the oldest sample in the Te Anarata sequence, is formed of porous friable, patchy vitreous, and vitreous sinter. Most of the sinter in this sample is composed of intergrown patches of dark and light grey opal (BSEI) (Fig. 3.37E). The vitreous sinter has a relatively small variation in total water content between dark and light grey opal (BSEI) (4.0 ± 0.6 wt % vs. 1.0 ± 0.4 wt %, respectively) compared to the patchy vitreous sinter, which has much larger difference (6.0 ± 0.6 wt % vs. 1.7 ± 0.3 wt %, dark and light opal (BSEI), respectively) (Table 3.3, Fig. 3.38D). This sample also has the lowest average total water content (< 4.4 ± 0.3 wt %) of the samples analysed from the Te Anarata sequence. Due to problems associated with sample preparation, only the vitreous sinter in this sample was analysed using FTIR. The laminae of vitreous sinter in this sample are formed mostly of type B molecular water and type A silanols (Figs. 3.31B, 3.32B). The laminae of vitreous sinter contain 4.0 and 5.2 ± 0.5 wt % H_2O_{mol}, and 0.05 and 0.4 ± 0.1 wt % H_2O_{SiOH} (Fig. 3.33B).

Table 3.3. Water contents of sinters as determined by EMP and FTIR analyses of different types of sinter; porous friable (PF), porous indurated (PI), dull indurated (DI), patchy vitreous (PV), vitreous (vit), and spicules (sp) from New Zealand and Iceland. Number subscripts denote different laminae of the same type of sinter within a sample. EMP spot analyses of BSEI indicated by dark (dark opal, BSEI), light (light opal, BSEI), and random (BSEI, homogeneous; random spot analyses taken). Total water content adjusted according to quartz standards due to EMP drift; indicated by *.

				EMP						FTIR					
Location	Sample		Type of Sinter	BSEI	N	wt% Si	wt% O	mol	Wt% H_2O_{Total}	Wt% H_2O_{avg}	d (μm)	$Å_{5200}$	Wt% H_2O_{mol}	$Å_{4500}$	Wt% H_2O_{SiOH}	Wt% H_2O_{Total}
Te Anarata	NZ 613	opal-CT	vit_1	dark	26	44.3	53.4	0.12	**4.0** ±0.6							
				light	14	46.0	52.8	0.01	**1.0** ±0.4*							
				random	14	44.0	53.5	0.13	**4.5** ±0.7*	3.3	450	54.41	4.0	3.67	0.4	**4.4**
			vit_2	dark	18	43.5	54.5	0.20	**6.1** ±0.2*							
				light	12	46.0	53.6	0.04	**1.8** ±0.2*	4.4	450	70.61	5.2	0.45	0.05	**5.2**
			PF	random	27	44.4	53.1	0.10	**3.1** ±0.8*		-	-	-	-	-	-
			PV_1	dark	33	44.0	54.2	0.16	**5.1** ±0.3*							
				light	27	46.3	53.3	0.02	**1.0** ±0.2*	3.3	-	-	-	-	-	-
			PV_2	dark	19	43.7	54.4	0.18	**6.0** ±0.3*							
				light	11	46.1	53.4	0.03	**1.7** ±0.3*	4.4	-	-	-	-	-	-
Geysir, Iceland	Ice-87	opal-A	PF	random	3	40.8	54.1	0.32	**7.9** ±1.1*		300	29.11	3.7	5.52	1.1	**4.8**
			PV	random	15	43.2	57.2	0.32	**7.9** ±0.8*		300	13.10	1.7	2.08	0.4	**2.1**
	Ice-86	opal-CT	PV_1	random	73	41.6	53.4	0.25	**7.0** ±0.5		340	61.39	5.9	3.69	0.6	**6.5**
			PV_2	random	47	43.3	54.1	0.19	**5.5** ±0.5		340	43.85	4.2	4.48	0.7	**4.9**
			vit_1	dark	3	42.1	55.1	0.30	**8.2** ±0.6							
				light	9	44.0	54.8	0.19	**5.3** ±0.5							
				random	59	43.5	55.0	0.22	**6.1** ±0.4	6.1	340	75.42	7.3	0.08	0.01	**7.3**
			vit_2	random	33	44.1	54.1	0.16	**4.5** ±0.5		490	76.22	5.1	1.03	0.1	**5.2**
			PF_1	random	57	43.5	53.5	0.16	**4.5** ±0.6		490	77.30	5.1	0.64	0.1	**5.2**
			PF_2	random	56	44.3	54.5	0.16	**4.6** ±0.5		490	57.83	3.8	1.63	0.2	**4.0**

3.2.4 Geysir, Iceland

ICE-87

Sample ICE-87 (opal-A) is formed of interlaminated porous friable and patchy vitreous sinter. Backscattered electron images of sample ICE-87 are homogeneous in grey shades, indicating there is little spatial variation in average atomic weight. Most of the patchy vitreous and porous friable sinters in sample ICE-87 contain 1-12 wt % Al. The total water content could only be calculated from a few of the EMP spot analyses and caution must be used in the comparison of the total water content for the patchy vitreous (7.9 ± 0.8 wt %) and porous friable sinter (7.9 ± 1.1 wt %) of this sample (Table 3.3, Fig. 3.39A).

The total water content obtained using EMP analysis is significantly higher than the total water contents determined using FTIR analyses for both the patchy vitreous (7.9 ± 0.8 wt % vs. 2.1 ± 0.7 wt %) and porous friable sinter (7.9 ± 1.1 wt % vs. 4.8 ± 0.7 wt %) (Table 3.3). High Al contents (> 1 wt %) may have interfered in the determination of water content using FTIR analysis because Al-OH groups are absorbed in the same region of the spectrum as silanol groups (4500 cm^{-1}) (Stolper 1982; Silver and Stolper 1989).

Despite the uncertainty in the absolute quantitative results obtained for this sample, some general trends in the type of water present are still evident. The patchy vitreous and porous friable sinter in sample ICE-87 have equivalent ratios of type A to type B molecular water, with type B molecular water content roughly twice that of type A molecular water (Fig. 3.31C). The porous friable sinter in this sample has a significantly higher proportion of type B silanol groups compared to the patchy vitreous sinter (Fig.

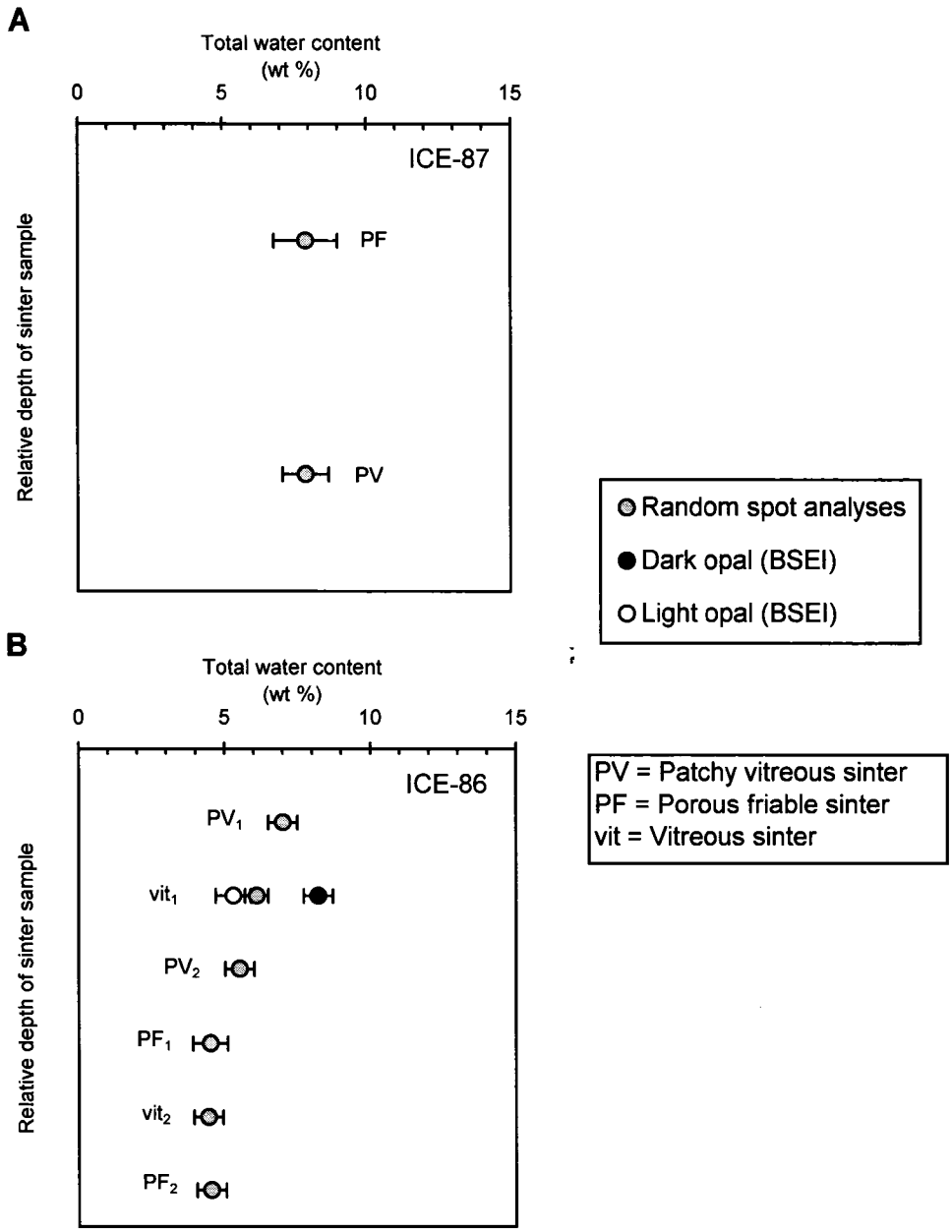

Figure 3.39. Mean total water content (wt %) of different types of sinter from the Geysir succession calculated using EMP analysis. Subscripts indicate different laminae of the same type of sinter in a deposit. Error bars are based on propogation of standard error of the mean.

3.32C). The porous friable sinter in sample ICE 87 has higher amounts of both H_2O_{mol} (3.7 ± 0.5 wt %) and H_2O_{SiOH} (1.1 ± 0.1 wt %) compared to the patchy vitreous sinter; H_2O_{mol} (1.7 ± 0.5 wt %) and H_2O_{SiOH} (0.4 ± 0.1 wt %) (Fig. 3.33C).

ICE-86

Sample ICE-86 (opal-CT) is formed of laminated patchy vitreous, porous friable, and vitreous sinter. This sample is formed almost entirely of Si and O; other elements (Al, Ca, Mg etc.) constitute less than 1 wt %. The total water contents obtained using EMP and FTIR are within the limits of analytical error for all types of sinter in this sample (e.g. 6.1 ± 0.4 wt % vs. 7.3 ± 0.7 wt %; EMP vs. FTIR, respectively) (Table 3.3).

In sample ICE-86, the total water content decreases with depth in the sample from 7.0 to 4.5 wt % (Fig. 3.39B). The upper laminae of patchy vitreous sinter contains 7.0 and 5.5 ± 0.5 wt % total water (Fig. 3.39B). A lamina of vitreous sinter containing 6.1 ± 0.4 wt % total water separates the patchy vitreous sinter and is the only type of sinter in this sample that displays variations in grey shades on BSEI (Fig. 3.39B). The dark grey opal (BSEI) has 8.2 ± 0.6 wt % total water, whereas the light grey opal (BSEI) has 5.3 ± 0.5 wt % total water. The laminae of porous friable sinter and the lower laminae of vitreous sinter all contain 4.5 ± 0.6 wt % total water (Fig. 3.39B).

All of the different types of sinter in sample ICE-86 have the roughly same ratio of type A to type B molecular water, with type B molecular water constituting most of the molecular water content (Fig. 3.31C). This sample has much less type A molecular water than sample ICE-87. Generally type A silanol groups constitute most of the silanol content (Fig. 3.32C). The laminae of patchy vitreous sinter in this sample have a

relatively high amount of H_2O_{SiOH} (0.7 ± 0.1 wt %) compared to the vitreous and porous friable sinter (< 0.2 ± 0.1 wt %) (Fig. 3.33C).

3.2.5 Water Content Synopsis: Opal-A vs. Opal-CT

Siliceous sinter composed of opal-A generally has higher total water contents than sinters composed of opal-CT; however, there is overlap in total water contents between opal-A and opal-CT. Sinter composed of opal-A generally contains 6-9 wt % total water but may contain as little as 2 wt % total water (light grey opal (BSEI), NZ 603) and as much as 12 wt % total water (dark grey opal (BSEI), NZ 592) (Table 3.1-3.3). Sinter composed of opal-CT generally contains 3-6 wt % total water but may contain as much as 9 wt % total water (dark grey opal (BSEI), NZ 618) and as little as 1 wt % total water (light grey opal (BSEI), NZ 613) (Table 3.1-3.3). Microscale variations in total water content are evident in both opal-A and opal-CT on BSEI (e.g. Fig. 3.29, 3.37).

Opal-CT deposits generally have a larger range in their minimum and maximum total water contents than opal-A deposits. For example, sample NZ 625, composed of opal-A, contains 7.2 wt % total water in the light opal (BSEI) in the patchy vitreous sinter and 9.4 wt % total water in dark opal (BSEI) in the porous friable sinter, a difference of 2.2 wt % total water (Fig. 3.38A). Sample NZ 613, composed of opal-CT, has a difference of 5.0 wt % total water between the light and dark opal (BSEI) in the vitreous sinter (Fig 3.38D).

Results indicate that siliceous sinter composed of opal-A generally has a higher proportion of type A molecular water, whereas opal-CT has a higher proportion of type B molecular water; as illustrated by the variations between opal-A and opal-CT in the

molecular water absorption spectra (Fig. 2.8). Variations in the absorption spectra between opal-A and opal-CT are highlighted in the average component band center, FWHM, and percent areas of the four component bands used to fit the molecular water band (Fig. 3.40). The average center position of all four of the molecular water component bands of opal-A are at a higher energy compared to opal-CT (Fig. 3.40A). Significant differences in the FWHM occur in component bands 1 and 4 between opal-A and opal-CT, whereas the FWHM of the other component bands (2 and 3) is essentially the same for opal-A as it is for opal-CT (Fig. 3.40B). Likewise, significant differences occur in the percent area of component bands 1 and 4 between opal-A and opal-CT, whereas component bands 2 and 3 show no significant difference between opal-A and opal-CT (Fig. 3.40C). Thus, due to the significant differences observed between opal-A and opal-CT in component bands 1 and 4, the qualitative assessment of type A and type B molecular water using these two component bands is realistically equivalent to the high and low energy bands described by Langer and Flörke (1974).

Siliceous sinter composed of opal-A has relatively more type B silanol groups, compared to opal-CT, which has more type A silanol groups (Figs. 2.9, 3.41). The variations in silanol groups between opal-A and opal-CT are highlighted by differences in the average component band center, FWHM, and percent areas of the three component bands used to fit the silanol group band (Fig. 3.41). The average center position of component band 3 (low energy) is located at a lower energy in sinter composed of opal-A compared to sinter composed of opal-CT, whereas there is no significant difference between opal-A and opal-CT in the average center position of component bands 1 and 2 (Fig. 3.41A). The FWHM for all 3 component bands is higher in sinter composed of

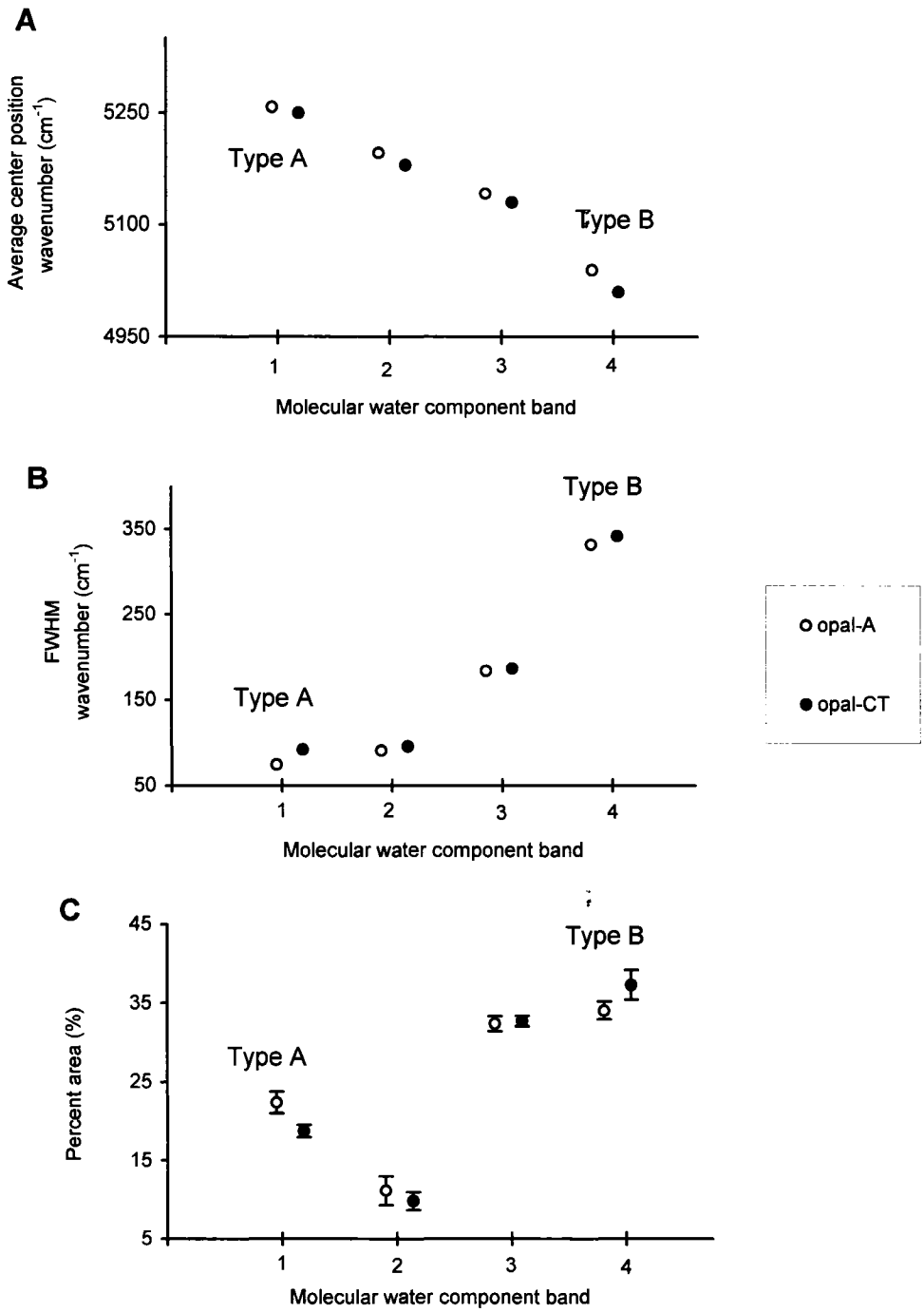

Figure 3.40. Comparative analysis of molecular water spectra; opal-A vs. opal-CT. Component bands (1-4) fit using PeakFit © program. Component band 1 represents type A molecular water. Component band 4 represents type B molecular water. Error bars are estimates based on the standard error of the mean, see text for details.

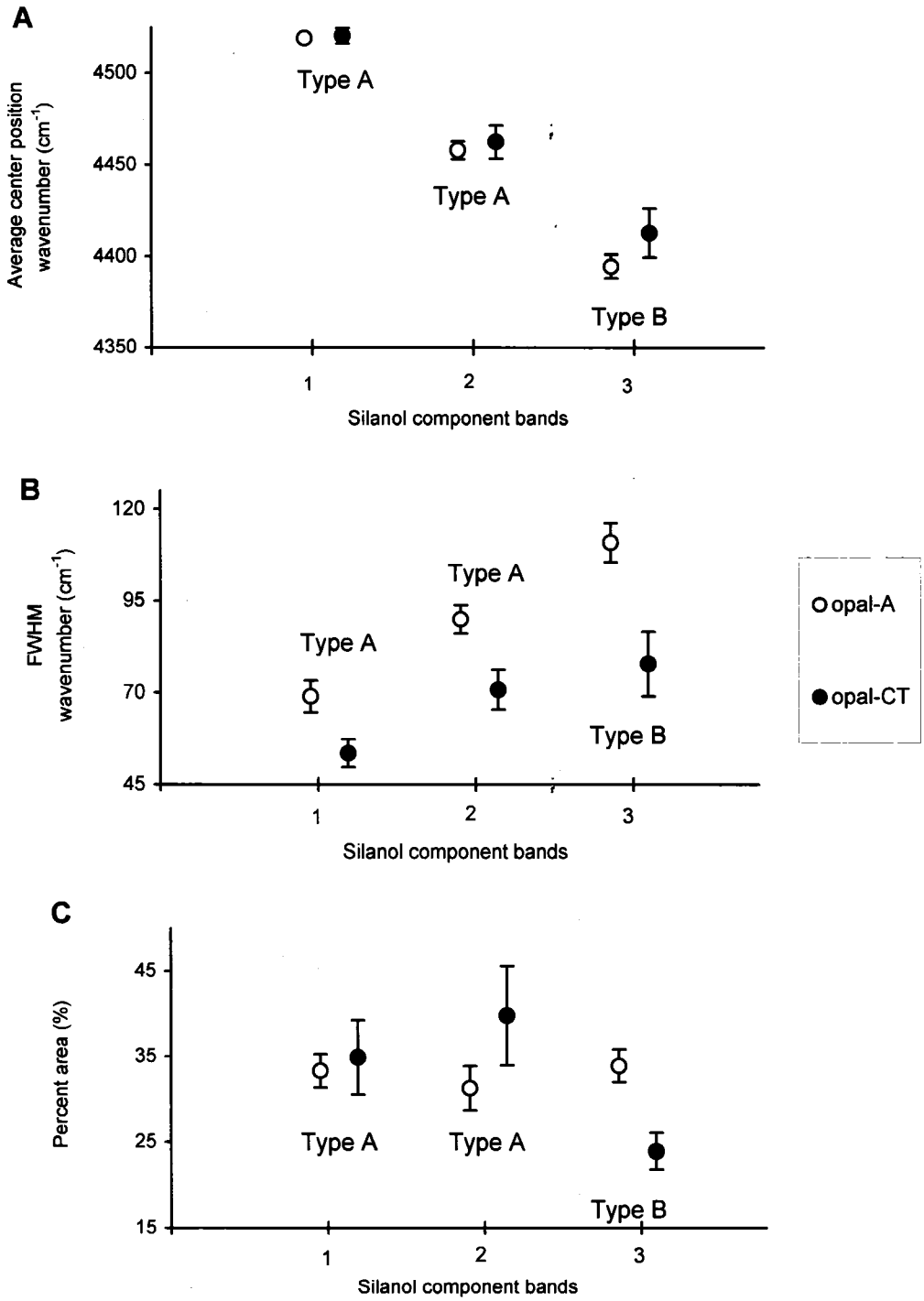

Figure 3.41. Comparative analysis of silanol group spectra; opal-A vs. opal-CT. Component bands (1-3) fit using PeakFit © program. The sum of component bands 1 + 2 represents type A silanol groups. Component band 3 represents type B silanol groups. Error bars are estimates based on standard error of the mean, see text for details.

opal-A compared to opal-CT (Fig. 3.41B). In sinter composed of opal-A, component band 3 has a significantly higher percent area than sinter composed of opal-CT (Fig. 3.41C). The percent areas of both component band 1 and 2 is generally higher in opal-CT than in opal-A (Fig. 3.41C). Respectively, component band 3, and component bands 1 and 2 are thus equivalent to the low and high energy bands used by Langer and Flörke (1974).

Most of the total water content in opal-A and opal-CT is in the form of molecular water (H_2O_{mol}) rather than silanols (H_2O_{SiOH}) (Fig. 3.33). Results show that sinter composed of opal-A generally has higher H_2O_{SiOH} contents than sinter composed of opal-CT (0.5-1 wt % vs. 0.05-0.4 wt %, respectively). As with the total water content there is a degree of overlap in H_2O_{SiOH} contents between opal-A and opal-CT; for example H_2O_{SiOH} contents may be as high as 0.7 wt % in some opal-CT deposits (ICE-86). There is considerably more overlap in H_2O_{mol} contents between opal-A and opal-CT, as sinter composed of opal-A generally contains 6-10 wt % H_2O_{mol} and opal-CT generally contains 4-7 wt % H_2O_{mol} (Fig. 3.33).

Chapter Four – Discussion

The conversion from opal-A to opal-CT is generally thought to take place through a dissolution-reprecipitation pathway (e.g., White et al. 1956; Carr and Fyfe 1958; Williams et al. 1985; Rice et al. 1995; Lynne and Campbell 2004; Rodgers et al. 2004). Landmesser (1998)'s "mobility by metastability" theory is based on the different solubilities of solid silica; the range of solubilities allow different concentrations (or chemical potentials) to develop in the pore solution network. Less mature silica solids (e.g. opal-A), which have a relatively high solubility, dissolve, diffuse, then precipitate in areas with more mature silica solids (e.g. opal-CT), where there is a lower solubility. Essentially all that is required is that metastable silica states exist over time and that active sources and sinks are connected by aqueous films (Rodgers et al. 2004). The opal-A to quartz transformation is thought to take place over a period of 30,000 to 40,000 years in siliceous sinters in the New Zealand hot spring systems (Herdianita et al. 2000b). Although the diagenetic mechanisms are poorly understood, time and/or high temperatures, pressures, excess organic matter, the presence of other minerals, and post-depositional alteration by steam condensate are all believed to have a strong influence on the transformation process (e.g., Rimstidt and Cole 1983; Fournier 1985; Herdianita et al. 2000b; Hinman 1990; Lynne and Campbell 2003).

The water content in opal-A and opal-CT, hydrated silica dioxides ($SiO_2 \cdot nH_2O$), is a key component of these minerals as their total water content is 1.5 to 15.3 wt % (Tables 4.1). The total water content of opal is comprised of silanol groups (OH groups attached to silicon) and/or molecular water (Fig. 4.1). Type A molecular water is water trapped as isolated molecules in the silica matrix with little involvement in hydrogen

Table 4.1. Total water contents, and molecular and silanol water contents of opal-A, from a variety of locations, determined using a variety of analytical techniques.

Opal-A				
Location	**Sample #**	**Wt % H_2O_{Total}**	**Wt% H_2O_{Mol}**	**Wt% H_2O_{SiOH}**
Data from Jones and Renaut (2004)[a]				
Waikite Geyser, NZ	"dry opal-A"	5-6	-	-
Waikite Geyser, NZ	"wet opal-A"	12-13	-	-
Data from Campbell et al. (2002)[b]				
Ngatamariki, NZ	AU49860	6.27	-	-
Ngatamariki, NZ	AU49859	8.66	-	-
Data from de Jong et al. (1987)[c]				
Location not specified	5	6.91	2.04	4.6
Location not specified	8	6.79	2.68	4.1
Data from Adams et al. (1991)[d]				
Australia	S22	15.31	-	-
Idaho, U.S.A	S27	6.38	-	-
Data from Langer and Flörke (1974)				
North Carolina, U.S.A.	[S-am]-37	6.8[e]	6.1	0.7
		6.70[c]	-	-
		6.5[b]	-	-
Poland	[S-am]-90	3.7[e]	2.2	1.5
		3.49[c]	-	-
		3.5[b]	-	-
Coober, Australia	[S-am]-60	7.4[e]	6.5	0.9
		7.26[c]	-	-
Andamooka, Australia	[S-am]-79	6.0[e]	5.1	0.9
		5.79[c]	-	-
		6.0[b]	-	-
Data from Herdianita et al. (2000a)				
Wairakei drain sinter	Bulk sample	6.0[d]	-	-
		5.0[b]	1.0	4.7
Data from Herdianita et al. (2000b)[b]				
Atiamuri B, New Zealand	AU47243	7.8	3.7	4.1
Atiamuri A, New Zealand	AU47242	9.3	4.7	4.6
Omapere 6, New Zealand	AU47260	6.4	1.8	4.6
Atiamuri 14, New Zealand	AU47241	4.0	1.9	2.1
Ohakuri 48, New Zealand	AU47258	10.0	5.5	4.5
Data from Graetsch et al. (1990)[c]				
Coober, Australia	60	5.6		
Piaui, Brazil	275	5.0		

[a] Measured using electron microprobe technique
[b] Measured using thermogravimetric technique
[c] Measured using modified Karl Fisher titration.
[d] Measured using a modified Penfield technique
[e] Measured by near infrared spectroscopy

Table 4.1. Continued. Total water contents, and molecular and silanol water contents of opal-CT, from a variety of locations, determined using a variety of analytical techniques.

Opal-CT				
Location	**Sample #**	**Wt % H_2O_{Total}**	**Wt% H_2O_{Mol}**	**Wt% H_2O_{SiOH}**
Data from de Jong et al. (1987)[c]				
Location not specified	2	8.75	1.74	7.0
Location not specified	7	8.81	1.08	7.5
Data from Adams et al. (1991)[d]				
Australia	S1	5.02	-	-
Cornwall, England	S25	9.28	-	-
Data from Langer and Flörke (1974)				
Mexico	[S-am]-54	10.6[e]	10.4	0.2
		8.81[c]	-	-
		7.3[f]	-	-
Nova Ves/CSSR	[S-am]-59	3.7[e]	3.3	0.4
		3.72[c]	-	-
		3.5[f]	-	-
Data from Herdianita et al. (2000b)[b]				
Ohakuri 102, New Zealand	AU47259	6.3	4.2	2.1
Umukuri A, New Zealand	AU47271	4.9	3.8	1.1
Data from Graetsch et al. (1990)[c]				
Lake Eyre, Australia	43	3.6	3.6	<0.1

[b] Measured using thermogravimetric technique
[c] Measured using modified Karl Fisher titration.
[d] Measured using a modified Penfield technique
[e] Measured by near infrared spectroscopy

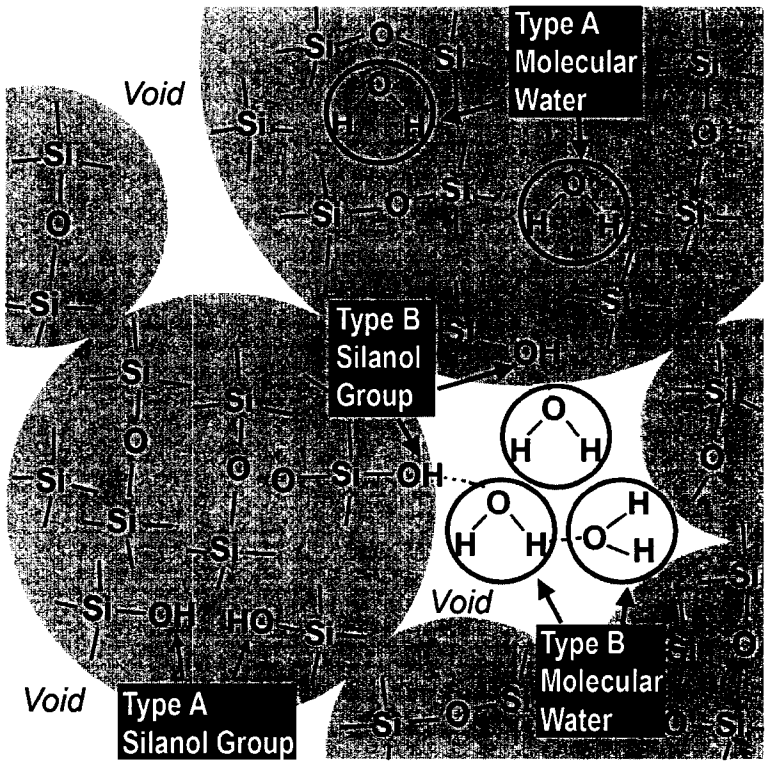

Figure 4.1. Schematic diagram of different forms of water present in opal detected using FTIR analysis. Spheres are illustrated here, however, the general concepts may be applied to all microstructures in opal-A and opal-CT. Type A molecular water is water isolated in the silica matrix, not involved in hydrogen bonding. Type B molecular water is adsorbed water in relatively large voids strongly involved in hydrogen bonding. Type A silanol groups are located at structural defects in the silica matrix, not involved in hydrogen bonding. Type B silanol groups are surface silanols strongly involved in hydrogen bonding. Dotted lines indicate hydrogen bonding. Based on Langer and Flörke (1974) and Graetsch (1994).

bonding, whereas type B molecular water is adsorbed to silica surfaces with strong involvement in hydrogen bonding (Langer and Flörke 1974; Flörke et al. 1991; Graetsch 1994). Type A silanol groups are located at structural defects, such as dislocations in the silica matrix, with little involvement in hydrogen bonding. Type B silanol groups are located on silica surfaces with strong involvement in hydrogen bonding (Langer and Flörke 1974; Flörke et al. 1991; Graetsch 1994).

Microscale variations in the total water content of opal-A have been detected using BSEI and EMP analyses (Jones and Renaut 2004); an important discovery given the potential loss of water in the transformation of opal-A to opal-CT (e.g., Herdianita et al. 2000b). Due to the relatively recent development of the EMP technique used to determine the total water content in opal, the technique was verified in this study using a long-established method of analysis, infrared spectroscopy (e.g., Segnit et al. 1965; Langer and Flörke 1974). Micro-Fourier transform infrared spectroscopy (FTIR) is a technique based on the absorption of functional groups in characteristic regions of the infrared spectrum, which allows for quantitative microscale analysis of hydrated siliceous minerals (Langer and Flörke 1974; Graetsch et al. 1985; Ito and Nakashima 2002; King et al. 2002). The total water contents of most types of sinter determined using both EMP and FTIR analyses are within the limits of experimental error (Tables 3.1-3.3). The porous and poorly consolidated nature of some sinters, and the high Al content (> 1 wt %) of other sinters, were the cause of the few discrepancies between the total water content determined using EMP and FTIR analysis. Overall, however, EMP analysis is a reliable method for the quantitative determination of the total water content in opal.

Analysis of porous and poorly consolidated siliceous sinter, such as porous friable sinter, using either EMP or FTIR analysis is problematic. Low total weight percents obtained using EMP analysis, difficulty in removing the bonding adhesive, and poor light transmission in FTIR analysis are common when analyzing porous and poorly consolidated sinter. Conversely, analysis of vitreous sinter is generally uncomplicated as it is non porous and very well consolidated; thus total weight percents are high in EMP analysis, the adhesive is readily removed while keeping the sinter intact, and light is transmitted well in FTIR analysis.

Although EMP analysis may be used at a much finer resolution than FTIR analysis (5 μm^2 and 150 μm^2, respectively), these methods are of comparable scale in contrast to bulk sample analyses based on coulometric Karl-Fisher titration, which require ~ 50 mg of sample for the determination of total water content in opal (Graetsch et al. 1985). Hence, both EMP and FTIR analysis have the advantage of spatial resolution over the bulk methods used to determine total water content, including loss on ignition (e.g., Nicholson and Parker 1990) and thermogravimetric analysis (e.g., Graetsch et al. 1985; Adams et al. 1991). EMP analysis has exceptional spatial resolution when considering microscale quantification (5 μm^2). The total water content of opal may be determined using either EMP or FTIR analysis; however, only FTIR analysis is capable of determining the content of different forms of water in opal. Using near infrared spectroscopy, two types of molecular water and silanol groups, with different involvement in hydrogen bonding, can be distinguished in opal (Fig. 4.1). The total water content, including the various forms of water, is a fundamental, yet poorly

understood aspect of both the deposition of opal-A and its subsequent transformation to opal-CT.

Spicules and flat-lying laminae of vitreous sinter in the Waikite Geyser complex offer the most striking evidence that the total water content of relatively young, unaltered opal-A deposits is highly variable (1-6 wt % difference) at the microscale level (Figs. 3.29B-C, 3.30A). Microscale variations in the total water content of opal-A are also evident in other types of sinter such as porous friable and patchy vitreous sinter (e.g. Figs. 3.37A-B, 3.38A). These variations in the total water content of the initial opal-A deposits may be attributed to variable precipitation conditions in the dynamic environment of hot springs. Rapid precipitation from highly supersaturated hot spring fluids is thought to produce opal-A deposits with a relatively high total water content, whereas slow precipitation rates are thought to produce opal-A with relatively low total water contents (Jones and Renaut 2004). Little is yet known, however, about the factors controlling the amount of water in opal-A deposits found in hot spring environments (Jones and Renaut 2004).

The total water content of different types of sinter in an opal-A deposit may also differ significantly (1-5 wt % difference) between sinter types (e.g. Fig. 3.30A). The relatively low total water content of the porous indurated sinter (4.7 wt %), which forms between spicules, compared to the spicules themselves (10.3 wt %), may be a result of the sheltered crevices between spicules retaining water between eruptions. This moisture between spicules allows for more gradual precipitation of the porous indurated sinter compared to relatively rapid precipitation of spicules, which form during wetting and drying periods (Jones and Renaut 2004). Conversely, different types of sinter may have

equivalent total water contents within an opal-A deposit; for example, the porous indurated and vitreous sinter, distal from the main vent from the Waikite Geyser Complex, have equivalent total water contents (7-9 wt %), but a higher total water content than the porous friable sinter (5.4 wt %) found in the deposit (Fig. 3.30C). The total water content of the initial opal-A deposit formed in hot spring systems is presumably influenced by numerous factors, such as the precipitation rate (e.g., Jones and Renaut 2004), pH levels (e.g., Carroll et al. 2002), and arrangement of spheres (e.g., Iler 1955). Thus, it is difficult to ascertain (1) why different types of sinter in some opal-A deposits contain the same amount of total water (e.g. Fig. 3.38A), whereas in other deposits, different types of sinter differ significantly in their total water content (e.g. Fig. 3.30A), and (2) why microscale variations in the total water content are evident in some opal-A deposits (e.g. Figs. 3.29B-C, 3.30A) and not others (e.g. Figs. 3.35C, 3.30C).

The total water content of sinter composed of opal-CT is also variable at both the microscale level (e.g. Figs. 3.37C-F, 3.38C-D) and between different types of sinter in a deposit (e.g. Fig. 3.39B). Although sinters composed of opal-CT generally have a lower total water content compared to sinters composed of opal-A, the total water content of some opal-CT samples can coincide with the total water content of some opal-A samples (Tables 3.1-3.3, and 4.2). In the Te Anarata succession in New Zealand the total water content of the youngest opal-A sinter deposits are higher than the total water content of the oldest opal-CT deposits (Fig. 3.38A, D). In the middle of the sequence, however, the total water content of sinters composed of opal-CT is equivalent to the total water content of opal-A deposits at the top of the sequence (Fig. 3.38A-C). Likewise, some of the

sinter composed of opal-CT from the succession at Geysir, Iceland, have total water contents equivalent to the overlying sinter composed of opal-A (Fig. 3.39).

The total water content of opal-CT deposits is probably affected by (1) the potential variations in the original total water content of its predecessor, opal-A and/or (2) the patchy nature its formation. It is evident that the total water content of relatively young opal-A deposits is variable (e.g. Fig. 3.30A-C). Consider two deposits of opal-A, one deposit with 12 wt % total water and another with 8 wt % total water. If both opal-A deposits lose 5 wt % total water during their transformation to opal-CT, going to 7 and 3 wt % total water, respectively, the first deposit at 7 wt % would still be similar to other opal-A deposits with 8 wt % total water. Thus, the variability in the total water content of the initial opal-A deposit results in some overlap of the total water in opal-A and opal-CT. The patchy and inhomogeneous nature of the mineralogy and microstructures of siliceous sinters has lead to the conclusion that the transformation of opal-A to opal-CT is likewise a patchy and discontinuous process (Lynne and Campbell 2004; Rodgers et al. 2004; Jones and Renaut in press). Similarly, the loss of water during the transformation of opal-A to opal-CT is patchy and inhomogeneous in nature. Opal-A deposits generally show a smaller range in their minimum and maximum total water contents than opal-CT (e.g. Fig. 3.38). The larger range in total water contents of opal-CT deposits may be due to its patchy and inhomogeneous formation. For example, some areas in the opal-CT deposit may have lost more water than other areas or perhaps the total water content in some areas of the deposit has not changed significantly from the time of opal-A precipitation. The factors controlling the loss of water, however, in the transformation of opal-A to opal-CT are not clear. The notion that opal-A has higher total water contents

than opal-CT as a result of the progressive loss of water in the transformation of opal-A to opal-CT is an idealized notion (cf. Herdianita et al. 2000b). Rather, the loss of total water in the transformation of opal-A to opal-CT is a variable process due to the undisputed patchy nature of this mineralogical transformation, at all levels. The total water content of the primary opal-A deposits likely has an influence on the total water content of the ensuing opal-CT.

The molecular water content of opal-A and opal-CT is formed largely of type B molecular water, which is adsorbed water in relatively large voids with strong involvement in hydrogen bonding (Figs. 3.31, 4.1). The amount of water in these voids is, in part, dependent on the arrangement of the microstructures; for example, loosely packed aggregates of spheres are able to enclose more water than a dense arrangement of spheres (Iler 1955). If the pore structure of spheres is open, however, water can readily escape (Segnit et al. 1965). Conversely, in a closely packed arrangement of spheres water may become trapped in the closed pores. There is no evidence in this study that different types of sinter (e.g. vitreous or porous friable sinter) composed of opal-A are preferentially enriched in type B molecular water (Fig 3.31). Sinter composed of opal-A located closest to the main vent at the Waikite Geyser complex, however, contains relatively more type B molecular water than sinter distal from the vent (Fig. 3.31A). With proximity to the vent comes more frequent exposure of the sinter to moisture provided by the emerging hydrothermal waters. More frequent exposure to moisture allows for more opportunity for the adsorption of molecular water to the silica surface. Sinter on the distal discharge apron is subject to changing flow paths, which may cause some sinter to dry out (Braunstein and Lowe 2001). The type of hot spring environment

influences the moisture content of the sinter as well. In a hot spring environment, hydrothermal waters are continually emerging, whereas in a geyser environment the frequency of eruptions is intermittent. Thus, the sinter surrounding a geyser may be subject to long periods of dryness between eruptions. Potentially, sinter exposed to dry conditions may allow for the preferential removal of type B molecular water over type A molecular water, which is isolated in the silica matrix. The depositional environment of sinter with respect to the vent appears to be more influential in the type of molecular water contained in opal-A than the type of sinter that is formed (Fig. 3.31A).

Sinter composed of opal-CT contains relatively more type B molecular water than sinter composed of opal-A (Fig. 3.40C). The larger inner surface and irregular microstructure of opal-CT allows for more trapped water compared to the relatively dense network of spheres in opal-A (Langer and Flörke 1974; Flörke et al. 1990). Opal-CT deposits are not always enriched in type B molecular water compared to opal-A; for example, the sinter deposits of opal-A and opal-CT from Te Anarata have approximately the same proportion of molecular water types (Fig. 3.31B). At this point, it is difficult to ascertain if the type of molecular water content in opal-CT is primarily due to diagenesis or a result of the variability in the molecular water of the original opal-A deposit.

Sinters composed of opal-A have relatively more type B silanol groups, which are surface silanols with a strong involvement in hydrogen bonding, compared to sinters composed of opal-CT (Figs. 3.41C, 4.1). During polymerization, there is a strong tendency for silicic acid to maximize the number of siloxane (Si-O-Si) bonds and minimize silanol groups; however, silanols will form on the silica surface in an effort to complete tetrahedral coordination (Iler 1979). Hence, during the precipitation of opal-A,

surface silanols may be preferentially formed over silanols in structural defects (type A silanol groups). Type A silanol groups are not expected in a stable, undisturbed silica structure but may be common in flawed structures where the siloxanes are distorted in the matrix (Kronenberg 1994). Thus, the relatively high content of type A silanol groups in sinter composed of opal-CT may possibly be attributed to dissolution reactions, in which distorted siloxane bonds, in the silica matrix, may be broken and hydrated, forming type A silanols (Fig. 4.2). Assuming silica maturation occurs via a dissolution-reprecipitation (e.g., Rice et al. 1995; Landmesser 1998; Herdianita et al. 2000b; Rodgers et al. 2004), the dissolution process may present unstable conditions in the silica structure, thus promoting a relative increase in type A silanol groups.

The total water content of opal-A and opal-CT is formed mostly of molecular water rather than silanols (Fig. 3.33) (Segnit et al. 1965; Langer and Flörke 1974; Graetsch et al. 1990, 1994; Flörke et al. 1991). The molecular water content (H_2O_{mol}) is the sum of type A and type B molecular water, and the silanol content (H_2O_{SiOH}) is likewise comprised of type A and B silanol groups. In opal-A deposits, this may be due to the tendency of silicic acid to maximize the number of siloxane (Si-O-Si) bonds, thereby minimizing the silanol groups during polymerization (Iler 1979). The adsorption of molecular water in opal may be likened to the step-wise water-surface interactions in freshly cleaved quartz, in which molecular water is preferentially adsorbed to surface silanols (Fig. 4.3) (Lasaga and Gibbs 1990; Dove and Rimstidt 1994). Surface silanols provide an adsorption site for molecular water (Dove and Rimstidt 1994), as this absorbed water film increases, it is essentially limited only by the size of the pore space and the amount of water available. Thus, the potential for molecular water adsorption is

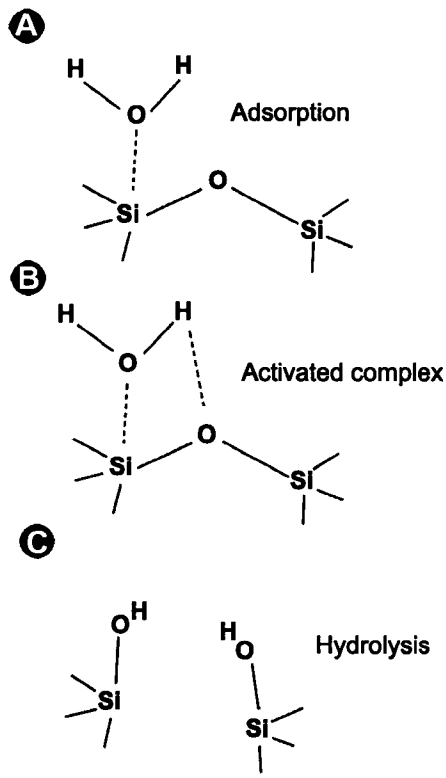

Figure 4.2. Schematic diagram of elementary reactions involved in a single hydrolysis reaction of silica to form silanols. Based on Lasaga and Gibbs (1990). Type A silanol groups may form where siloxanes are distorted in the silica matrix. Such reactions may occur during the dissolution process during the transformation of opal-A to opal-CT. **A)** Adsorption of molecular onto Si of a siloxane bond in the silica matrix. **B)** An activated complex is formed. **C)** Hydrolysis is complete, resulting in the formation of silanol groups.

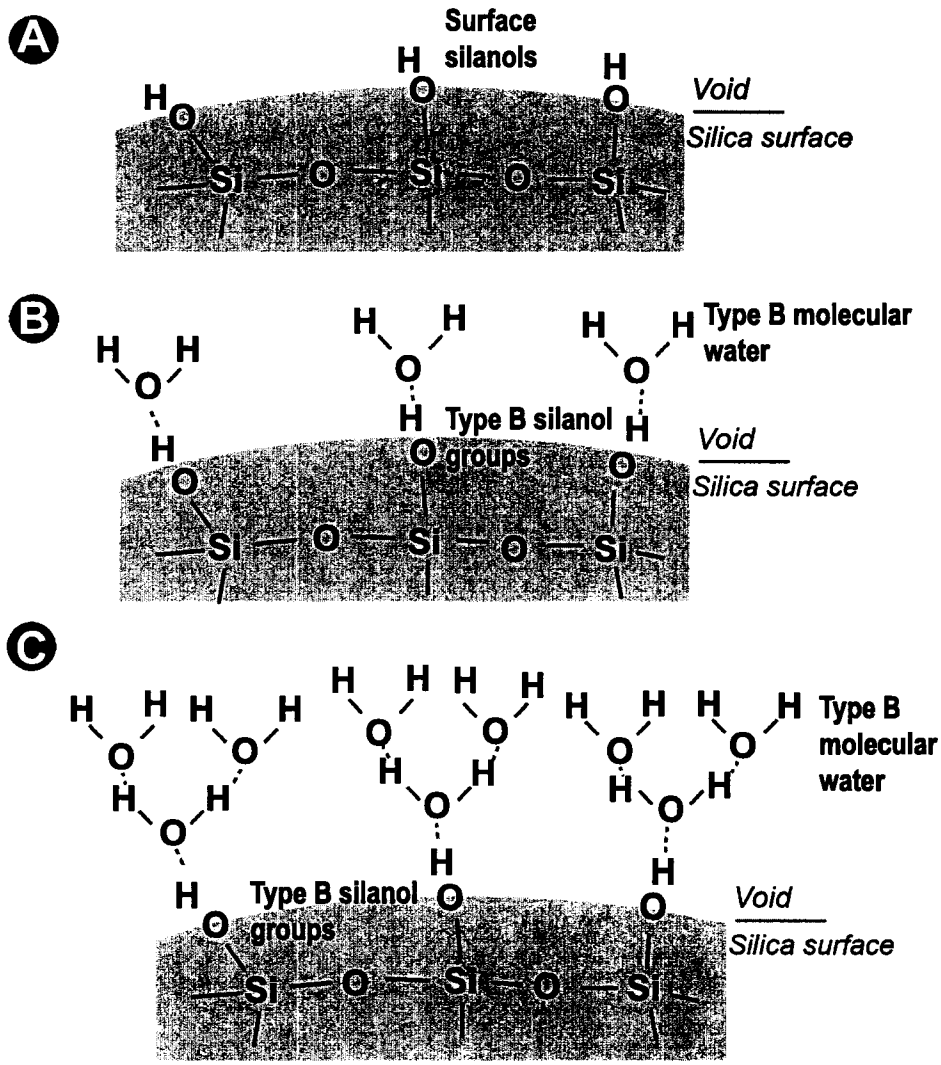

Figure 4.3. Schematic diagram illustrating step-wise water surface interactions of opal. Based on diagram in Dove and Rimstidt (1994). Dotted lines indicate hydrogen bonding. **A)** Silanol groups on a silica surface. **B)** Layer of water adsorbed onto surface silanols, forming type B molecular water and type B silanol groups. **C)** The content of silanol groups remains the same as the adsorption of molecular water continues to increase. Type B molecular water is limited by the size of the void and the availability of water.

relatively great in comparison to the amount of silanol groups that can form during the precipitation of opal.

There is considerable overlap in the molecular water content (H_2O_{mol}) of opal-A and opal-CT; however, the silanol content (H_2O_{SiOH}) is consistently higher in opal-A than opal-CT (Fig. 3.33) (Segnit et al. 1965; Langer and Flörke 1974; Flörke et al. 1991; Smith 1998). Low H_2O_{SiOH} contents can be expected in hydrated siliceous minerals, such as opal-CT, which form slowly, at relatively low temperatures (Langer and Flörke 1974). Based on a dissolution-reprecipitation pathway for the transformation of opal-A to opal-CT, the slow reprecipitation of opal-CT may promote an increase in siloxane bonds, consequently lowering the H_2O_{SiOH} content. Thus, in the transformation of opal-A to opal-CT, the H_2O_{SiOH} content generally decreases before a significant loss of H_2O_{mol} occurs as a result of an increase in siloxane bonds. The increase in siloxane bonds is presumed to yield more domains of short-range ordering, which produce the characteristic XRD pattern of opal-CT (Rodgers et al. 2004).

Siliceous sinters composed of opal-A and/or opal-CT are generally formed of a variety of different sinter types (e.g. Fig. 3.15). It is apparent from hand sample and XRD analyses that regardless of geographical location (e.g. New Zealand or Iceland) neither deposits of opal-A or opal-CT are dominated by any particular type of sinter. For example porous friable sinter is common in sinters composed of opal-A and opal-CT (e.g. Fig. 3.25). Vitreous, patchy vitreous, dull indurated and porous indurated sinters are also common to deposits composed of either opal-A or opal-CT (e.g. Figs. 3.1A, 3.8A). The notion that opal-A deposits are more porous and less dense than opal-CT deposits is not always reflected in the macroscopic appearance of sinter (cf. Herdianita et al. 2000b;

Lynne et al. 2005). Many physical properties are common to both opal-A and opal-CT, hence the prime criterion used to distinguish these minerals remains the distinct nature of their XRD patterns (Fig. 2.1); not their physical macroscopic appearance (Jones and Segnit 1971).

The mineralogical and associated microstructural changes in the transformation of opal-A to opal-CT in siliceous sinter has been assessed using XRD and SEM analyses (Herdianita et al. 2000a, 2000b; Lynne and Campbell 2003, 2004; Rodgers et al. 2004; Lynne et al. 2005). The major challenge in linking XRD and SEM analyses is the variance in scale between the two methods (Campbell et al. 2001; Rodgers and Hampton 2003; Jones and Renaut in press). A relatively large volume of sample is required for XRD analysis (typically 200-300 mg) compared to the microstructural elements assessed with SEM analysis. Given that the transition from opal-A to opal-CT is known to be a discontinuous and patchy process at various scales (e.g., Campbell et al. 2001; Lynne et al. 2005; Jones and Renaut in press), a method which allows for microscale identification of opal-A and opal-CT will invariably reveal additional information unattainable with the current methods of analyses. Reliable methods for microscale identification of opal-A and opal-CT, however, have yet to be developed (cf. Rice et al. 1995; Rodgers and Hampton 2003; Lynne et al. 2005). The issue of scale can be partly overcome by examining large areas of a sample on the SEM (cf. Jones and Renaut, in press) so that a complete array of textures can be established.

Sinters composed of opal-A are formed largely of spheres and silicified microbes (Fig. 3.28). Sinters composed of opal-CT are most commonly formed of lepispheres, bumpy spheres, silicified microbes, and nanospheres (Fig. 3.28). Dissolution fabrics and

reprecipitation fabrics are most common in sinters composed of opal-CT (e.g. Fig. 3.22A-D), but are present in some opal-A deposits (e.g. Fig. 3.14E). The most obvious evidence of dissolution is inverse opal; the dissolution is commonly incomplete, leaving evidence of the original fabric. Spheres tightly enveloped in cement may still be present in some spaces of type I inverse opal (Fig. 3.22B). Type II inverse opal is most easily identified in areas where some of the original opal cement is still present (Fig. 3.14E). Spheres with small holes are also a product of preferential dissolution and have been attributed to the earliest stages of sinter diagenesis (Lynne and Campbell 2004). Unlike inverse opal, however, the spheres with holes are not common in the sinter observed in this study and are only evident in the sinter distal from the Waikite Geyser vent (Fig. 3.6D). Inverse opal and spheres with holes are produced through preferential dissolution, which indicates that the solubility of opal is variable, at scales as low as 150 nm^2. Potentially, these differences in opal solubility may be attributed to variations in the water content (Jones and Renaut 2004). This is plausible given the evidence of microscale variations in the total water content of opal-A (e.g. Fig. 3.29B-C); however, it is difficult to confirm as it is not possible to decipher variations in water content at the level required to assess preferential dissolution. Nevertheless, the evidence of opal dissolution permits the release of Si and O into solution, which then becomes available for reprecipitation. This supports the idea of a dissolution-reprecipitation pathway in the transformation of opal-A to opal-CT.

Features present in sinter indicative of silica reprecipitation, including multilobed masses of spheres covered in nanospheres, bumpy spheres, knobby lepispheres, and lepispheres, are most common in sinter composed of opal-CT (Fig. 3.28). Nanospheres

covering multilobed masses of spheres suggest multiple stages of silica precipitation (Fig. 3.2F); however, it is unclear if the nanospheres formed from the initial parent fluid or if they are associated with onset of opal-CT precipitation. Opal-A deposits are thought to form rapidly through the agglomeration of nanospheres which then form spheres (Smith et al. 2003). Nanospheres, however, have also been associated with the formation of bumpy spheres and "incipient lepispheres" (Lynne et al. 2005). The formation of bumpy spheres (Lynne et al. 2005), and similarly, ornamentation features (Jones and Renaut in press), have been attributed to the growth of secondary features on the surface of smooth spheres. In some instances, however, bumpy spheres may have formed through the amalgamation of nanospheres. Discrete clusters of nanospheres, < 200 nm in diameter, are found in regions with bumpy spheres (Fig. 3.18) and where bumpy spheres develop in the voids created by type I inverse opal (Fig. 3.22C). Knobby lepispheres, also termed incipient lepispheres (e.g., Lynne and Campbell 2004; Rodgers et al. 2004), have an ordered appearance of intersecting structures similar to lepispheres (Fig. 2.4C-E). It is uncertain, however, if bumpy spheres and/or knobby lepispheres are in fact the direct predecessor of lepispheres or if they may represent another form of opal-CT.

Several different morphological schemes have been invoked to explain the formation of lepispheres (Lynne and Campbell 2004; Lynne et al. 2005). Lynne and Campbell (2004)'s scheme involves the unfolding of spheres with holes into loose piles of silica platelets which is subsequently followed by an aggregation of the platelets to form lepispheres. This scheme, however, seems unrealistic given that spheres are either homogeneous or formed of concentrically nested laminae (Jones and Renaut in press). Although spheres with holes are evident in sinter observed in this study, these features

are not common (Fig. 3.6D). The morphological similarity of lepispheres and knobby lepispheres incite their correlation in the transformation of opal-A to opal-CT. Apart from their physical similarities, it is not clear how the proposed evolution of bumpy spheres and "incipient lepispheres" to lepispheres occurs with respect to the dissolution-reprecipitation pathway (Lynne and Campbell 2004; Lynne et al. 2005). In fact, the schemes proposed by Lynne and Campbell (2004) and Lynne et al. (2005) portray a physical reorganization of these features into the proposed end product of opal-CT, lepispheres, implying a solid state transformation not a dissolution-reprecipitation pathway. Thus, it is unclear if Lynne and Campbell (2004) and Lynne et al. (2005) favour a dissolution-reprecipitation pathway, a solid state transformation or a combination of both for the opal-A to opal-CT conversion. Lepispheres are the most commonly illustrated feature of opal-CT (e.g., Flörke et al. 1975; Kastner et al. 1977; Elzea et al. 1994; Herdianita et al. 2000b). It does not mean, however, that all opal-CT occurs as lepispheres (Knauth 1994). The common occurrence of bumpy spheres and knobby lepispheres in opal-CT rather than in opal-A (Fig. 3.28) may be an indication that these features are a distinct form of opal-CT.

The presence of dissolution fabrics, such as type II invserse opal (Fig. 3.14E), and reprecipitation fabrics, such as nanospheres covering multilobed masses of spheres (Fig. 3.2F) in some sinter composed of opal-A illustrate early post-depositional alteration. Substantial post-depositional growth and textural changes of sinter are facilitated wherever an aqueous film is present and may take place at an early stage in the diagenesis of opal-A (Smith et al. 2003). The presence of such features in opal-A deposits is, however, limited (Fig. 3.28). The limited morphological alteration in opal-A deposits

suggests the laminae of different types of sinter in hot spring deposits, such as porous indurated and patchy vitreous sinter (e.g. Figs. 3.1A, 3.12A), may be attributed to variations in precipitation conditions rather than diagenetic alteration (cf. Lynne and Campbell 2004). The physical appearance of opal-A deposits initially produced by the precipitation of silica from supersaturated hot spring fluids is thought to be a product of various factors such as the degree of silica saturation (e.g., Iler 1979: Rimstidt and Cole 1983; Fournier 1985; Herdianita et al. 2000b; Rodgers et al. 2004), variations in water temperature (e.g., Fournier 1985) and/or depositional environments within hot spring systems (e.g. Rimstidt and Cole 1983; Braunstein and Lowe 2001).

The patchy vitreous sinter in some deposits of opal-A may be due to steam alteration. Isopachous laminae are highlighted by rising steam and sulphuric gases (H_2S, SO_2) and scalloped surfaces are produced by steam alteration (Jones and Renaut 2003a). These features, associated with steam alteration are prominent in the patchy vitreous sinter of sample NZ 603, from the Waikite Geyser complex, New Zealand (Fig. 3.4) and in the patchy vitreous sinter of sample ICE-87, from Geysir, Iceland (Fig. 3.26). Both of these deposits are associated with high Al contents (> 1 wt %) (Tables 3.1, 3.3). It is unclear, however, whether Al-rich opal (> 1 wt %) is a result of post-depositional Al^{3+} substitution for Si^{4+} (e.g., Graetsch et al. 1987) or if Al^{3+} was present in the original hydrothermal fluids, which may have aided in silica deposition by bridging the negatively charge silica colloids (Iler 1979). Little is known about the relationship, if any, between high Al contents and steam alteration in sinter, nevertheless, given the evidence of these features in deposits of opal-A from different geographical locations, it is clear that such features are not exclusive to a particular hot spring environment.

Chapter 5 - Conclusions

The transformation of opal-A to opal-CT in siliceous sinter deposits is a phenomenon which has been investigated in diverse hot spring environments from around the world including Yellowstone National Park, U.S.A. (Hinman and Walter 2005), Opal Mound, U.S.A. (Lynne et al. 2005), the Taupo Volcanic Zone, New Zealand (e.g., Lynne and Campbell, 2004), El Tatio, Chile (Fernandez-Turiel et al. 2005), and Geysir, Iceland (Jones and Renaut in press). The sinters composed of opal-A and opal-CT from New Zealand and Iceland in this study offer a direct comparison of sinter diagenesis from two different geographical locations. The trends in the water content (total water and different forms of water) of opal-A and opal-CT are apparent in sinters from both New Zealand and Iceland. In spite of different geographical locations, silanol groups (H_2O_{SiOH}) appear to decrease prior to molecular water (H_2O_{mol}) loss in the transformation of opal-A to opal-CT. Dissolution fabrics, such as inverse opal, and reprecipitation fabrics, such as bumpy spheres, are most evident in sinters composed of opal-CT, as opposed to opal-A, in both deposits from New Zealand and Iceland. Deposits of opal-A and opal-CT from these geographically diverse areas are likewise composed of different types of sinter ranging from porous friable sinter to vitreous sinter. Despite variable precipitation conditions and drastically different diagenetic environments, the siliceous sinters from New Zealand and Iceland display similar physical attributes (i.e. types of sinter), microstructures and water contents in the deposits composed of opal-A and opal-CT. Although the diagenetic mechanisms are uncertain, the results of this study indicate that sinter from different depositional and diagenetic environments follows analogous pathways in the transformation from opal-A to opal-CT.

The detailed analysis of the physical appearance, microstructures, and water content of siliceous sinters composed of opal-A and opal-CT from the Whakarewarewa geothermal area in New Zealand and the Geysir discharge apron in Iceland has led to the following conclusions:

- Electron microprobe (EMP) analysis is a viable method for determination of total water content in opal.
- Micro-Fourier transform infrared (FTIR) spectroscopy is advantageous because it allows for the identification of different forms of water in opal.
- Deposits of opal-A and opal-CT are composed of many different textured types of sinter.
- Opal-A and opal-CT are not distinguishable in hand sample, only using X-ray diffraction analysis.
- The deposition of opal-A from hot spring fluids results in the formation of different types of sinter, variable microstructures, and variable water contents depending on precipitation conditions, which in turn affect the appearance and water content of the ensuing opal-CT deposits.
- The transformation of opal-A to opal-CT does not follow a linear pathway, rather it is patchy and inhomogeneous at all levels, as indicated by the variability observed in the water content, microstructures, and mineralogy within a succession of sinter.
- Silanol groups are lost prior to molecular water in the transformation of opal-A to opal-CT.

- Dissolution and reprecipitation fabrics are evident primarily in sinters composed of opal-CT, supporting the idea of a dissolution-reprecipitation mechanism in the transformation of opal-A to opal-CT.
- Given the similarities in physical appearance, microstructures, and water content of sinter deposits from New Zealand and Iceland, two vastly different depositional and diagenetic environments, there must be common mechanisms in both the deposition of opal-A and its transformation to opal-CT.

References

ADAMS, S.J., HAWKES, G.E., and CURZON, E.H., 1991, A solid state ^{29}Si nuclear magnetic resonance study of opal and other hydrous silicas: American Mineralogist, v. 76, p. 1863-1871.

AINES, R.D., and ROSSMAN, G.R., 1984, Water in minerals? A peak in the infrared: Journal of Geophysical Research, v. 89, p. 4059-4071.

ALLIS, R.G., and LUMB, J.T., 1992, The Rotorua geothermal field, New Zealand: its physical setting, hydrology, and response to exploitation: Geothermics, v. 21, p. 7-24.

BARTH, T.F.W., 1940, Geysir in Iceland: American Journal of Science, v. 238, p. 381-407.

BARTH, T.F.W., 1950, Volcanic Geology Hot Springs and Geysers of Iceland: Washington, Carnegie Institution of Washington, 174 p.

BEVINGTON, P.R., 1969, Data reduction and error analysis for the physical sciences: New York, McGraw Hill, 336 p.

BRAUNSTEIN, D.G., and LOWE, D.R., 2001, Relationship between spring and geyser activity and the deposition and morphology of high temperature (> 73°C) siliceous sinter, Yellowstone National Park, Wyoming, U.S.A.: Journal of Sedimentary Research, v. 71, p. 747-763.

CADY, S.L., and FARMER, J.D., 1996, Fossilization processes in siliceous thermal springs: trends in preservation along thermal gradients, Evolution of hydrothermal ecosystems on Earth (and Mars?): Ciba Foundation Symposium 202: Chichester, Wiley, p. 150-173.

CAMPBELL, K.A., SANNAZZARO, K., RODGERS, K.A., HERDIANITA, N.R., and BROWNE, P.R.L., 2001, Sedimentary facies and mineralogy of the late Pleistocene Umukuri silica sinter, Taupo Volcanic Zone, New Zealand: Journal of Sedimentary Research, v. 71, p. 727-746.

CAMPBELL, K.A., RODGERS, K.A., BROTHERIDGE, J.M.A., and BROWNE, P.R.L., 2002, An unusual modern silica-carbonate sinter from Pavlova spring, Ngatamariki, New Zealand: Sedimentology, v. 49, p. 835-854.

CARR, R.M., and FYFE, W.S., 1958, Some observations on the crystallization of amorphous silica: American Mineralogist, v. 43, p. 908-916.

CARROLL, S.A., MAXWELL, R.S., BOURCIER, W., MARTIN, S., and HULSEY, S., 2002, Evaluation of silica-water surface chemistry using NMR spectroscopy: Geochimica et Cosmochimica Acta, v. 66, p. 913-926.

DANYUSHEVSKY, L.V., FALLOON, T.J., SOBOLEV, A.V., CRAWFORD, A.J., CARROLL, M., and PRICE, R.C., 1993, The H_2O content of basalt glasses from Southwest Pacific back-arc basins: Earth and Planetary Science Letters, v. 117, p. 347-362.

DARRAGH, P.J., GASKIN, A.J., TERRELL, B.C., and SANDERS, J.V., 1966, Origin of precious opal: Nature, v. 209, p. 13-16.

DE JONG, B.H.W.S., VAN HOEK, J., VEEMAN, W.S., and MANSON, D.V., 1987, X-ray diffraction and ^{29}Si magic-angle-spinning NMR of opals: Incoherent long- and short-range order in opal-CT: American Mineralogist, v. 72, p. 1195-1203.

DEMISSIE, Y., 2003, Transient electromagnetic resistivity survey at the Geysir geothermal field, S. Iceland, Geothermal Training Program, Reports 2003: Reykjavik, The United Nations University, p. 143- 164.

DOVE, P.M., and RIMSTIDT, J.D., 1994, Silica-water interactions, *in* Heany, P.J., Prewitt, C.T., and Gibbs, G.V., eds., Silica; Physical Behavior, Geochemistry and Materials Applications: Reviews in Mineralogy: Washington, Mineralogical Society of America, p. 259-308.

ELZEA, J.M., ODOM, I.E., and MILES, W.J., 1994, Distinguishing well ordered opal-CT and opal-C from high temperature cristobalite by x-ray diffraction: Analytica Chimica Acta, v. 286, p. 107-116.

FERNANDEZ-TURIEL, J.L., GARCIA-VALLES, M., GIMENO-TORRENTE, D., SAAVERDRA-ALONSO, J., and MARTINEZ-MANENT, S., 2005, The hot spring and geyser sinters of El Tatio, Northern Chile: Sedimentary Geology, v. 180, p. 125-147.

FLÖRKE, O.W., JONES, J.B., and SEGNIT, E.R., 1975, Opal-CT crystals: Neues Jahrb Mineral Monatsh, v. H8, p. 369-377.

FLÖRKE, O.W., GRAETSCH, H., and JONES, J.B., 1990, Hydrothermal deposition of cristobalite: Neues Jahrb. Mineral. Monatsh., v. H2, p. 81-95.

FLÖRKE, O.W., GRAETSCH, H., MARTIN, B., ROLLER, K., and WIRTH, R., 1991, Nomenclature of micro- and non-crystalline silica minerals, based on structure and microstructure: Neues Jahrbuch Miner. Abh., v. 163, p. 19-42.

FORBES, C.S., 1860, Iceland, its Volcanoes, Geysers, and Glaciers: London, 255 p.

FOURNIER, R.O., 1985, The behavior of silica in hydrothermal solutions, *in* Berger, B.R., and Bethke, P.M., eds., Geology and Geochemistry of Epithermal Systems: Reviews in Economic Geology: Chelsea, MI, Society of Economic Geologists, p. 45-61.

FRÖHLICH, F., 1989, Deep-sea biogenic silica: new structural and analytical data from infrared analysis - geological implications: Terra Nova, v. 1, p. 267-273.

GLOVER, R.B., and MROCZEK, E.K., 1998, Changes in silica chemistry and hydrology across the Rotorua geothermal field, New Zealand: Geothermics, v. 27, p. 183-196.

GORYNIUK, M.C., RIVARD, B.A., and JONES, B., 2004, The reflectance spectra of opal-A (0.5-25 μm) from the Taupo Volcanic Zone: Spectra that may identify hydrothermal systems on planetary surfaces: Geophysical Research Letters, v. 31, p. Art. No. L24701.

GRAETSCH, H., FLORKE, O.W., and MIEHE, G., 1985, The nature of water in chalcedony and opal-C from Brazilian agate geodes: Phys. Chem. Minerals, v. 12, p. 300-306.

GRAETSCH, H., FLORKE, O.W., and MIEHE, G., 1987, Structural defects in microcrystalline silica: Phys. Chem. Minerals, v. 14, p. 249-257.

GRAETSCH, H., MOSSET, A., and GIES, H., 1990, XRD and 29Si MAS-NMR study on some non-crystalline silica minerals: Journal of Non-Crystalline Solids, v. 119, p. 173-180.

GRAETSCH, H., 1994, Structural characteristics of opaline and microcrystalline silica minerals, *in* Heany, P.J., Prewitt, C.T., and Gibbs, G.V., eds., Silica; Physical Behavior, Geochemistry and Materials Applications: Reviews in Mineralogy: Washington, Mineralogical Society of America, p. 209-232.

GUIDRY, S.A., and CHAFETZ, H.S., 2003a, Anatomy of siliceous hot springs: examples from Yellowstone National Park, Wyoming, USA: Sedimentary Geology, v. 157, p. 71-106.

GUIDRY, S.A., and CHAFETZ, H.S., 2003b, Depositional facies and diagenetic alteration in a relict siliceous hot-spring accumulation: examples from Yellowstone National Park, U.S.A.: Journal of Sedimentary Research, v. 73, p. 806-823.

HARRIS, D.C., 1987, Quantitative Chemical Analysis: New York, W.H. Freeman and Company, 818 p.

HERDIANITA, N.R., RODGERS, K.A., and BROWNE, P.R.L., 2000a, Routine instrumental procedures to characterise the mineralogy of modern and ancient silica sinters: Geothermics, v. 29, p. 65-81.

HERDIANITA, N.R., ROGERS, K.A., and BROWNE, P.R.L., 2000b, Mineralogical and morphological changes accompanying ageing in silica sinters: Mineralium Deposita, v. 35, p. 48-62.

HINMAN, N.W., 1990, Chemical factors influencing the rates and sequences of silica phase transitions: effects of organic constituents: Geochemica et Cosmochemica Acta, v. 54, p. 1563-1574.

HINMAN, N.W., and WALTER, M.R., 2005, Textural preservation in siliceous hot spring deposits during early diagenesis: Examples from Yellowstone National Park and Nevada, U.S.A.: Journal of Sedimentary Research, v. 75, p. 200-215.

HRÓARSSON, B., and JÓNSSON, S.S., 1992, Geysers and Hot Springs in Iceland: Reykjavík, Mál Og Menning, 158 p.

ILER, R.K., 1955, The colloid chemistry of silica and silicates: New York, Cornell University Press, 324 p.

ILER, R.K., 1979, The Chemistry of Silica: New York, John Wiley & Sons, 866 p.

ISAACS, C.M., 1982, Porosity reduction during diagenesis of the Monterey Formation, Santa Barbara Coastal Area, California, *in* Garrison, R.E., and Douglas, R.G., eds., The Monterey Formation and related siliceous rocks of California: Los Angeles, SEPM Pacific Secion, p. 257-271.

ITO, Y., and NAKASHIMA, S., 2002, Water distribution in low-grade siliceous metamorphic rocks by micro-FTIR and its relation to grain size: a case from the Kanto Mountain region, Japan: Chemical Geology, v. 189, p. 1 – 18.

JONES, B., RENAUT, R.W., and ROSEN, M.R., 1997, Vertical zonation of biota in microstomatolites associated with hot springs, North Island, New Zealand: Palaios, v. 12, p. 220-236.

JONES, B., RENAUT, R.W., and ROSEN, M.R., 1998, Microbial biofacies in hot-spring sinters: A model based on Ohaaki Pool, North Island, New Zealand: Journal of Sedimentary Research, v. 68, p. 413-434.

JONES, B., RENAUT, R.W., and ROSEN, M.R., 1999, Actively growing siliceous oncoids in the Waiotapu geothermal area, North Island, New Zealand: Journal of the Geological Society, London, v. 156, p. 89-103.

JONES, B., RENAUT, R.W., and ROSEN, M.R., 2000, Stromatolites forming in acidic hot-spring waters, North Island, New Zealand: Palaios, v. 15, p. 450-475.

JONES, B., RENAUT, R.W., and ROSEN, M.R., 2001a, Taphonomy of silicified filamentous microbes in modern geothermal sinters - Implications for identification: Palaios, v. 16, p. 580-592.

JONES, B., RENAUT, R.W., and ROSEN, M.R., 2001b, Microbial construction of siliceous stalactites at geyers and hot springs: Examples from the Whakarewarewa geothermal area, North Island, New Zealand: Palaios, v. 16, p. 73-94.

JONES, B., RENAUT, R.W., and ROSEN, M.R., 2001c, "Geyer eggs" from the Te Whakarewarewatangateopetauaawahiao, North Island, New Zealand: Journal of Sedimentary Research, v. 71, p. 190-204.

JONES, B., RENAUT, R.W., ROSEN, M.R., and ANSDELL, K.M., 2002, Coniform stromatolites from geothermal systems, North Island, New Zealand: Palaios, v. 17, p. 84-103.

JONES, B., and RENAUT, R.W., 2003a, Petrography and genesis of spicular and columnar geyserite from the Whakarewarewa and Orakeikorako geothermal areas, North Island, New Zealand: Canadian Journal of Earth Sciences, v. 40, p. 1585-1610.

JONES, B., and RENAUT, R.W., 2003b, Hot spring and geyer sinters: the integrated product of precipitation, replacement, and deposition: Canadian Journal of Earth Sciences, v. 40, p. 1549-1569.

JONES, B., KONHAUSER, K.O., RENAUT, R.W., and WHEELER, R.S., 2004, Microbial silicification in Iodine Pool, Waimangu geothermal area, North Island, New Zealand: implications for recognition and identification of ancient silicified microbes: Journal of the Geological Society of London, v. 161, p. 989-993.

JONES, B., and RENAUT, R.W., 2004, Water content of opal-A: Implications for the origin of laminae in geyserite and sinter: Journal of Sedimentary Research, v. 74, p. 117-128.

JONES, B., and RENAUT, R.W., in press, The opal-A to opal-CT transition in siliceous sinters from the discharge apron of Geysir, Iceland.

JONES, J.B., and SEGNIT, E.R., 1969, Water in sphere-type opal: Mineralogical Magazine, v. 37, p. 357-361.

JONES, J.B., and SEGNIT, E.R., 1971, The nature of opal I. Nomenclature and constituent phases: Journal of the Geological Society of Australia, v. 18, p. 57-68.

JONES, J.B., and SEGNIT, E.R., 1972, Genesis of cristobalite and tridymite at low temperatures: Journal of the Geological Society of Australia, v. 18, p. 419-422.

KASTNER, M., KEENE, J.B., and GIESKE, J.M., 1977, Diagenesis of siliceous oozes- I. Chemical controls on the rate of opal-A to opal-CT transformation an experimental study: Geochimica et Cosmochimica Acta, v. 41, p. 1041-1059.

KING, P.L., VENNEMANN, T.W., HOLLOWAY, J.R., HERVIG, R.L., LOWENSTERN, J.B., and FORNERIS, J.F., 2002, Analytical techniques for volatiles: A case study using intermediate (andesitic) glasses: American Mineralogist, v. 87, p. 1077-1089.

KING, P.L., RAMSEY, M.S., MCMILLIAN, P.F., and SWAYZE, G., 2004, Laboratory Fourier transform infrared spectroscopy methods for geologic samples, *in* King, P.L., Ramsey, M.S., and Swayze, G., eds., Infrared Spectroscopy in Geochemistry, Exploration Geochemistry and Remote Sensing, Mineral. Assoc. Canada, Short Course, p. 57-91.

KNAUTH, L.P., 1994, Petrogenesis of chert, *in* Heany, P.J., Prewitt, C.T., and Gibbs, G.V., eds., Silica; Physical Behavior, Geochemistry and Materials Applications: Reviews in Mineralogy: Washington, Mineralogical Society of America, p. 233-258.

KONHAUSER, K.O., JONES, B., REYSENBACH, A.-L., and RENAUT, R.W., 2003, Hot spring sinters: keys to understanding Earth's earliest life forms: Canadian Journal of Earth Sciences, v. 40, p. 1713-1724.

KRONENBERG, A.K., 1994, Hydrogen speciation and chemical weakening of quartz, *in* Heany, P.J., Prewitt, C.T., and Gibbs, G.V., eds., Silica; Physical Behavior, Geochemistry and Materials Applications: Reviews in Mineralogy: Washington, Mineralogical Society of America, p. 123-176.

LANDMESSER, M., 1998, "Mobility by Metastability" in Sedimentary and Agate Petrology: Applications: Chemie der Erde, Geochemistry, v. 58, p. 1-22.

LANGER, K., and FLÖRKE, O.W., 1974, Near infrared absorption spectra (4000-9000cm^{-1}) of opals and the role of "water" in the $SiO_2 \cdot nH_2O$ minerals: Fortschr. Miner., v. 52, p. 17-51.

LASAGA, A.C., and GIBBS, G.V., 1990, Ab-initio quantum mechanical calculations of water-rock interactions: Adsoption and hydrolysis reactions: American Journal of Science, v. 290, p. 263-295.

LLYOD, E.F., 1975, Geology of Whakarewarewa hot spring: New Zealand Department of Scientific and Industrial Research, Information Series no. 111, 24 p.

LOWE, D.R., and BRAUNSTEIN, D., 2003, Microstructure of high-temperature (>73°C) siliceous sinter deposited around hot springs and geyers, Yellowstone National Park: the role of biological and abiological processes in sedimentation: Canadian Journal of Earth Sciences, v. 40, p. 1611-1642.

LYNNE, B.Y., and CAMPBELL, K.A., 2003, Diagenetic transformations (opal-A to quartz) of low- and mid-temperature microbial textures in siliceous hot-spring deposits,

Taupo Volcanic Zone, New Zealand: Canadian Journal of Earth Sciences, v. 40, p. 1679-1696.

LYNNE, B.Y., and CAMPBELL, K.A., 2004, Morphological and mineralogic transitions from opal-A to opal-CT in low-temperature siliceous sinter diagenesis, Taupo Volcanic Zone, New Zealand: Journal of Sedimentary Research, v. 74, p. 561-579.

LYNNE, B.Y., CAMPBELL, K.A., MOORE, J.N., and BROWNE, P.R.L., 2005, Diagenesis of 1900-year-old siliceous sinter (opal-A to quartz) at Opal Mound, Roosevelt Hot Springs, Utah, U.S.A.: Sedimentary Geology, v. 179, p. 249-278.

MICHALSKI, J.R., KRAFT, M.D., DIEDRICH, T., SHARP, T.G., and CHRISTENSEN, P.R., 2003, Thermal emission spectroscopy of the silica polymorphs and consideration for remote sensing of Mars: Geophysical Research Letters, v. 30, p. doi:10.1029/2003GL018354.

MOUNTAIN, B.W., BENNING, L.G., and BOEREMA, J.A., 2003, Experimental studies on New Zealand hot spring sinters: rates of growth and textural development: Canadian Journal of Earth Sciences, v. 40, p. 1643-1667.

MURATA, K.J., and NAKATA, J.K., 1974, Cristobalitic stage in the diagenesis of diatomaceous shale: Science, v. 184, p. 567-568.

MURPHY, R.P., and SEWARD, D., 1981, Stratigraphy, lithology, paleomagnetism, and fission track ages of some ignimbrite formations in the Matahana Basin, New Zealand: New Zealand Journal of Geology and Geophysics, v. 24, p. 325-331.

NEWMAN, S., STOLPER, E.M., and EPSTEIN, S., 1986, Measurement of water in rhyolitic glasses: Calibration of an infrared spectroscopic technique: American Mineralogist, v. 71, p. 1527-1541.

NICHOLSON, K., and PARKER, R., 1990, Geothermal sinter chemistry: towards a diagnositc signature and a sinter geothermometer: Proceedings of the 12th New Zealand Geothermal Workshop, p. 92-102.

NIELSEN, N., 1937, Renewed activity of the Great Geysir: The Geographical Journal, v. 89, p. 451-454.

PASVANOGLU, S., KRISTMANNSDÓTTIR, H., BJÖNSSON, S., and TORFASSON, H., 2000, Geochemical study of the Geysir geothermal field in Haukadalur, Iceland, Proceedings of the World Geothermal Congress 2000: Kyushu-Tohoku, Japan, p. 675-680.

PATERSON, M.S., 1982, The determination of hydroxyl by infrared absorption in quartz, silicate glasses and similar materials: Bull. Mineral., v. 105, p. 20-29.

RICE, S.B., FREUND, H., HUANG, W.L., CLOUSE, J.A., and ISAACS, C.M., 1995, Application of Fourier transform infrared spectroscopy to silica diagenesis: the opal-A to opal-CT transformation: Journal of Sedimentary Research, v. A65, p. 639-647.

RIMSTIDT, J.D., and COLE, D.R., 1983, Geothermal Mineralization I: The mechanism of formation of the Beowawe, Nevada, siliceous sinter deposit: American Journal of Science, v. 283, p. 861-875.

RODGERS, K.A., and CRESSEY, G., 2001, The occurrence, detection and significance of moganite (SiO_2) among some silica sinters: Mineralogical Magazine, v. 65, p. 157-167.

RODGERS, K.A., COOK, K.L., BROWNE, P.R.L., and CAMPBELL, K.A., 2002, The mineralogy, texture and significance of silica derived from alteration by steam condensate in three New Zealand geothermal fields: Clay Minerals, v. 37, p. 299-322.

RODGERS, K.A., and HAMPTON, W.A., 2003, Laser Raman identification of silica phases comprising microtextural components of sinters: Mineralogical Magazine, v. 67, p. 1-13.

RODGERS, K.A., BROWNE, P.R.L., BUDDLE, T.F., COOK, K.L., GREATEX, R.A., HAMPTON, W.A., HERDIANITA, N.R., HOLLAND, G.R., LYNNE, B.Y., MARTIN, R., NEWTON, Z., PASTARS, D., SANNAZZARO, K., and TEECE, C.I.A., 2004, Silica phases in sinters and residues from geothermal fields of New Zealand: Earth Science Reviews, v. 66, p. 1-61.

ROSSMAN, G.R., 1988, Vibrational spectroscopy of hydrous components, *in* Hawthorne, F.C., ed., Spectroscopic Methods in Mineralogy and Geology: Reviews in Mineralogy: Washington, Minerological Society of America, p. 193-206.

SCHOLZE, V.H., and FRANZ, H., 1960, Eine Methode zur Aufnahme von Ultrarot-Spektren von kornigem Material und ihre Anwendung auf einige Feldspate und SiO_2-Varietaten: Ber. DKG, v. 37, p. 420-423.

SEGNIT, E.R., STEVENS, T.J., and JONES, J.B., 1965, The role of water in opal: Journal of the Geological Society of Australia, v. 12, p. 211-226.

SEGNIT, E.R., ANDERSON, C.A., and JONES, J.B., 1970, A scanning microscope study of the morphology of opal: Search, v. 1, p. 349-351.

SILVER, L., and STOLPER, E., 1989, Water in albitic glasses: Journal of Petrology, v. 30, p. 667-709.

SMITH, B.C., 1996, Fundamentals of Fourier transform infrared spectroscopy: London, CRC Press, 202 p.

SMITH, B.Y., TURNER, S.J., and RODGERS, K.A., 2003, Opal-A and associated microbes from Wairakei, New Zealand: the first 300 days: Mineralogical Magazine, v. 67, p. 563-579.

SMITH, D.K., 1998, Opal, cristobalite, and tridymite: Noncrystallinity versus crystallinity, nomenclature of the silica minerals and bibliography: Powder Diffraction, v. 13, p. 2-19.

STOLPER, E., 1982, Water in silicate glasses: An infrared spectroscopic study: Contributions to Mineralogy and Petrology, v. 81, p. 1-17.

THORKELSSON, T., 1910, The hot springs of Iceland: The Royal Danish Science Society, v. Publication 7-VIII 4, p. 199-264.

TORFASSON, H., 1985, The Great Geysir: Reykjavik, Geysir Conservation Committee, 23 p.

WALTER, M.R., 1976, Geyserites of Yellowstone National Park: An example of abiogenic stromatolites, *in* Walter, M.R., ed., Stromatolites: Developments in Sedimentology: Amsterdam, Elsevier, p. 87-112.

WEED, W.H., 1889, Formation of travertine and siliceous sinter by the vegetation of hot springs, U.S. Geological Survey, p. 613-676.

WHITE, D.E., BRANNOCK, W.W., and MURATA, K.J., 1956, Silica in hot-spring waters: Geochimica et Cosmochimica Acta, v. 10, p. 27-59.

WILLIAMS, L.A., PARKS, G.A., and CRERAR, D.A., 1985, Silica diagenis, I. Solubility controls: Journal of Sedimentary Petrology, v. 55, p. 301-311.

WOOD, C.P., 1992, Geology of the Rotorua geothermal system: Geothermics, v. 21, p. 25-41.